NUMERICAL SIMULATIONS OF ULTRAFAST PULSE MEASUREMENTS

A Thesis
Presented to
The Academic Faculty

by

Xuan Liu

In Partial Fulfillment
of the Requirements for the Degree
Doctor of Philosophy in the
School of Physics

Georgia Institute of Technology
August 2007

NUMERICAL SIMULATIONS OF ULTRAFAST PULSE MEASUREMENTS

Approved by:

Dr. Rick Trebino, Advisor
School of Physics
Georgia Institute of Technology

Dr. John Buck
School of Electrical and Computer Engineering
Georgia Institute of Technology

Dr. Brian Kennedy
School of Physics
Georgia Institute of Technology

Dr. Chandra Raman
School of Physics
Georgia Institute of Technology

Dr. Michael Chapman
School of Physics
Georgia Institute of Technology

Date Approved: August 2007

Dedicated to the lost legend of the Gao family

from ShiGuanTun, SuiZhong Xian, Liao Ning Province, China

PREFACE

Just started? Then read the following(originally published in the nature magazine[19], 2006), discussing about "What makes a good PhD student?"

"• Choose a supervisor whose work you admire and who is well supported by grants and departmental infrastructure.

• Take responsibility for your project.

• Work hard - long days all week and part of most weekends. If research is your passion this should be easy, and if it isn't, you are probably in the wrong field. Note who goes home with a full briefcase to work on at the end of the day. This is a cause of success, not a consequence.

• Take some weekends off, and decent holidays, so you don't burn out.

• Read the literature in your immediate area, both current and past, and around it. You can't possibly make an original contribution to the literature unless you know what is already there.

• Plan your days and weeks carefully to dovetail experiments so that you have a minimum amount of downtime.

• Keep a good lab book and write it up every day.

• Be creative. Think about what you are doing and why, and look for better ways to go. Don't see your PhD as just a road map laid out by your supervisor.

• Develop good writing skills: they will make your scientific career immeasurably easier.

• To be successful you must be at least four of the following: smart, motivated, creative, hard-working, skilful and lucky. You can't depend on luck, so you had better focus on the others!"

ACKNOWLEDGEMENTS

I would like to thank Dr. Rick Trebino for his enthusiasm and encouragement, which made this thesis possible. His knowledge and innovation always shines lights on our research. His perfection in presentation and paper writing is a legend. Special thanks to Dr. Arlee V. Smith, a 'Jedi' master in nonlinear optics, for his enormous help. Many thanks to Linda Trebino who carried away those paperwork burden for us. Also I would like to thank Aparna, Dongjoo, Erik, Helen, Kristen, Lina, Mark, Neeraj, Pablo, Pam, Qiang, Saman, Selçuk, Stephan, Wenyu, Xun and Ziyang(listed in alphabetic order) for being such nice people to work with. And finally, my father Zhengchun and my mother Jingzhi, thank you for your love.

TABLE OF CONTENTS

LIST OF FIGURES

SUMMARY

This thesis contains two major components of research: numerical simulation of optical-parametric amplification cross correlation of Frequency-Resolved Optical Gating (OPA-XFROG) and numerical simulation of GRENOUILLE and its related issues.

Recently, an extremely sensitive technique–OPA-XFROG has been developed. A short pump pulse serves as the gate by parametrically amplifying a short segment of the signal pulse in a nonlinear crystal. High optical parametric gain makes possible the complete measurement of ultraweak, ultrashort light pulses. Unlike interferometric methods, it does not carry prohibitively restrictive requirements, such as perfect mode-matching, perfect spatial coherence, highly stable absolute phase, and a same-spectrum reference pulse. We simulate the OPA-XFROG technique and show that by a proper choice of the nonlinear crystal and the noncollinear mixing geometry it is possible to match the group velocities of the pump, signal, and idler pulses, which permits the use of relatively thick crystals to achieve high gain without measurement distortion. Gain bandwidths of 100 nm are possible, limited by group velocity dispersion.

In the second part of the thesis, we numerically simulate the performance of the ultrasimple ultrashort laser pulse measurement device- GRENOUILLE. While simple in practice, GRENOUILLE has many theoretical subtleties because it involves the second-harmonic generation of relatively tightly focused and broadband pulses. In addition, these processes occur in a thick crystal, in which the phase-matching bandwidth is deliberately made narrow compared to the pulse bandwidth. We developed a model that include all sum-frequency-generation processes, both collinear and

noncollinear. We also include dispersion using the Sellmeier equation for the crystal BBO. Working in the frequency domain, we compute the GRENOUILLE trace for practical-and impractical-examples and show that accurate measurements are easily obtained for properly designed devices.

For pulses far outside a GRENOUILLE's operating range (on the long side), we numerically deconvolve the GRENOUILLE trace with the response function of GRENOUILLE to improve its spectral resolution.

In the last part of the thesis, we simulate the second harmonic generation with tightly focused beams by use of lens. Thus, we are able to explain the 'weird' focusing effect that has been a 'puzzles' for us in the GRENOUILLE measurement[76].

CHAPTER I

THE MEASUREMENT OF ULTRASHORT PULSES: FROG(FREQUENCY-RESOLVED OPTICAL GATING)

An ultrafast pulse is a very short burst of electro-magnetic energy. Its mathematic expression is the product of a pulse envelope and a sin wave, with a carrier frequency on the order of 10^{15} second^{-1}. It is the shortest event ever created by human beings. Its vast applications to various fields, such as physics, chemistry, biology and engineering make it very important to fully characterize it.

"In order to measure an event in time, you must use a shorter one. So how do you measure the shortest event ever created?"

The answer to that question was found to be–use the pulse itself. Due to its incredible short duration, an ultrashort pulse have a very broad bandwidth. For the measurement of an ultrashort pulse, we concern not only its intensity, but also its color variation in time, which is a problem of measuring the phase of the pulse.

Early attempt, such as the intensity autocorrelation[63, 86, 102] can give a very crude estimation of the pulse temporal width, but no pulse shape or phase information. Spectral phase interferometry for direct electric-field reconstruction(SPIDER)[51, 52] is based on shearing interferometry in the optical frequency domain. It uses nonlinear frequency mixing to generate a pair of identical but frequency-sheared replicas of the input pulse. The phase information of the pulse is obtained by use of a direct inversion algorithm of the resulted interferogram and a separate measurement is done to measure the spectrum. However, the SPIDER experiment apparatus is very complicated, which involves twelve sensitive alignment parameters. Mechanical instability

and poor beam quality can wash out the fringes easily. No independent measurements are available to check its correctness. Ambiguities arises since pulse delay has to be chosen for the particular pulse. Even worse, recently it was pointed out that most measurements made by SPIDER have errors more than a pulse length![10, 11]

Fortunately, the Frequency-Resolved Optical Gating(FROG) technique and the class of its kind introduced in the early 1990s and later on solved those problems mentioned above[24, 25, 26, 27, 56, 57, 58, 59, 93]. It is a very powerful technique that can completely characterize an ultrashort pulse in the time/frequency domain. It measures the spectrogram of a pulse and uses an iterative algorithm to retrieve the pulse intensity and phase. It can measure not only well behaved laser pulses, but also pulses not so well-behaved in space, time and frequency or even extremely weak pulses. Gu et. al performed the measurement of the ultrabroadband continuum(up to 1200 nm wide) generated from microstructure optical fiber using cross-correlation frequency-resolved gating(XFROG) with an angle dithered nonlinear-optical crystal[48]. Transient-Grating Frequency-Resolved-Optical-Gating(TG FROG) uses a third-order nonlinear-optical beam geometry, suitable for measurement of broadband UV pulses or microjou- or higher-energy pulses[66]. Ultraweak light pulses with only a few attojoules per pulse can also be measured using optical-parametric-amplification cross-correlation frequency-resolved optical gating (OPA-XFROG)[107]. A simplest ultrashort pulse measurement device, Grating Eliminated No-Nonsense Observation of Ultrafast Incident Laser Light E-fields (GRENOUILLE) was developed, which is extremely compact and alignment free[4, 6, 7, 8, 77]. Without any modification, GRENOUILLE also measures spatio-temporal distortions and pulse front tilt[2, 3, 5].

In this chapter, we will give a brief introduction to FROG and XFROG theory, and explain how GRENOUILLE works.

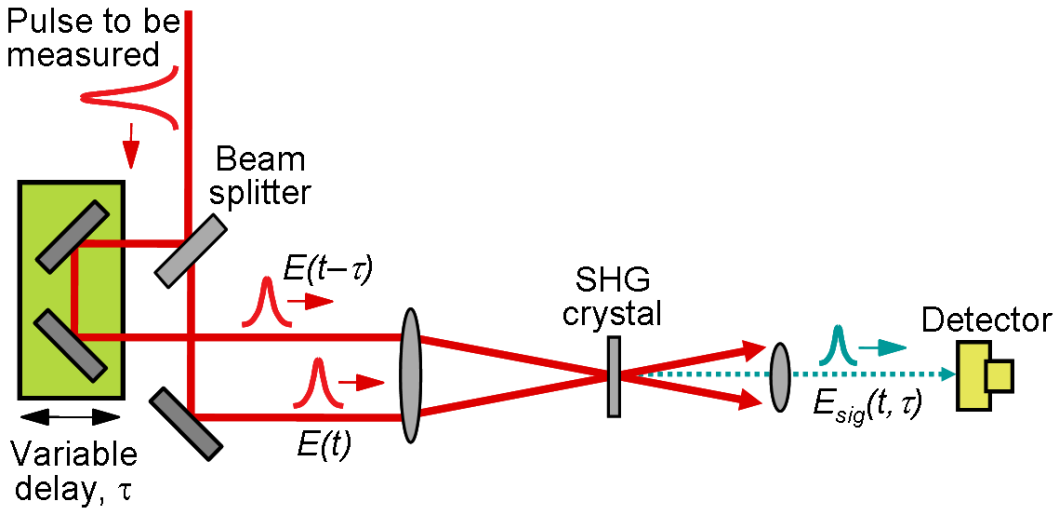

Figure 1: Schematic diagram of an SHG autocorrelator.

1.1 Autocorrelation

The forerunner of the ultrafast pulse measurement techniques is intensity autocorrelation [63, 86, 102], which inspires the invention of the FROG technique. Virtually all available techniques are based on autocorrelation.

Figure 1 shows the diagram of an autocorrelator. The pulse to be measured is splitted into two after a beam splitter. One of the beam is delayed by use of a delay stage, then the two pulses are overlapped both in time and space inside a nonlinear second-harmonic-generation(SHG) crystal. While moving the delay stage, the two pulses are swept with respect to each other. The generated second harmonic field is given by:

$$E_{sig}^{SHG}(t,\tau) \propto E(t)E(t-\tau) \tag{1}$$

The autocorrelation signal intensity $A(\tau)$ is recorded by a slow detector and mapped out as a function of delay.

$$A(\tau) = \int_{-\infty}^{\infty} I(t)I(t-\tau)\,dt \tag{2}$$

Autocorrelation attempts to measure the pulse's temporal intensity, but not the phase of the pulse. The autocorrelation width $\Delta\tau_A^{FWHM}$ of a pulse is somewhat related to

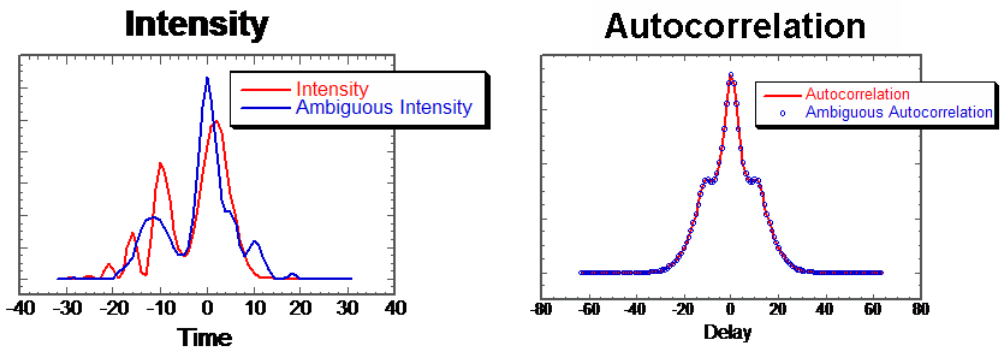

Figure 2: Different pulse intensities can correspond to one autocorrelation intensity.

its own intensity width $\Delta\tau_P^{FWHM}$. For a square shaped input pulse, $\Delta\tau_A^{FWHM}$ is equal to $\Delta\tau_P^{FWHM}$. If the input pulse is Gaussian shaped, $\Delta\tau_P^{FWHM}$ is equal to $\Delta\tau_A^{FWHM}$ divided by a constant 1.41. For an input pulse that has $Sech^2$ shape, $\Delta\tau_P^{FWHM}$ is equal to $\Delta\tau_A^{FWHM}$ divided by 1.54. In order to obtain a pulse's length, intensity autocorrelation requires a *priori* knowledge about the shape of the unknown input, which is not practical. Even worse, several pulse intensities that have complicated structures can correspond to exactly one autocorrelation intensity[20, 93](See Figure 2). Thus, autocorrelation can not provide us reliable information about the pulse intensity or width. Various methods have been proposed for better performance over the years. Intensity correlation combined with spectrum [78] uses an iterative algorithms to find the pulse intensity and phase that are consistent with the autocorrelation intensity and spectrum. However, the algorithm only yields *a* possible but not *the* pulse field for the same difficulties. Third order intensity autocorrelation[37] beaks the symmetry of autocorrelation, but it still could not uniquely determine the pulse intensity, so does the interferometric autocorrelation[31].

Even today, many people out of there are still using intensity autocorrelation method to characterize their pulses, which is quite irresponsible for serious scientific research. Advanced technique, such as FROG should be used and we will discuss this

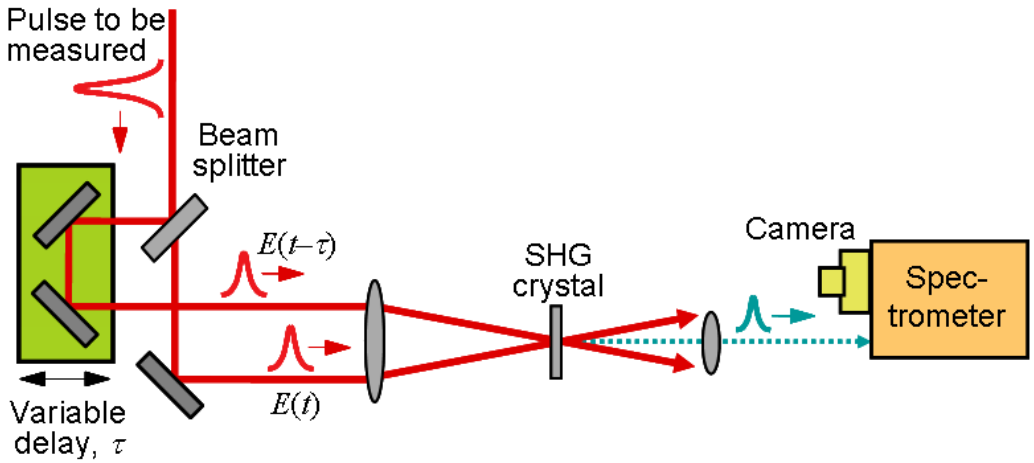

Figure 3: The SHG FROG apparatus.

topic next.

1.2 FROG

Frequency-Resolved Optical Gating(FROG) [57, 59, 92] works in a hybrid time-frequency domain. It can completely determine the pulse intensity and phase(except for a few trivial ambiguities.)

FROG closely resembles autocorrelation-type measurement, except the autocorrelation signal is spectrally resolved. For a FROG apparatus, the only difference is that a spectrometer replaces the detector in a autocorrelator(The experiment set up for a SHG FROG is shown in Figure 3.). FROG measures the spectrogram of a pulse, in other words– a set of spectra of all gated slices of the unknown field $E(t)$ at different delays τ. In general, the mathematic form of a FROG trace can be written as:

$$I_{\mathrm{FROG}}(\omega,\tau) = \left| \int_{-\infty}^{\infty} E_{sig}(t,\tau)\exp(-i\omega t)\mathrm{d}t \right|^2 \tag{3}$$

If a second harmonic nonlinearity is used, $E_{sig}(t,\tau) = E(t)E(t-\tau)$. For third-order polarization-gate process, $E_{sig}(t,\tau) = E(t)|E(t-\tau)|^2$ and for third-harmonic generation(THG) process, $E_{sig}(t,\tau) = E(t)^2E(t-\tau)$. We neglected the proportionality constants here. Figure 4 shows the SHG FROG trace of a double chirped pulse. As you can see, what we have here is a two-dimensional trace with N by N data points.

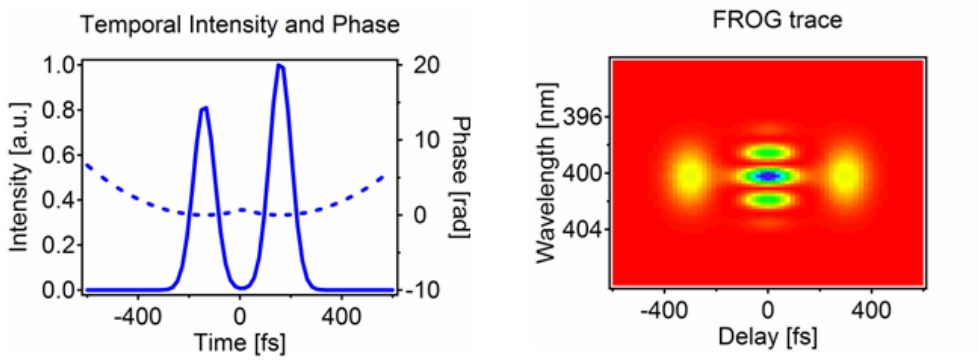

Figure 4: The SHG FROG trace(right) for a double chirped pulse(left).

It is helpful if we rewritten the FROG trace as a two-dimensional Fourier transform of $\bar{E}_{sig}(t,\Omega)$:

$$I_{\mathrm{FROG}}(\omega,\tau) = \left| \int_{-\infty}^{\infty} \int_{-\infty}^{\infty} \bar{E}_{sig}(t,\Omega) \exp(-i\omega t - i\Omega\tau) \mathrm{d}t \mathrm{d}\Omega \right|^2 \tag{4}$$

where $\bar{E}_{sig}(t,\Omega)$ and $E_{sig}(t,\tau)$ are the one-dimensional Fourier transform pairs:

$$E_{sig}(t,\tau) = \int_{-\infty}^{\infty} \bar{E}_{sig}(t,\Omega) \exp(-i\Omega\tau) \mathrm{d}\Omega. \tag{5}$$

A close examination of equation (4) tells us that finding $E(t)$ is actually a two dimentional phase-retrieval problem[90]. It is *solved* and has an essentially *unique* solution provided with additional information such as that $\bar{E}_{sig}(t,\Omega)$ has finite support[38, 39, 40, 41, 79, 90, 95](zero outside a finite range of values of t and Ω).

For FROG, this condition is not met. $\bar{E}_{sig}(t,\Omega)$ can not be finite in extent simultaneously in both time and frequency. However, we have a much more better constraint, the so called nonlinear-optical constraints which result from the generation of the nonlinear signal field. For example, in SHG FROG, $E_{sig}(t,\tau) = E(t)E(t-\tau)$. It is a very strong constraint and the FROG trace can essentially uniquely determine the pulse field[93]. Once we retrieved $\bar{E}_{sig}(t,\Omega)$ from the FROG trace, we can just inverse Fourier transform it with respect to Ω to get $E(t)E(t-\tau)$. If we substitute τ by t, we have $E(t)E(t-\tau)|_{t=\tau} = E(t)E(0)$ and $E(0)$ is just a constant.

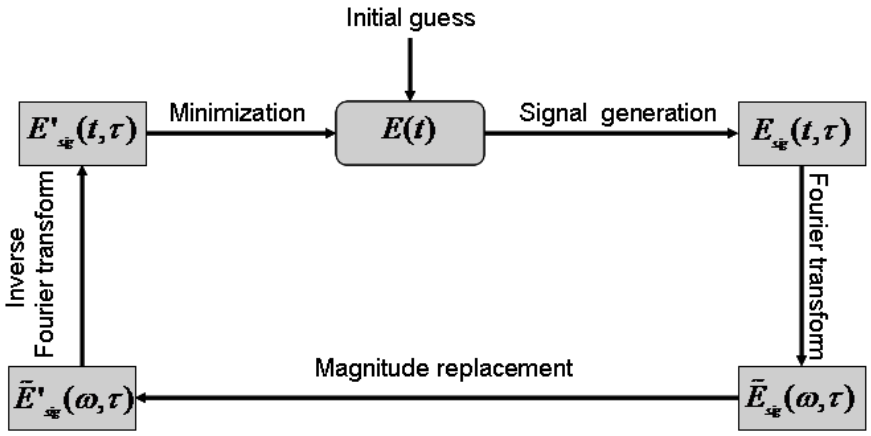

Figure 5: A generic FROG algorithm.

The retrieval of $\bar{E}_{sig}(t,\Omega)$ from a FROG trace is quite indirect and complicated. An iterative algorithm is used to find the solution and it works very well. A generic FROG algorithm is shown schematically in Figure 5. Initially, the algorithm makes a random guess of the electric field $E(t)$, which is then used to generate the signal field $E_{sig}(t,\tau)$. For SHG FROG, $E_{sig}(t,\tau) = E(t)E(t-\tau)$. The signal field in the frequency domain $\tilde{E}_{sig}(\omega,\tau)$ is simply derived by a Fourier transformation of $E_{sig}(t,\tau)$ with respect to t. Since the squared magnitude of $\tilde{E}_{sig}(\omega,\tau)$ should be equal to the measured trace, we replace the magnitude of $\tilde{E}_{sig}(\omega,\tau)$ with the square root of $I_{FROG}(\omega,\tau)$ to generate $\tilde{E}'_{sig}(\omega,\tau)$. $E'_{sig}(\omega,\tau)$ is then inverse Fourier transformed back to the time domain to get $E'_{sig}(t,\tau)$. The modified signal field $E'_{sig}(t,\tau)$ is used to generate a better guess of $E(t)$ for the next iteration. This specific step is also called the minimization step. The above process is repeated until certain termination criterion is met. This criterion is a measure of the error between the actual electric field and the retrieved field. We call it the FROG error, or the G error. In the k-th iteration it is defined as

$$G^{(k)} = \sqrt{\frac{1}{N^2}\sum_{i,j=1}^{N}\left|I_{FROG}(\omega_i,\tau_j) - \mu I^{(k)}_{FROG}(\omega_i,\tau_j)\right|^2}, \tag{6}$$

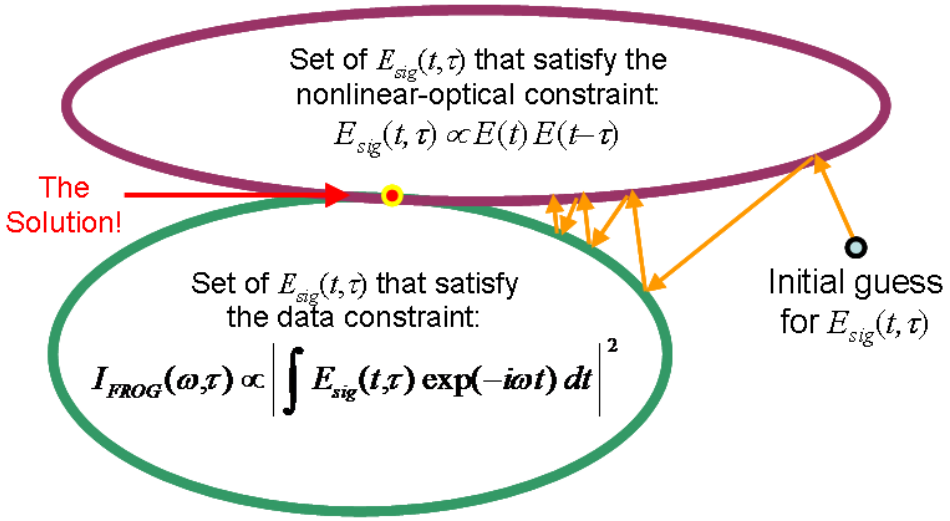

Figure 6: Generalized projection.

where μ is a real normalization constant that minimizes the error $G^{(k)}$. $I^{(k)}_{FROG}(\omega_i, \tau_j)$ is the k-th iteration of the retrieved FROG trace and $I_{FROG}(\omega_i, \tau_j)$ is the measured FROG trace. For SHG FROG,

$$G^{(k)}_{SHG-FROG} = \sqrt{\frac{1}{N^2}\sum_{i,j=1}^{N}\left| I_{FROG}(\omega_i,\tau_j) - \mu \left| \int_{-\infty}^{+\infty} E^{(k)}(t)E^{(k)}(t-\tau)\exp(-i\omega t)dt \right|^2 \right|^2} \tag{7}$$

It has been proven that the FROG error is an effective measure for convergence and it is used for all the FROG retrieval algorithms. In practise, an empirical small value G_0 is set and the algorithm is terminated when $G^{(k)} < G_0$.

Among all the available retrieval algorithms, generalized projection method appears to be very reliable and superior to the others[23, 28, 29, 53, 90, 103, 104](See figure 6). The entire figure represents the set of all signal fields $E_{sig}(t,\tau)$. We want to find the signal-field that satisfy both data and nonlinear optical constrains. If we use the upper elliptical to indicate the nonlinear optical constraint and the lower elliptical to represent the data constraint(See equation 3), the solution will correspond to the intersection of the two elliptical regions.

In operation, we start with an arbitrary point in the plane. The pulse is then mapped to the closest point in the constraint sets. Projections are repeated until reaching the solution. For convex sets, convergence is guaranteed, but generally occurs even with non-convex sets and particularly FROG. In order to satisfy the data constraint, it is necessary to perform the magnitude replacement with the measured FROG trace at each iteration. For the nonlinear optical constraint, it takes some effort. We need to find a new signal field $E_{sig}^{(k+1)}(t_i, \tau_j)$ that has the right nonlinear optical form and at the same time it is closest to the current signal field $E_{sig}^{\prime(k)}(t_i, \tau_j)$. So we need to minimize the following functional distance or Z error,

$$Z = \sum_{i,j=1}^{N} \left| E_{sig}^{\prime(k)}(t_i, \tau_j) - E_{sig}^{(k+1)}(t_i, \tau_j) \right|^2. \tag{8}$$

For SHG FROG, it is:

$$Z^{SHG} = \sum_{i,j=1}^{N} \left| E_{sig}^{\prime(k)}(t_i, \tau_j) - E^{(k+1)}(t_i) E^{(k+1)}(t_i - \tau_j) \right|^2. \tag{9}$$

In FROG algorithm, minimization of the Z error is treated as an unconstrained multi-dimensional optimization problem with computation of derivatives. Steepest decent method is used to find the minimization direction for each step. The gradient of Z is calculated with respect to $E^{(k+1)}(t_k)$ $(t_k = 1, 2, 3, ...N)$. In practice we calculate the 2N real quantities, shown as following(using SHG FROG as an example),

$$\begin{aligned}
&\frac{\partial Z^{SHG}}{\partial \mathrm{Re}\{E^{(k+1)}(t_k)\}} = 2\mathrm{Re}\{\sum_{j=1}^{N} -E_{sig}^{\prime(k)}(t_k, \tau_j)^* E^{(k+1)}(t_k - \tau_j) + E^{(k+1)}(t_k)^* \left| E^{(k+1)}(t_k - \tau_j) \right|^2 \\
&- E_{sig}^{\prime(k)}(t_k + \tau_j, \tau_j)^* E^{(k+1)}(t_k + \tau_j) + E^{(k+1)}(t_k)^* \left| E^{(k+1)}(t_k + \tau_j) \right|^2 \} \\
&\frac{\partial Z^{SHG}}{\partial \mathrm{Im}\{E^{(k+1)}(t_k)\}} = -2\mathrm{Im}\{\sum_{j=1}^{N} -E_{sig}^{\prime(k)}(t_k, \tau_j)^* E^{(k+1)}(t_k - \tau_j) + E^{(k+1)}(t_k)^* \left| E^{(k+1)}(t_k - \tau_j) \right|^2 \\
&- E_{sig}^{\prime(k)}(t_k + \tau_j, \tau_j)^* E^{(k+1)}(t_k + \tau_j) + E^{(k+1)}(t_k)^* \left| E^{(k+1)}(t_k + \tau_j) \right|^2 \}
\end{aligned} \tag{10}$$

So the new signal field can be calculated as,

$$E^{(k+1)}(t_k) = E_{in}^{(k)}(t_k) + x \cdot dE^{(k)}(t_k) \tag{11}$$

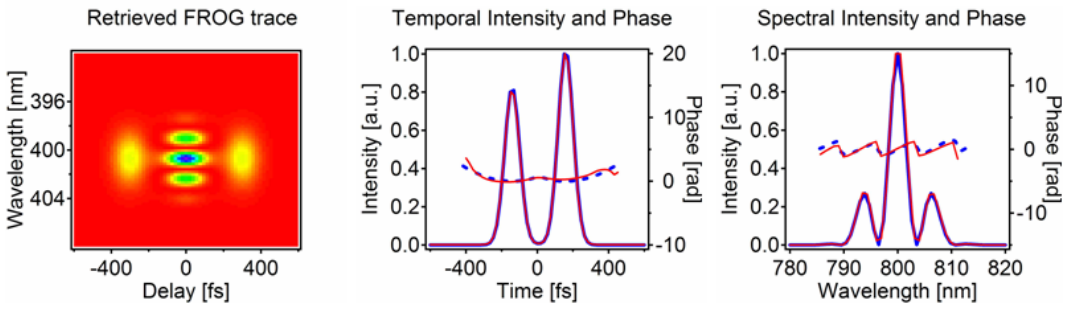

Figure 7: FROG retrieval. The Blue curves correspond to the real input pulse intensity and phase and the red lines correspond to the retrieved intensity and phase.

$$dE^{(k)} = \frac{2\partial Z}{\partial E^{(k+1)}(t_k)^*}\bigg|_{E^{(k+1)}(t_k)=E_{in}^{(k)}(t_k)}. \tag{12}$$

We still need to find the one dimensional minimization step length x towards the direction dE. We substitute equation (11) back into equation (9),

$$Z = \sum_{i,j=1}^{N} \left| E_{sig}^{\prime(k)}(t_i,\tau_j) - [E_{in}^{(k)}(t_i) + x\cdot dE^{(k)}(t_i)][E_{in}^{(k)}(t_i-\tau_j) + x\cdot dE^{(k)}(t_i-\tau_j)] \right|^2 \tag{13}$$

Equation (13) can be expended into a polynomial of order four with variable x,

$$Z = a_0 + a_1 x + a_2 x^2 + a_3 x^3 + a_4 x^4 \tag{14}$$

where,

$$\begin{aligned}
a_0 &= \sum_{i,j=1}^{N} \left| E_{sig}^{\prime(k)}(t_i,\tau_j) - E_{in}^{(k)}(t_i)E_{in}^{(k)}(t_i-\tau_j) \right|^2 \\
a_1 &= \sum_{i,j=1}^{N} 2\mathrm{Re}\{[E_{in}^{(k)}(t_i)E_{in}^{(k)}(t_i-\tau_j) - E_{sig}^{\prime(k)}(t_i,\tau_j)]^* \\
&\times [E_{in}^{(k)}(t_i)dE^{(k)}(t_i-\tau_j) + E_{in}^{(k)}(t_i-\tau_j)dE^{(k)}(t_i)]\} \\
a_2 &= \sum_{i,j=1}^{N} \left| E_{in}^{(k)}(t_i-\tau_j)dE^{(k)}(t_i) + E_{in}^{(k)}(t_i)dE^{(k)}(t_i-\tau_j) \right|^2 + \\
&2\mathrm{Re}\{[E_{in}^{(k)}(t_i)E_{in}^{(k)}(t_i-\tau_j) - E_{sig}^{\prime(k)}(t_i,\tau_j)]^* dE^{(k)}(t_i)dE^{(k)}(t_i-\tau_j)\} \\
a_3 &= \sum_{i,j=1}^{N} 2\mathrm{Re}[E_{in}^{(k)}(t_i-\tau_j)dE^{(k)}(t_i) + E_{in}^{(k)}(t_i)dE^{(k)}(t_i-\tau_j)]^* dE^{(k)}(t_i)dE^{(k)}(t_i-\tau_j) \\
a_4 &= \sum_{i,j=1}^{N} \left| dE^{(k)}(t_i)dE^{(k)}(t_i-\tau_j) \right|^2
\end{aligned} \tag{15}$$

It is a one dimensional minimization problem and the global minimum can be easily calculated.

Applying our generalize projection algorithm to the simulated example FROG trace shown in figure 4, we can retrieve the input pulse very well(See figure 7). The FROG error was 0.000377.

For the retrieval of experimental traces, one important question has to be asked, " How robust the FROG technique is against noise?". Since in all measurements, noise is unavoidable. It puts the FROG-retrieval algorithm into test. Fortunately , it has been found that the FROG algorithm converges very well [43]. Adding a massive 10% multiplicative noise in the trace only brings in 1% rms error in the retrieved intensity and phase. Adding additive noise, it is a tricker problem. However, simple filtering techniques can be used to remove such noises. It has been shown that 10% additive noise also results in 1% rms error to the retrieved pulse intensity and phase after filtering. In addition, boot-strap method can be used to determine the error bars for the retrieved intensity and phase of a FROG measurement[96, 97]. So we know how accurate we are doing at each retrieved intensity and phase points!

So far, we have shown that the FROG technique can fully characterize a pulse intensity and phase in an elegant manner- simple but powerful. We still need to keep in mind that we can not use the FROG technique to determine the absolute phase of a pulse, or the pulse arrival time. For most of the applications, those information turns out to be uninteresting. For SHG type of FROG measurement, it has an ambiguity in the direction of time, but this time-reverse problem can be easily removed. One way is to place a thin glass before the beam splitter[91]. The surface reflection will introduce a small trailing satellite pulse and thus beak the symmetry to remove the ambiguity.

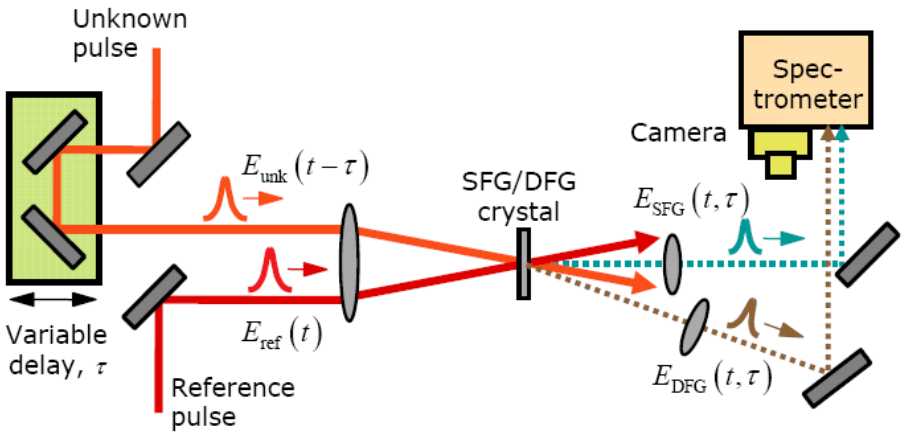

Figure 8: Experiment set up of SFG/DFG XFROG.

1.3 XFROG

FROG technique does not require a shorter reference pulse. However, if a reference pulse is readily available and we can make use of it to help our FROG measurement.

Temporal Analysis by Dispersing a pair of Light E-fields(TADPOLE) is a technique that combines FROG and spectral interferometry(SI) methods[46, 80]. The reference pulse is characterized by a FROG and it tells us the spectral phase of the reference pulse $\psi_{ref}(\omega)$. SI measures the pulse spectrum and the spectral phase difference between the unknown and the reference pulse: $\Delta\phi(\omega) = \psi_{ref}(\omega) - \psi(\omega)$. Trains of pulses as weak as 42×10^{-21} joules per pulse have been measured by use of TADPOLE[42]. It is also an excellent method to measure shaped ultrashort pulses[98]. The drawback of SI type of measurements are: The reference pulse spectral range needs to contain that of the unknown pulse; Perfect beam collinearity and excellent spacial coherence are required.

Obviously, for measurement of spuercontinuum from microstructure-fiber or luminescence from molecules, TADPOLE is hopeless. Another technique, called cross-correlation Frequency-Resolved Optical Gating (XFROG) has been introduced for

such type of measurements when a reference pulse is available[67, 68]. Figure 8 shows the experiment apparatus of an XFROG. The cross-correlation signal is generated through sum frequency generation(SFG), difference frequency generation(DFG) or other third-order nonlinear processes, depending on the relative frequencies. For sum frequency generation, the signal field of XFROG has the form,

$$E_{sig}^{SFG} = E(t)E_{ref}(t-\tau). \tag{16}$$

For difference frequency generation, it is

$$E_{sig}^{DFG} = E(t)E_{ref}^{*}(t-\tau). \tag{17}$$

The SFG XFROG trace can then be written as(in the following discussion, we use SFG XFROG as our example),

$$I_{\mathrm{XFROG}}^{SFG}(\omega,\tau) = \left|\int_{-\infty}^{\infty} E(t)E_{ref}(t-\tau)\exp(-i\omega t)\mathrm{d}t\right|^2. \tag{18}$$

Concerning the XFROG retrieval algorithm, only minor changes need to be made to the usual FROG algorithm. First, we define the Z error for XFROG:

$$Z_{XFROG}^{SFG} = \sum_{i,j=1}^{N}\left|E_{sig}^{\prime(k)}(t_i,\tau_j) - E^{(k+1)}(t_i)E_{ref}(t_i-\tau_j)\right|^2. \tag{19}$$

It appears simpler since the reference field $E_{ref}(t_i,\tau_j)$ is known. The gradient of Z with respect to $E^{(k+1)}(t_k)^*$ is,

$$\frac{dZ_{XFROG}^{SFG}}{dE^{(k+1)}(t_k)^*} = \sum_{\tau} E_{ref}(t_k-\tau)^*[E_{sig}^{\prime(k)}(t_k,\tau) - E^{(k+1)}(t_k)E_{ref}(t_k-\tau)] \tag{20}$$

Let the above derivative equal to zero and we can solve $E^{(k+1)}(t_k)$ for the next iteration directly,

$$E^{(k+1)}(t_k) = \frac{\sum\limits_{\tau} E_{ref}(t_k-\tau)^* E_{sig}^{(k)}(t_k-\tau)}{\sum\limits_{\tau}\left|E_{ref}(t_k-\tau)\right|^2}. \tag{21}$$

And this is the only change made to the FROG retrieval program. The XFROG algorithm has been tested for different unknown pulses and reference pulses. It can

retrieve the unknown pulse very well with a typical G error on the order of 10^{-7} for a 64 by 64 trace.

For XFROG type of measurement, if the reference pulse is intense, higher efficiency is expected because signal strength I_{sig}^{XFROG} is proportional to $I_{unk}I_{ref}$. XFROG does not require spectral overlap between the unknown pulse and the reference pulse. It also does not require stringent coherence or mode matching etc. It can be applied to the measurement of ultra weak light pulses. We will discuss various detailed prospects of Optical-Parametric Amplification (OPA) XFROG[69] in chapter 3. For measurement of weak blue or UV pulses, if we use a visible or infrared reference pulse as the gate pulse, DFG process will generate a convenient wavelength that is possible for us to measure, since SHG crystal becomes absorptive at those pulses' second harmonic frequencies. For the measurement of a very complex pulse, XFROG is also a better choice since we can choose a very smooth reference pulse to generate a much less complicated trace.

1.4 GRENOUILLE

Recently, an extremely simple pulse-measurement device was introduced and is now in wide use. A highly simplified version of the frequency-resolved-optical-gating (FROG) family of devices, this method (called GRENOUILLE[77]; see Figure 9) operates by using a simple, large-apex-angle prism (a "Fresnel biprism") to split the beam into two replicas and to automatically cross and align them in space and time in the crystal. It uses a relatively large crossing angle and a line focus, so the pulse replicas' relative delay is mapped onto the crystal transverse position. GRENOUILLE's second innovation is the use of a thick second-harmonic-generation (SHG) crystal, which, due to its thickness, phase-matches only a small-and different-fraction of the pulse bandwidth for each output angle, allowing the crystal to operate, not only as

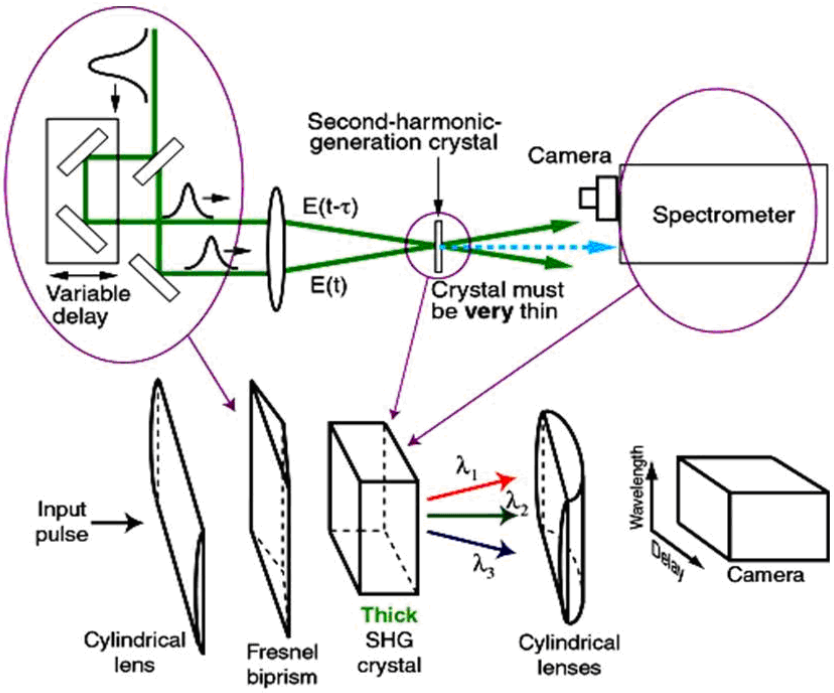

Figure 9: FROG (top) and its simpler cousin, GRENOUILLE (bottom).

an autocorrelating element, but also as a spectrometer. The phase-matching bandwidth of the thick crystal is then GRENOUILLE's spectral resolution (and not its spectral range, as in other devices). These two simple innovations yield a very simple, compact FROG device composed of only four easily aligned, linearly arranged optical elements and that requires almost no alignment and never misaligns. In addition, without modification, GRENOUILLE also measures the spatio-temporal distortions, spatial chirp and pulse-front tilt: the otherwise symmetrical trace develops shear in the presence of spatial chirp and displacement along the delay axis in the presence of pulse-front tilt [2, 3, 5]. In chapter 4, we describe a numerical model that simulates the GRENOUILLE device. We compute the GRENOUILLE trace for pratical examples and show that accurate measurements are easily obtained for properly designed devices.

CHAPTER II

PULSE PROPAGATION

The theoretical study carried out in chapter 3 and 4 involves the pulse propagation in medium. In this chapter, we will cover some of the basics in this area. Books authored by Boyd, Shen, Diels [16, 32, 87] are suggested for further readings.

The wave equation for electric field vector $\mathbf{E}$ can be derived from Maxwell equations, which has the form:

$$(\frac{\partial}{\partial x^2} + \frac{\partial}{\partial y^2} + \frac{\partial}{\partial z^2} - \frac{1}{c^2}\frac{\partial}{\partial t^2})\mathbf{E}(x, y, z, t) = \mu_0 \frac{\partial}{\partial t^2}\mathbf{P}(x, y, z, t) \tag{22}$$

where μ_0 is the magnetic permeability in free space. The source term, polarization $\mathbf{P}$ describes the interaction between the pulse field and the medium,

$$\mathbf{P} = \varepsilon_0 \chi(E)E = \varepsilon_0 \chi^{(1)}E + \varepsilon_0 \chi^{(2)}E^2 + \varepsilon_0 \chi^{(3)}E^3 + ... + \varepsilon_0 \chi^{(n)}E^n + ... \tag{23}$$

$\chi^{(n)}$ is known as the nonlinear optical susceptibility of the n^{th} order. $\chi^{(1)}$ is the linear susceptibility. We can rewritten the induced polarization in two parts:

$$\mathbf{P} = \mathbf{P}^L + \mathbf{P}^{NL} \tag{24}$$

$\mathbf{P}^L$ represents the linear response of the medium, such as diffraction, dispersion, refraction, linear loss/gain etc. $\mathbf{P}^{NL}$ takes account for the nonlinear optical effects, *eg.*, nonlinear absorption and gain, harmonic generations, and Raman processes etc. In the following sections we will discuss those effects separately for simplicity. A numerical technique, split-step method will be introduced for solving the nonlinear partial differential equations.

2.1 Linear propagation

In this section, we consider only the contribution of the linear polarization $\mathbf{P}^L$ but omit $\mathbf{P}^{NL}$. Assuming the pulse envelope does not change significantly when traveling through a distance comparable with the wavelength, also known as the slowly-varying-envelope approximation(SVEA):

$$\left|\frac{\partial^2 E(x,y,z,t)}{\partial z^2}\right| \ll \left|k\frac{\partial E(x,y,z,t)}{\partial z}\right| \tag{25}$$

so the ∂_z^2 terms can be neglected. The propagation function for an e-polarized beam in a uniaxial crystal is(The details can be found in Ref.[33, 34, 36, 44]):

$$\begin{aligned}
&\tfrac{\partial E(x,y,z,t)}{\partial z} = -\tan\rho\tfrac{\partial E(x,y,z,t)}{\partial x} \\
&+i\tfrac{1}{2k}[n^2(\tfrac{\cos^2\theta}{n_e^2}+\tfrac{\sin^2\theta}{n_o^2})-\tan^2\rho]\tfrac{\partial^2 E(x,y,z,t)}{\partial^2 x} \\
&+i\tfrac{1}{2k}\tfrac{n^2}{n_e^2}\tfrac{\partial^2 E(x,y,z,t)}{\partial^2 y} - \tfrac{1}{v_g}\tfrac{\partial E(x,y,z,t)}{\partial t} \\
&-i\tfrac{gvd}{2}\tfrac{\partial^2 E(x,y,z,t)}{\partial^2 t} - i(\tfrac{\partial\tan\rho}{\partial\omega}\big|_c)\tfrac{\partial^2 E(x,y,z,t)}{\partial x\partial t}
\end{aligned} \tag{26}$$

The last term is taken with respect to the carrier frequency. n is the refractive index. Extraordinary wave experiences a refractive index $n(\theta)$ that depends on the angle θ between the k vector and the optic axis according to:

$$\frac{1}{n(\theta)^2} = \frac{\sin^2\theta}{n_e^2} + \frac{\cos^2\theta}{n_o^2} \tag{27}$$

where n_e and n_o correspond to the principle extraordinary and ordinary refractive index respectively. $k = n\omega/c$ is the wave vector. $tan\rho = -(1/k)\partial k/\partial\theta$ is the birefringent walkoff. v_g is the velocity of the pulse envelope , or the group velocity, by definition,

$$v_g = (\frac{\partial k}{\partial\omega})^{-1} = (\frac{n}{c}+\frac{\omega}{c}\frac{\partial n}{\partial\omega})^{-1} \tag{28}$$

gvd is the group velocity dispersion,

$$gvd = \frac{\partial^2 k}{\partial\omega^2} = \frac{\partial(\partial k/\partial\omega)}{\partial\omega} = -\frac{1}{v_g^2}\frac{\partial v_g}{\partial\omega} \tag{29}$$

gvd describes that for different wavelength in the pulse, the group velocity will be different. It disperses a pulse in time and leads to a frequency chirp and a reshaping of the pulse envelope. Another frequently mentioned quantity– the group delay dispersion (GDD), is defined as,

$$GDD = gvd \times L \tag{30}$$

where L is the medium length.

For *o*-polarized beam, the propagation equation is simpler,

$$\begin{aligned} &\tfrac{\partial E(x,y,z,t)}{\partial z} = i\tfrac{1}{2k}\tfrac{\partial^2 E(x,y,z,t)}{\partial^2 x} \\ &+i\tfrac{1}{2k}\tfrac{\partial^2 E(x,y,z,t)}{\partial^2 y} - \tfrac{1}{v_g}\tfrac{\partial E(x,y,z,t)}{\partial t} \\ &-i\tfrac{gvd}{2}\tfrac{\partial^2 E(x,y,z,t)}{\partial^2 t} \end{aligned} \tag{31}$$

2.2 Nonlinear mixing processes

In this section, we will consider the second order nonlinear response of the medium. For higher order effects, interested readers are referred to text book authored by Boyd[16]. Assuming there are two different-color beams present: $E(t) \propto E_1 \exp(i\omega_1 t) + E_1^* \exp(-i\omega_1 t) + E_2 \exp(i\omega_2 t) + E_2^* \exp(-i\omega_2 t)$, we have:

$$\begin{aligned} &E(t)^2 \propto E_1^2 \exp(2i\omega_1 t) + E_1^{*2} \exp(-2i\omega_1 t) \\ &+E_2^2 \exp(2i\omega_2 t) + E_2^{*2} \exp(-2i\omega_2 t) \\ &+2E_1 E_2 \exp\left[i(\omega_1+\omega_2)t\right] + 2E_1^* E_2^* \exp\left[-i(\omega_1+\omega_2)t\right] \\ &+2E_1 E_2^* \exp\left[i(\omega_1-\omega_2)t\right] + 2E_1^* E_2 \exp\left[-i(\omega_1-\omega_2)t\right] \\ &+2\left|E_1\right|^2 + 2\left|E_2\right|^2 \end{aligned} \tag{32}$$

The first two terms correspond to the second harmonic generation(SHG). The third and the fourth terms correspond to the sum-frequency generation(SFG) and difference-frequency generation(DFG) respectively. The last term is the dc rectification term. The energy diagrams are illustrated in figure 10. Next, we will examine the nonlinear mixing wave equations using the SHG and DFG as examples. In chapter 3 and 4, we will review those concepts.

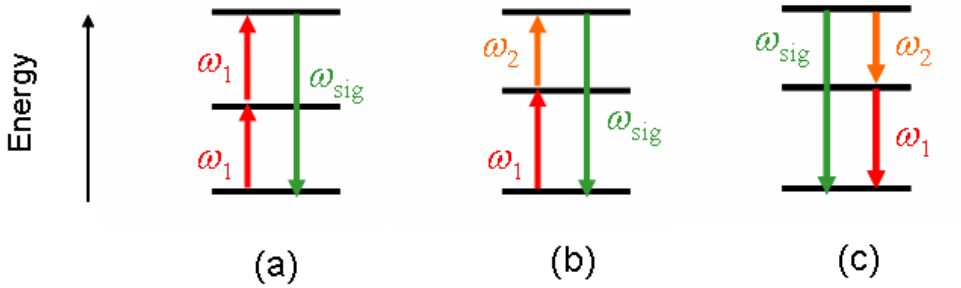

Figure 10: (a)second-harmonic generation. (b)sum-frequency generation. (c)difference-frequency generation.

For the relative simple case of type I SHG, the fundamental wave propagates as an ordinary/extraordinary wave and produces an extraordinary/ordinary wave. The coupled differential equations for the envelopes of the fundamental(subscript 1) and the second harmonic(subscript 3) waves are(for simplicity we assume the field is uniform in the transverse x, y direction):

$$\begin{aligned}(\frac{\partial}{\partial z}+\frac{1}{v_1}\frac{\partial}{\partial t}+i\frac{gvd_1}{2}\frac{\partial^2}{\partial^2 t})E_1(z,t) &= \frac{i\omega_1 d_{eff}}{n_1 c}E_1(z,t)^* E_3(z,t)e^{i\Delta kz}\\ (\frac{\partial}{\partial z}+\frac{1}{v_3}\frac{\partial}{\partial t}+i\frac{gvd_3}{2}\frac{\partial^2}{\partial^2 t})E_3(z,t) &= \frac{i\omega_3 d_{eff}}{n_3 c}E_1(z,t)^2 e^{-i\Delta kz}\end{aligned} \tag{33}$$

where d_{eff} is the effective nonlinear coefficient[16]. $\Delta k = k_3 - 2k_1$ is the phase velocity mismatch for the carrier wave. The wave vectors are often oriented in certain geometry such that phase matching $\Delta k = 0$ is achieved to optimize the conversion efficiency.

We now consider the process that two optical waves with center frequencies ω_3 and ω_1 mix inside a nonlinear medium to generate an output wave at the frequency $\omega_2 = \omega_3 - \omega_1$(see figure 10(c)). The coupled equations that describe this interaction can be written as:

$$\begin{aligned}(\frac{\partial}{\partial z}+\frac{1}{v_1}\frac{\partial}{\partial t}+i\frac{gvd_1}{2}\frac{\partial^2}{\partial^2 t})E_1(z,t) &= \frac{i\omega_1 d_{eff}}{n_1 c}E_2(z,t)^* E_3(z,t)e^{i\Delta kz}\\ (\frac{\partial}{\partial z}+\frac{1}{v_2}\frac{\partial}{\partial t}+i\frac{gvd_2}{2}\frac{\partial^2}{\partial^2 t})E_2(z,t) &= \frac{i\omega_2 d_{eff}}{n_2 c}E_1(z,t)^* E_3(z,t)e^{i\Delta kz}\\ (\frac{\partial}{\partial z}+\frac{1}{v_3}\frac{\partial}{\partial t}+i\frac{gvd_3}{2}\frac{\partial^2}{\partial^2 t})E_3(z,t) &= \frac{i\omega_3 d_{eff}}{n_3 c}E_1(z,t)E_2(z,t)e^{-i\Delta kz}\end{aligned} \tag{34}$$

The phase velocity mismatch is calculated as $\Delta k = k_3 - k_1 - k_2$. This process is known as difference-frequency generation(DFG) or parametric down-conversion. If the wave ω_3 is strong, the field ω_1 is amplified during the mixing process, it is called the optical parametric amplification(OPA). In convention, the ω_1, ω_2 and ω_3 waves are called the signal, idler and pump waves respectively. So far, we implicitly assumed the collinear geometry. In chapter 3, modifications of the above equations will be made to describe a noncollinear beam geometry that matches the group velocities of the pump, signal, and idler pulses, which permits the measurement of broadband pulses.

2.3 Split-step Fourier method

We have shown that the pulse propagation inside a nonlinear optical medium is governed by the following wave equation:

$$\frac{\partial E}{\partial Z} = (\hat{D} + \hat{N})E \tag{35}$$

where $\hat{D}$ represents the differential operator that accounts for dispersion and diffraction, etc. $\hat{N}$ is the nonlinear operator that accounts for the nonlinear optical effects. In general, there are no analytic solutions available and we have to employ numerical approach[75]. The two well known numerical methods are: the finite difference methods and the split-step Fourier transform methods. Among the various finite-difference schemes, the Crank-Nicolson scheme and its variants are the commonly used ones. Details can be found in ref. [60, 75]. In this section, we will discuss the split step methods and later we will apply this method to our problems.

In general, dispersion and nonlinearity acts simultaneously while the pulse propagates through the nonlinear medium. The split-step method pretends they act independently and obtain an approximate solution. Specifically, the medium length is divided into a large number of segments of width h. Over the small distance h, the propagation is calculated in two explicit steps. In the first step, it assumes $\hat{D} = 0$ and let the nonlinearity act alone. In the second step, it assumes $\hat{N} = 0$ and let the

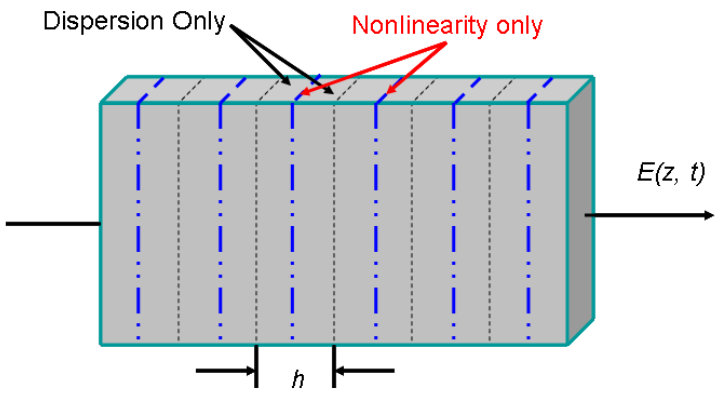

Figure 11: schematic illustration of the split-step Fourier method.

dispersion act alone(see figure 11). The envelope at $z + h$ is approximated by:

$$E(z + h, t) \approx \exp(h\hat{D}) \exp(h\hat{N}) E(z, t) = \exp(h\hat{D}) A(z + h, t) \tag{36}$$

Usually, the operator $exp(h\hat{D})$ is evaluated in the Fourier domain,

$$\exp(h\hat{D}) A(z + h, t) = IFFT\{FFT[\exp(h\hat{D})] FFT[A(z, t)]\} \tag{37}$$

$IFFT$ denotes the inverse Fourier transform. The use of fast Fourier transform(FFT) makes the evaluation of equation 37 relative fast. Compared with typical finite difference schemes, the split-step Fourier methods can be faster by up to two orders of magnitude[1].

CHAPTER III

NUMERICAL SIMULATIONS OF OPA-XFROG

This chapter originally appeared in paper:

Xuan Liu, Aparna Prasad Shreenath, Mark Kimmel, Rick Trebino, Arlee V. Smith, and Stephan Link, "Numerical Simulations of Optical-Parametric-Amplification Cross-Correlation Frequency-Resolved Optical Gating ", JOSA B 23, 318-325(2006)[70].

3.1 Introduction

The past decade has seen great progress in the development of techniques for measuring the intensity and phase vs. time of ultrashort laser pulses. Techniques such as Frequency-Resolved Optical Gating (FROG) and Cross-correlation FROG (XFROG)[67, 93] allow the measurement of a wide range of pulses. While these techniques have achieved fairly high sensitivity, they are not sufficient to measure extremely weak ultrashort light pulses-pulses with only a few photons—whose measurement would often help to elucidate important fundamental light-emission processes[73].

While spectral interferometry can measure the intensity and phase of trains of $\sim$1-photon pulses[42], interferometric methods unfortunately involve extremely stringent coherence requirements, including the need for precise mode-matching, nearly perfect spatial coherence, and highly stable absolute phase (carrier-envelope phase) from pulse to pulse in the train. While these conditions can be met by laser pulses, they are rarely met by light pulses (pulses not directly emitted by a laser), such as fluorescence, Raman scattering, and super-continuum. As a result, we introduced a non-interferometric technique that avoids such restrictive coherence requirements and which achieves few-photon sensitivity to help elucidate such fundamental weak-light emitting processes in many fields[107]. It is a variation on the XFROG method and

hence involves measuring a time-gated-pulse spectrum vs. delay to yield a visually intuitive spectrogram of the weak pulse. Unlike previous FROG methods, however, the gating process involves gain. Using either Optical Parametric Amplification (OPA) or Difference Frequency Generation (DFG) with an intense, higher-frequency, shorter gate pulse, we showed that it is possible to gate in time with a simultaneous gain of up to $\sim 10^6$. Like previous FROG and XFROG techniques, OPA and DFG XFROG do not require mode-matching, spatial coherence, or stability of the absolute phase.

OPA XFROG and DFG XFROG have additional advantages over interferometric methods. For example, another obstacle to the use of spectral interferometry for measuring weak pulses in many applications (even when the coherence requirements are met) is the lack of a well-characterized reference pulse whose spectrum contains that of the unknown weak pulse. Fortunately, appropriate reference pulses are much more readily available for OPA and DFG XFROG. This is because the creation of ultraweak fluorescence or Raman scattering pulses requires its own excitation pulse, which itself must have three characteristics: 1) it must have a shorter wavelength, 2) it must be shorter in duration, and 3) it must be relatively intense. Coincidentally, these are precisely the three conditions for the reference pulse in OPA and DFG XFROG! Thus, for this wide range of cases, an ideal reference pulse for OPA and DFG XFROG is guaranteed to be available. OPA XFROG and DFG XFROG are thus ideal for measuring such ultraweak ultrashort light pulses as luminescence or Raman scattering.

OPA, DFG, and stimulated Raman scattering (SRS) processes have been used for gating or gain in many situations previously[49, 82, 94, 100, 105]. One particularly relevant case has been the simultaneous use of gating and gain in ballistic-imaging techniques[17, 74] where few-photon unscattered pulses containing the desired image must be time-gated. Their adaptation to ultrashort-pulse intensity-and-phase measurement was perhaps overdue. The high gain available from these processes,

which allows us to significantly amplify ultraweak light pulses, increases the sensitivity in light-pulse-measurement applications by many orders of magnitude. We simply used a slightly modified FROG algorithm to retrieve the intensity and phase of the ultraweak pulse from the measured OPA XFROG spectrogram(See chapter 1).

Previously, we demonstrated OPA XFROG by measuring trains of pulses as weak as 50 aJ (a few hundred photons) per pulse[107]. Indeed, because our repetition rate was 100,000 times lower in this work than in our previous spectral-interferometry weak-pulse measurement[42], the total number of photons required for our measurement was actually less than in the previous less-than-one-photon-per-pulse spectral-interferometric measurement.

In our previous work on OPA XFROG, a question that remained unanswered was the trade-off between accuracy and efficiency. Specifically, the accuracy requirement involves minimizing the group-delay mismatch (GDM) in the crystal between the two (or three) pulses involved in order to minimize geometrical smearing of the temporal features of the pulse to be measured, which otherwise would yield inaccurate results. The efficiency requirement, on the other hand, involves maximizing the gain in the OPA or DFG crystal. Short crystals, which typically achieve minimal GDM (GDM $\propto L$, where L is the crystal length) and hence yield high OPA XFROG accuracy, also yield minimal gain, while longer crystals required for high gain also tend to have large GDM and thus tend to potentially yield some distortion in the measurement.

Fortunately, a similar problem has cropped up previously, and that is in OPA devices for efficiently transforming pulses from one wavelength to another. In that field, this problem was solved by use of non-collinear OPA (NOPA)[84] beam geometries with a few degrees between the two beams, which yield considerably larger phase-matching bandwidths or, equivalently, much smaller GDM. Clearly the NOPA concept will also solve the problem in OPA XFROG measurements. The OPA XFROG problem, however, is somewhat different from that of NOPAs for efficient wavelength

conversion. While efficiency is the predominant goal in NOPAs, whose only desire with respect to the signal pulse intensity-and-phase curve is that it have about the same pulse length as the input pump pulse, our requirement is much more stringent: we require that the intensity and phase of this pulse be such that it can be accurately modeled and, in particular, we'd prefer it to have the ideal form:

$$E_{sig}^{OPA}(t,\tau) = E(t)\, E_{gate}^{OPA}(t-\tau), \tag{38}$$

where $E(t)$ is the unknown input pulse; the second factor is the gate function, given by[16]:

$$E_{gate}^{OPA}(t) = \cosh(g\,|E_{ref}(t)|\,z). \tag{39}$$

where $E_{ref}(t)$ is the reference (pump) pulse and g is the gain parameter,

$$g^2 = \frac{4\pi^2 d_{eff}^2}{n_{OPA} n_{DFG} \lambda_{OPA} \lambda_{DFG}}. \tag{40}$$

On the other hand, OPA XFROG has the simplification that it does not involve efficient conversion of the pump pulse energy to the signal. In other words, OPA XFROG, unlike wavelength-conversion NOPAs, does not operate in the pump-depletion regime. This is a major simplification.

Our goal is therefore to model the OPA XFROG process for typical experimental conditions, checking the accuracy of OPA XFOG measurements of weak pulses for typical gains. We show that few-degree crossing angles between the beams, as is common in FROG beam geometries and NOPAs, yields excellent accuracy with large bandwidths in such measurements even in the presence of high gain. We perform an experiment on spectrally filtered continuum with $\sim$ 100 nm of bandwidth. Finally, we also consider DFG XFROG as well and show that our simple model works just as faithfully for DFG XFROG as it does for OPA XFROG-our theoretical simulations show that it is possible to retrieve the signal pulse by making either an OPA measurement or a DFG measurement and applying the suitable XFROG algorithm to it.

3.2 OPA/DFG XFROG

The FROG and XFROG techniques both involve using a gate pulse to gate the unknown pulse. In FROG, the gate pulse is the pulse itself. However, when a well-characterized reference pulse is available, it is generally better to use it as the gate pulse, and this technique (spectrally resolved cross-correlation in conjunction with an algorithm to extract the pulse intensity and phase) is generally referred to as XFROG. The standard FROG algorithm is easily modified to deal with XFROG. The expression for an XFROG trace is[93]:

$$I_{XFROG}(\omega,\tau) = \left| \int_{-\infty}^{\infty} E(t) E_{gate}(t-\tau) \exp(-i\omega t)\, dt \right|^2 \tag{41}$$

where the gate function, $E_{gate}(t)$, can be any function (i.e., pulse) that happens to be available and which has temporal structure on the order of that of the pulse to be measured, $E(t)$. More generally, all that is required is a signal field that is a function of time and delay, an example of which is a product of the form, $E(t)E_{gate}(t-\tau)$, which can then be spectrally resolved.

A schematic of the apparatus for both OPA XFROG and DFG XFROG is shown in Figure 12. In OPA XFROG, the weak pulse (labeled $E(t)$) is parametrically amplified in the crystal by the more intense reference-gate pulse. The DFG XFROG signal pulse is also shown. Either pulse can be spectrally resolved to yield an OPA XFROG or DFG XFROG trace.

In this section we will discuss a simplified theory of OPA/DFG in the framework for deriving a simplified algorithm for OPA/DFG XFROG. We will revisit the theory more rigorously in the next section. The coupled-wave equations for the generation of both the signal and idler (which we will refer to here as the OPA and DFG pulses, respectively, because the term, "signal," is already used in FROG and has a different meaning) are [16]:

$$\frac{\partial E_{OPA}}{\partial z} = i\kappa E_{ref} E^*_{DFG} \tag{42}$$

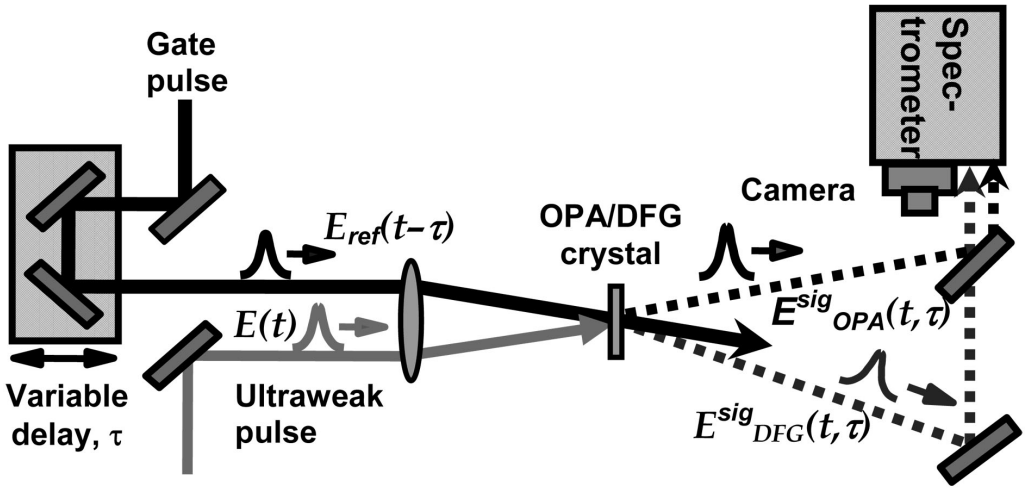

Figure 12: Schematic of the experimental apparatus for OPA/DFG XFROG.

$$\frac{\partial E_{DFG}}{\partial z} = i\kappa' E_{ref} E^*_{OPA} \tag{43}$$

where $\kappa = 2\pi d_{eff}/(n_{OPA}\lambda_{OPA})$ and $\kappa' = 2\pi d_{eff}/(n_{DFG}\lambda_{DFG})$. Here phase-matching is assumed, so that $\Delta k = 0$.

Assuming negligible pump depletion, the electric field of the signal pulse emerging from the crystal in an OPA XFROG apparatus has the form of equation (38) where $E(t)$ is the unknown input pulse. The second factor is the gate pulse and is given by equation (39). Thus the pulse to be measured undergoes exponential gain during OPA and yet retains its phase during the process.

The setup for DFG XFROG is similar to that of OPA XFROG, except that now the idler is imaged onto the slit of the spectrometer to yield a DFG XFROG trace. Although it is known that DFG XFROG is a sensitive technique for measuring fairly weak pulses[67], the method has never been demonstrated with gain. Here we consider the effect of possible gain, so that the electric field is given by:

$$E^{DFG}_{sig}(t,\tau) = E(t)^* E^{DFG}_{gate}(t-\tau). \tag{44}$$

This has the same unknown input pulse but a gate function of the form:

$$E^{DFG}_{gate}(t) = \exp[i\phi_{ref}(t)] \sinh(g|E_{ref}(t)|z), \tag{45}$$

where $\phi_{ref}(t)$ is the phase of the reference pulse. In the limit that the reference pulse is weak, the net gain is small, and the above expression reduces to $E_{gate}^{DFG}(t) = E_{ref}(t)$.

The measured XFROG trace is simply the magnitude-squared Fourier transform of the various signal fields.

In both OPA and DFG XFROG, the unknown pulse is easily retrieved from the measured trace using the iterative XFROG algorithm, modified for the above expressions for the gate pulse.

In the above treatment we have neglected the effect of group velocity mismatch (GVM) between the interacting pulses[18, 21, 89]. GVM between the pump and signal pulses constrains the interaction length over which parametric amplification occurs. The larger the GVM, the shorter the actual interaction length will have to be. GVM depends on the crystal, the various pulse wavelengths, and the type of phase-matching. Defining the pulse-splitting length l_{sp} as the propagating distance after which the pump and signal pulses separate from each other by a pulse length, it is known that GVM effects can be neglected in light-generation experiments to a first approximation for the cases where the crystal lengths are shorter than the pulse splitting length:

$$l_{sp} = \frac{\tau_p}{GVM_{sp}} \tag{46}$$

where τ_p is the length of the longer of the signal or pump pulse. In using OPA or DFG for pulse measurement, however, one must be careful to avoid allowing the gate pulse to walk more than one coherence time (usually less than one pulse length) with respect to the pulse to be measured, or the gate pulse will sample a range of pulse intensities and phases, not the correct intensity and phase for a particular delay. The next section will discuss the effect of including GVM and also the second order dispersion effects in the theoretical simulations.

3.3 Theory

In this section, we will investigate the theory of OPA/DFG more rigorously. We derive a set of equations to describe the parametric mixing process of three temporally structured waves that propagate at different angles. Without loss of generality, we align the incident face of the crystal along the xy-plane, so that the beam propagation directions lie nearly parallel to the axis. We begin with the nonlinear parametric wave equations[16],

$$\nabla \times \nabla \times \bar{\mathbf{E}}_s = \mu_0 \omega_s^2 (\varepsilon \cdot \bar{\mathbf{E}}_s + \varepsilon_0 2\mathbf{d} \cdot \bar{\mathbf{E}}_p \bar{\mathbf{E}}_i^*) \tag{47}$$

$$\nabla \times \nabla \times \bar{\mathbf{E}}_i = \mu_0 \omega_i^2 (\varepsilon \cdot \bar{\mathbf{E}}_i + \varepsilon_0 2\mathbf{d} \cdot \bar{\mathbf{E}}_p \bar{\mathbf{E}}_s^*) \tag{48}$$

$$\nabla \times \nabla \times \bar{\mathbf{E}}_p = \mu_0 \omega_p^2 (\varepsilon \cdot \bar{\mathbf{E}}_p + \varepsilon_0 2\mathbf{d} \cdot \bar{\mathbf{E}}_s \bar{\mathbf{E}}_i) \tag{49}$$

where $\bar{\mathbf{E}}_j$ is the electric field in its phasor form. In accordance with OPA conventions, $j = s, i$ and p refers to the signal (seed), idler, and pump, respectively. Also, ε and $\mathbf{d}$ refer to the permittivity and the nonlinear coefficient tensor respectively.

In the following derivation we assume monochromatic plane waves with infinite extent in the xy-plane, for convenience. The fields with k-vectors tilted away from the z-axis are represented by:

$$\begin{aligned} \bar{\mathbf{E}}_j &= \mathbf{E}_j(z) e^{i\mathbf{k}_j \cdot \mathbf{r}} \\ &= \hat{\mathbf{e}}_j \mathbf{E}_j e^{i(k_{jx}x + k_{jy}y + k_{jz}z)} \\ &= (\hat{x}E_{jx} + \hat{y}E_{jy} + \hat{z}E_{jz}) e^{i(k_{jx}x + k_{jy}y + k_{jz}z)} \end{aligned} \tag{50}$$

Applying the slowly-varying-amplitude approximation to equation (47), we derive the following expression after some standard mathematical manipulations:

$$\begin{aligned} &\hat{x}(-2ik_{sz}\tfrac{\partial E_{sx}}{\partial z} + ik_{sx}\tfrac{\partial E_{sz}}{\partial z}) + \hat{y}(-2ik_{sz}\tfrac{\partial E_{sy}}{\partial z} + ik_{sy}\tfrac{\partial E_{sz}}{\partial z}) \\ &+\hat{z}(ik_{sx}\tfrac{\partial E_{sx}}{\partial z} + ik_{sy}\tfrac{\partial E_{sy}}{\partial z}) = 2\mu_0\varepsilon_0\omega^2 \mathbf{d} \cdot \mathbf{E}_p \cdot \mathbf{E}_i^* e^{i(k_p \cdot r - k_s \cdot r - k_i \cdot r)}. \end{aligned} \tag{51}$$

The other two mixing equations (for the idler and the pump) have the same form, as well.

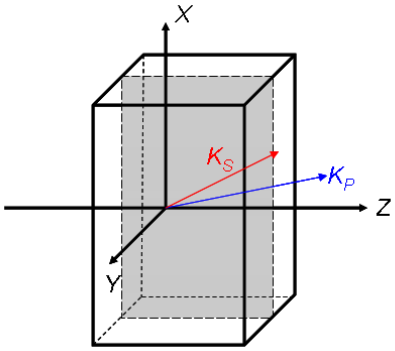

Figure 13: The geometry of the nonlinear process inside the crystal .

Although the beams could tilt away from the z-axis in any direction, in practice they are usually tilted along one of the polarized planes. Here, we assume that the k-vectors all lie in the xz-plane as shown in Figure 13. We let the signal beam propagate at an angle α_s with respect to the z-axis; it will walk off by an angle ρ_s toward the x-direction if it is x-polarized and it will walk off by zero in the y-direction if it is y-polarized. So, for x- or y- polarized beams, respectively, we have:

$$\hat{e}_s = \begin{cases} \hat{x}\cos(\alpha_s + \rho_s) - \hat{z}\sin(\alpha_s + \rho_s) & x - polarized \\ \hat{y} & y - polarized \end{cases} \tag{52}$$

Taking dot product of $\mathbf{E}_s$ on both sides of equation (51), we obtain:

$$\frac{\partial E_s}{\partial z} = \frac{i\omega_s}{\tilde{n}_s c} d_{eff} E_p E_i^* e^{i\Delta kz}. \tag{53}$$

The corresponding equations for the idler and pump will then be:

$$\frac{\partial E_i}{\partial z} = \frac{i\omega_i}{\tilde{n}_i c} d_{eff} E_p E_s^* e^{i\Delta kz} \tag{54}$$

$$\frac{\partial E_p}{\partial z} = \frac{i\omega_p}{\tilde{n}_p c} d_{eff} E_s E_i e^{-i\Delta kz} \tag{55}$$

where $\Delta k = k_{pz} - k_{sz} - k_{iz}$ is the phase mismatch. $\mathbf{d}_{eff} = d \cdot \hat{\mathbf{e}}_s \hat{\mathbf{e}}_i \hat{\mathbf{e}}_p$ is the effective nonlinearity and $\tilde{n}_j$, the effective refractive index, is defined by:

$$\tilde{n}_j = \begin{cases} n_j \cos\rho_j \cos(\alpha_j + \rho_j) & x - polarized \\ n_j \cos\alpha_j & y - polarized \end{cases} \tag{56}$$

For a pulse with temporal structure, the linear propagation of the envelope is given by[1]:

$$\frac{\partial E(t,z)}{\partial z} = -\frac{1}{V_{gz}}\frac{\partial E(t,z)}{\partial t} - i\frac{1}{2}\left(\frac{\partial^2 k_z}{\partial \omega^2}\bigg|_c\right)\frac{\partial^2 E(t,z)}{\partial t^2} + ..., \tag{57}$$

where V_{gz} is the group velocity along the z-axis. For a noncollinear mixing process, the group velocity and the group delay dispersion factors will be modified[89]. Here we call them the apparent group velocity and apparent group delay dispersion and indicate them by $\hat{V}_g$ and $\hat{D}$(See appendix B) :

$$\hat{V}_g = V_{gz} = V_g\frac{\cos(\alpha+\phi+\rho)}{\cos\phi\cos\rho} \tag{58}$$

and

$$\begin{aligned}\hat{D} &= -\tfrac{1}{2}\tfrac{d^2k_z}{d\omega^2} = \tfrac{1}{2V_g^2}\tfrac{\cos\phi\cos\rho}{\cos(\alpha+\phi+\rho)}GVD \\ &+\tfrac{1}{V_g^2}\tfrac{\cos\phi\cos^3\rho\sin^2(\alpha+\phi)}{\cos^3(\alpha+\phi+\rho)}A\end{aligned} \tag{59}$$

Here V_g is the group velocity along the direction of the k-vector of the pulse's carrier wave and $GVD = \partial v/\partial\omega$ relates to the ordinary group-velocity dispersion. ϕ is the slant angle of the pulse front relative to the normal to the z axis (See figure 14). α is the tilt angle of the propagation vector. The apparent group delay dispersion is slightly different from the equation in the Optics Letter[89], which includes a more accurate coefficient for diffraction. Instead of using $1/(2k)$ we now use A[34],

$$A = \frac{1}{2k} - \frac{1}{2k^2}\frac{\partial^2 k}{\partial\alpha^2} \tag{60}$$

Normally, the second and fourth term in the apparent group velocity dispersion are quite small and can be neglected. Substituting the above expressions into equations (47-55), we then have the wave equations for noncollinear parametric mixing:

$$\frac{\partial E_j}{\partial z} + \frac{1}{\hat{V}_{gj}}\frac{\partial E_j}{\partial t} - i\hat{D}\frac{\partial^2 E_j}{\partial t^2} = \tilde{P}_j \tag{61}$$

where

$$\tilde{P}_s = \frac{i\omega_s}{\tilde{n}_s c}d_{eff}E_pE_i^*e^{i\Delta kz} \tag{62}$$

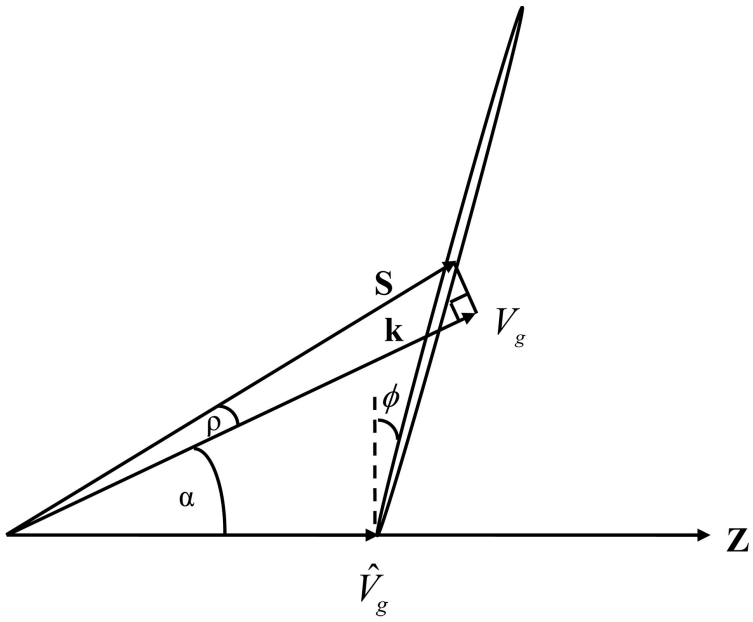

Figure 14: The apparent group velocity ($\hat{V}_g$) of a slanted pulse.

$$\tilde{P}_i = \frac{i\omega_i}{\tilde{n}_i c} d_{eff} E_p E_s^* e^{i\Delta kz} \tag{63}$$

and

$$\tilde{P}_p = \frac{i\omega_p}{\tilde{n}_p c} d_{eff} E_s E_i^* e^{-i\Delta kz} \tag{64}$$

In the simulations that follow, we will use equations (61-64). We will discuss the possible distortions that occur in the signal pulse after parametric amplification due to GVM and group velocity dispersion (GVD) effects.

In order to improve mixing efficiency, it is desirable to adjust the three interacting beams to propagate with the same group velocity along a common axis. A. V. Smith has demonstrated[89] that it is possible to achieve exact group-velocity matching of all three pulses by use of a combination of pulse-front tilt (We can use prisms and gratings to induce the appropriate pulse-front tilt[32].) and noncollinear phase matching. Figure 15 shows the geometry of the noncollinear amplification for our experiments. For convenience, we choose the common axis of propagation to be the z-axis and align $\hat{k}_p$ along $\hat{z}$. Ideally a short pump pulse travels with the same group velocity as the signal and idler and strongly amplifies a short segment of the signal

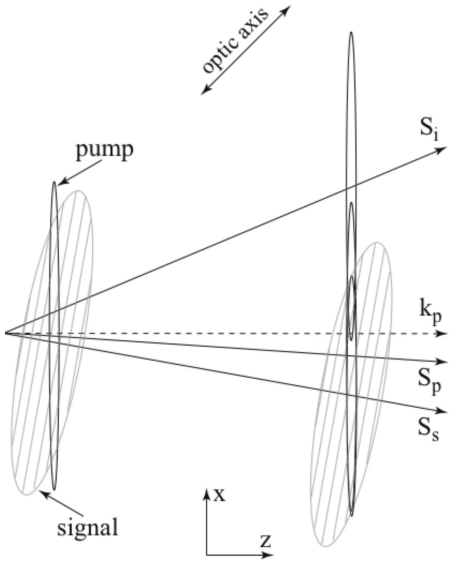

Figure 15: Model axes.The signal crosses the pump, which is parallel to $\hat{z}$, at an angle.

pulse. At the input end of the crystal there is a short, strong pump pulse and a weak, longer signal pulse. At the output end of the crystal, coincident with the pump pulse, there is a strong idler pulse and a strong segment of the signal pulse, plus the weak, unamplified signal pulse. For the geometry used in this paper there is no pulse front tilt for the pump pulse. The delay between the input signal and pump pulses is swept to generate a XFROG trace. The length of the crystal, and consequently the value of parametric gain, is limited by the apparent group velocity dispersion of the crystal. This stretches the pulses in time and distorts their phases, resulting in distortion of the XFROG traces. We assume the beams are large and uniform in irradiance in the transverse dimension so diffraction and transverse irradiance profiles can be ignored in our simulations. If the signal and idler have the same group velocity and group velocity dispersion is ignored, the amplified signal and the idler replicate the phase of the input signal. If their group velocities' differ, the signal phase is distorted in amplification. If the pump group velocity also matches the signal and idler group velocity the duration of the time gate is minimized, increasing the time resolution of the XFROG measurement.

3.4 Numerical Simulation Results

Using a configuration typical for our experiments, we simulate the OPA-XFROG process for broadband measurements. We consider Type I phase matching conditions in a BBO crystal. The signal is an 850-fs long pulse centered at about 600 nm, and the pump is a 120-fs long pulse at 390 nm. The input energies of the signal and pump pulses are 5 fJ and 8 μJ per pulse, respectively. For a type I parametric process, we find the crossing angle between the pump and the signal beams that permits group-velocity-matched mixing to be 7.15° using the nonlinear optical software, SNLO[88]. We assume Gaussian temporal input profile for our pulses. The FWHM beam diameters for the signal and pump are 200 μm and 300 μm respectively. We also assume that the phase-matching conditions are satisfied. For all the calculations, $d_{eff} = 1.8$ pm/V is used. The number of time steps is 512.

We now investigate the effect of different crystal thicknesses, as well as different beam crossing angles on pulse retrievals using the OPA XFROG algorithm. Unless specified otherwise, we use the above parameters in our calculations.

To establish a baseline for our simulations, we first define a linearly chirped broadband pulse for use in all simulations. We then generate an OPA XFROG signal trace by numerically solving equations (61)-(64)(See appendix A) in a 2-mm Type I BBO crystal for the ideal case, that is, with all three pulses traveling at exactly the same group velocity and with no group velocity dispersion. The resulting ideal-case OPA XFROG trace of this pulse is shown in figure 16 (a). Its retrieved trace is shown in figure 16 (b) using the OPA XFROG algorithm, which yields a very low frog error. Figures. 16 (c) and (d) show the retrieved temporal/spectral pulse intensities and phases compared with the actual pulse temporal/spectral intensities and phases(The solid lines with circular markers in (c) and (d) show the retrieved temporal and spectral intensities of the pulse. The dotted lines with circular markers refer to the retrieved signal temporal and spectral phases. The solid lines without any markers

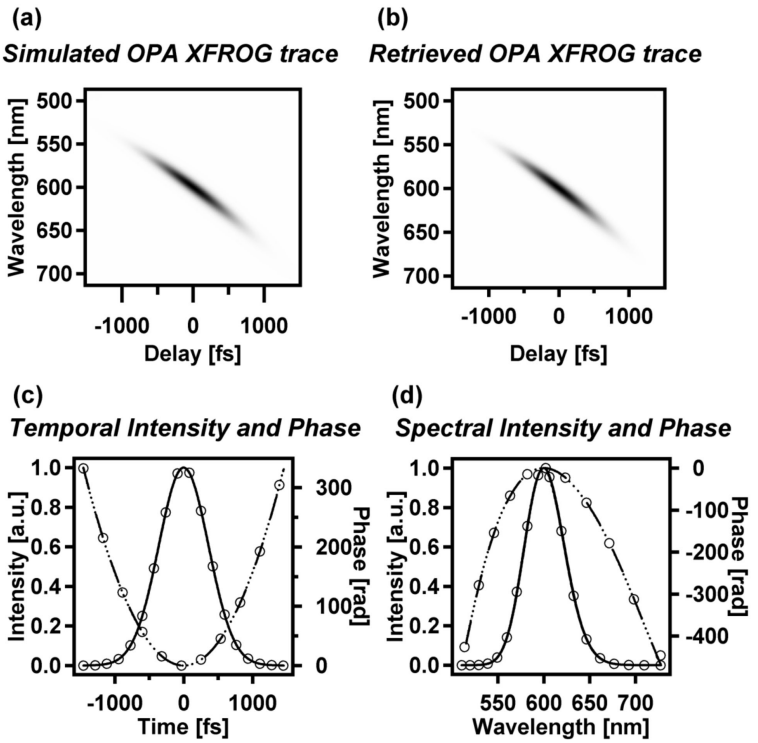

Figure 16: An Ideal case of OPA XFROG

refer to the intensities of the actual pulse. The dashed lines without any markers are the corresponding phases of the actual pulse. These conventions are maintained in the remaining figures in this chapter.). As can be seen from the figure, the agreement is excellent. Both the retrieved and the actual pulses have the same FWHM of 72 nm. The FROG error was 4.339E-005.

In our experiments, we have found that we can make accurate OPA XFROG measurements using 2-mm BBO crystals with very little GVM-induced distortion if we cross the pump and the signal at an angle of 7.15°. So we simulated this case, and our simulations bear this out (See figure 17). The FWHM of the retrieved signal pulse is estimated to be 63 nm, which is 9 nm narrower than the ideal 72 nm input seed pulse. The peak parametric gain is found to be 1.2 x 10^7 (higher than we observe experimentally, but this is to be expected due to mode-quality and alignment effects) and no pump depletion is observed. The temporal and spectral phases retrieve quite

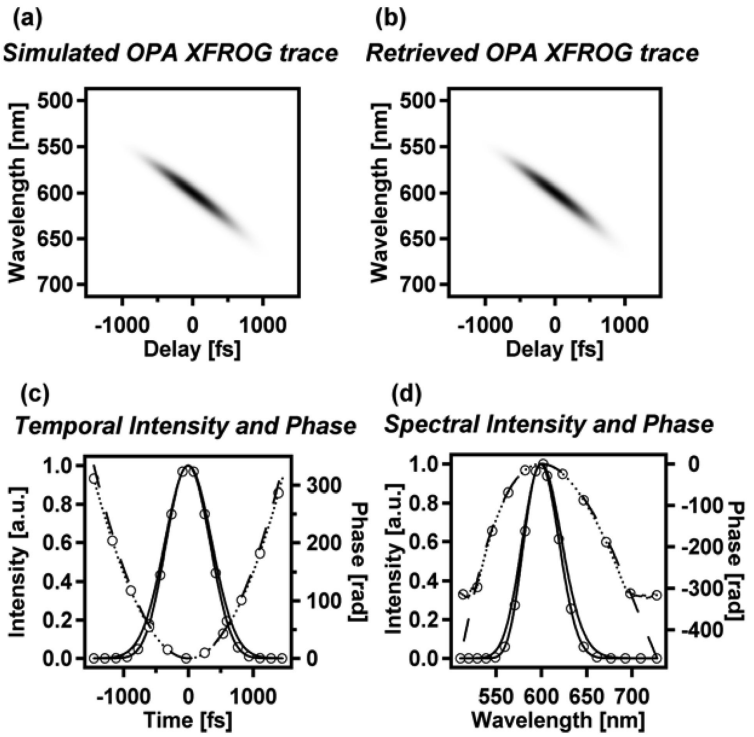

Figure 17: OPA XFROG trace and its retrieval with a 2-mm thick BBO

well. Overall, the retrieved pulse shows a very low FROG error of about 4.102E-004. For our case, when the crossing angle is taken to be 7.15°, the group velocities between the three pulses are almost equal along the propagation axis (z-axis). Thus, the bandwidth narrowing effect due to GVM is negligible. Any narrowing is mainly caused by the GVD. GVD becomes more significant in thicker crystals. Figure 18 shows OPA XFROG trace of the signal and its retrieval with 3 mm BBO . Here in order to avoid depletion, we use a 2 μJ pump. The FROG error was 4.254E-004. The peak parametric gain is now lower, about 1.5 x 10^5. Using thicker crystals, we can use correspondingly weaker pumps and still achieve fairly high gains. However, the distortions caused by GVD are quite significant. The retrieved signal pulse has a FWHM of 57 nm.

With thicker crystals, the parametric gain increases greatly, and pump depletion may occur. This is undesirable, as it will yield distortions analogous to those of second-harmonic-generation-based pulse-measurement devices in the depletion regime.

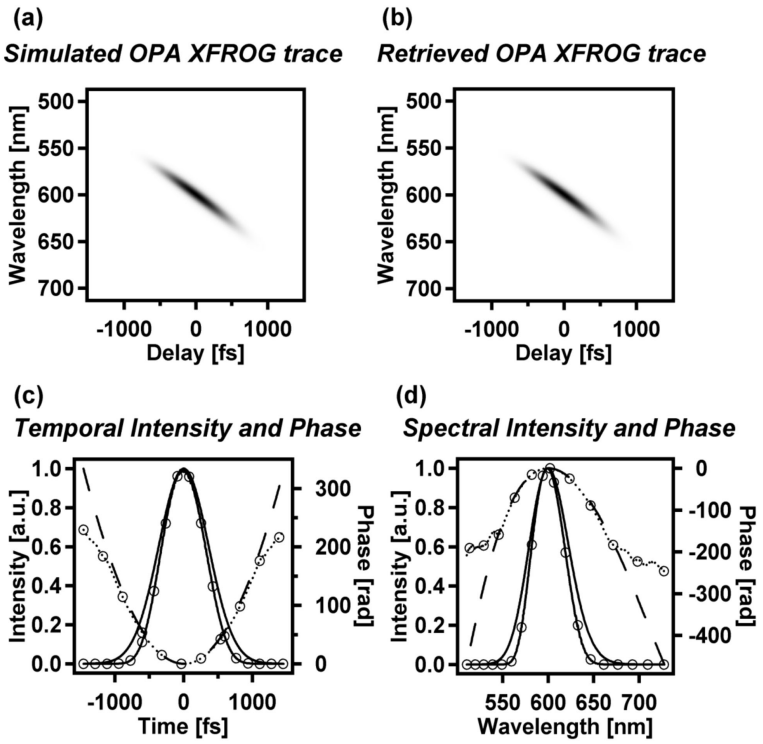

Figure 18: OPA XFROG trace of the signal and its retrieval with 3 mm BBO

For our OPA configuration, keeping the pump energy fixed at 8 μJ in a thicker crystal yields pump depletion, so we will reduce it accordingly. This is reasonable, as OPA XFROG rarely requires more than a few pJ of OPA signal pulse energy to make a measurement.

In fact, there will be fewer distortions in the signal pulse when thinner crystals are used. At the same time, we can use a stronger pump to maintain a high gain. Figure 19 shows the case of a 1-mm thick BBO crystal with a 30 μJ pump. The peak parametric gain is about 7 x 10^6. We observe minimal spectral narrowing due to the parametric process. Our OPA XFROG algorithm retrieves the input signal pulse with a very low error of 2.547E-004. The bandwidth of the retrieved pulse is 69 nm.

In all these above cases, interestingly, the spectral phase is always quite accurately retrieved. We can reach a good compromise between large parametric gains and low pulse distortions that arise principally due to GVD effect and pump depletion, by

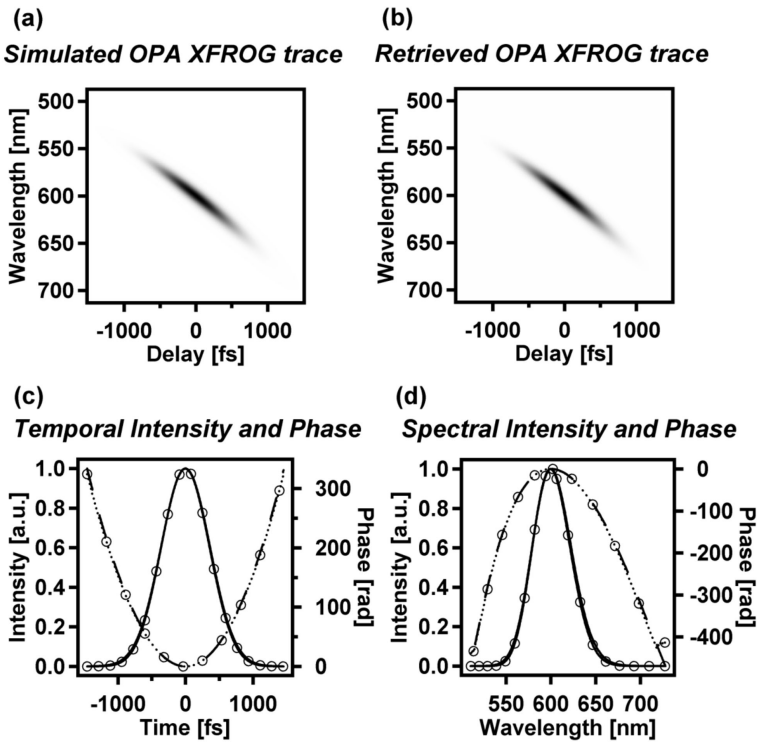

Figure 19: OPA XFROG trace of the signal and its retrieval with 1-mm BBO

choosing a suitable crystal length for a given initial pump energy.

For our measurements, group velocity matching is a very important factor. Even a slight temporal walk-off will distort the signal pulse. Thus, choosing the right crossing angle between the pump pulse and the input pulse is very critical. In the following analysis for various beam crossing angles, we use a crystal thickness of 2 mm. Figures (20-23) show XFROG traces of the signal and their retrievals with the crossing angles of 0°, 3°, 6.52° and 10°, respectively.

For the collinear geometry, $\alpha_s = 0°$, we obtain a pulse with only 14 nm of bandwidth after parametric amplification (See figure 20). The FROG error was 5.250E-3. When the signal is tilted away from the pump by a small angle of 3°, the signal bandwidth is increased to be 16 nm (See figure 21). The FROG error was 5.844E-003. When the signal and the pump are crossed at 6.52°, the retrieved pulse has a bandwidth of 50 nm (See figure 22). The FROG error was 1.500E-003. If we deviate from the ideal crossing angle, 7.15° in the other direction and use 10° instead, the

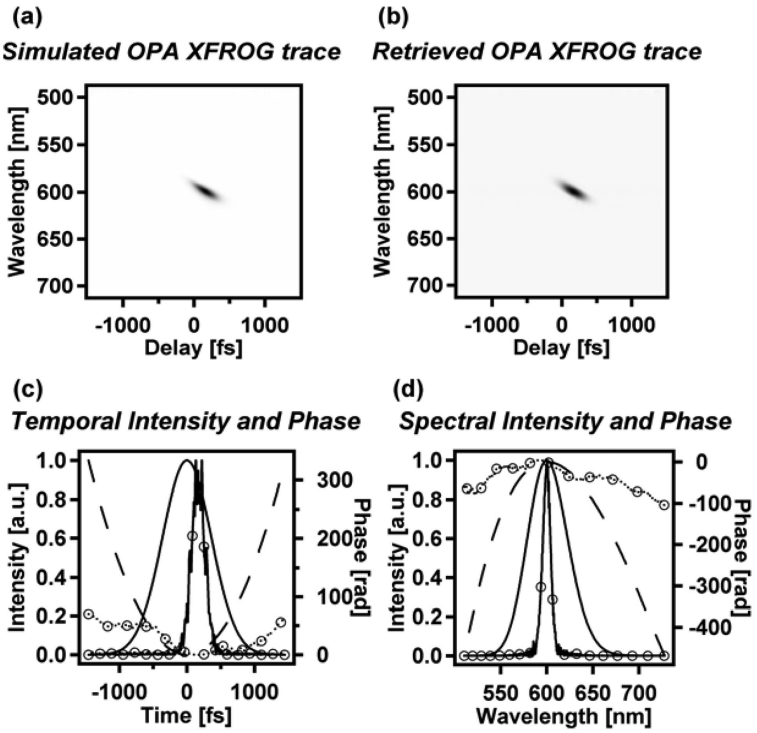

Figure 20: OPA XFROG trace and its retrieved pulse with collinear beams

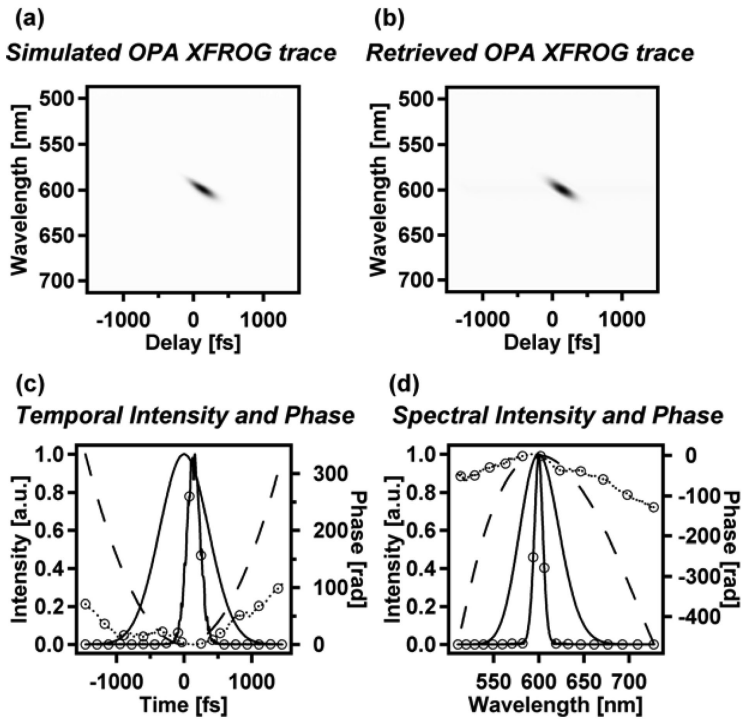

Figure 21: OPA XFROG trace and its retrieved pulse with crossing angle $\alpha_s = 3°$

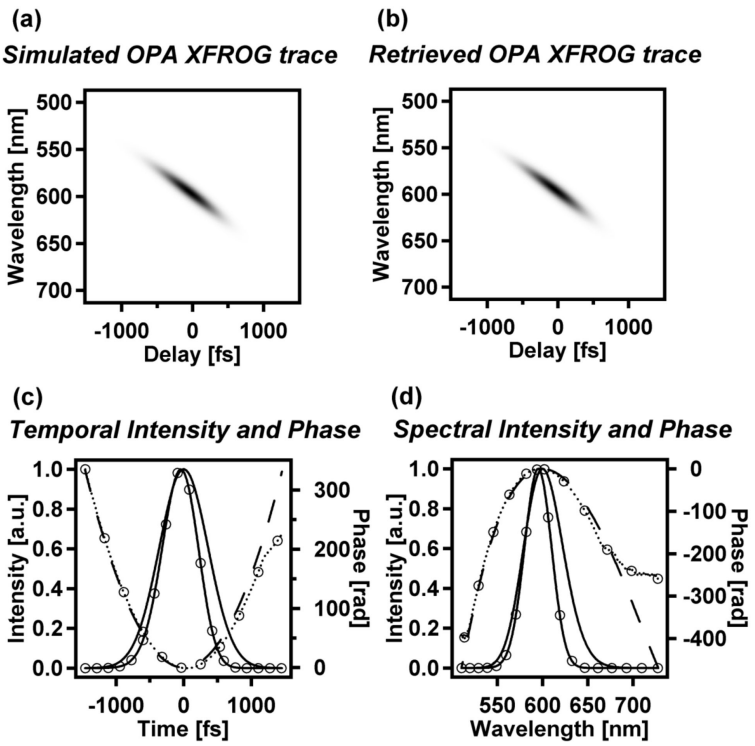

Figure 22: OPA XFROG trace and its retrieved pulse with a crossing angle $\alpha_s = 6.52°$

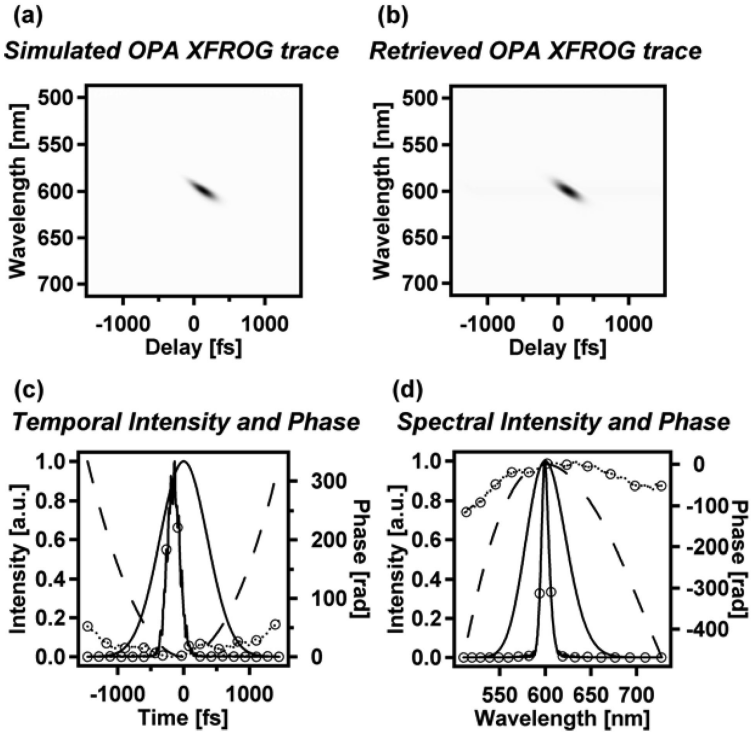

Figure 23: OPA XFROG trace and its retrieved pulse with a crossing angle $\alpha_s = 10°$

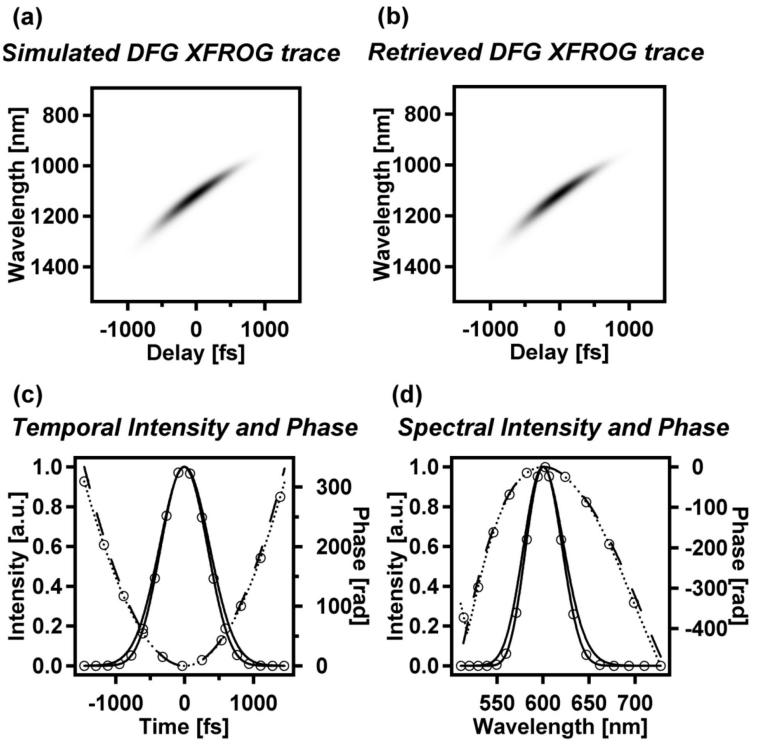

Figure 24: DFG XFROG trace of a pulse and its retrieval

bandwidth decreases to be 14 nm (See figure 23). The FROG error was 5.863E-003. Clearly, for broadband pulses, the GVM condition is critical.

We now show simulations of DFG XFROG, which also allows the measurement of pulses with gain. We consider the same configurations as for OPA XFROG in a 2-mm Type I BBO crystal with a 7.15° crossing angle between the signal and pump, but now we focus on the idler pulse and attempt to retrieve the visible broadband input pulse. We plot the DFG XFROG traces and the retrieved pulses in figure 24 using the same pulse and configurations as in figure 17. The FROG error was 5.922E-004.

The signal pulse was retrieved using the gate function given in equation (45) and has a FWHM of 63 nm, which is identical to what we retrieved from the corresponding OPA XFROG geometry. The FROG error in this case was fairly low, around 5.922E-004.

3.5 Experiment

The schematic for our experimental setup for OPA/DFG XFROG is shown in figure 12. Either the signal or the idler pulse can be spectrally resolved to yield an OPA XFROG or DFG XFROG trace. We use a KM Labs Ti:Sapphire oscillator, amplified using a kHz-repetition-rate regenerative amplifier to create a strong 800 nm pulse. We characterized this pulse using a Swamp Optics GRENOUILLE Model 8-50. The pulse was frequency doubled in a 1 mm thick Type-I BBO crystal with a deliberately low conversion efficiency of 15%. The fundamental and the second harmonic pulses were separated to form the first component of the OPA XFROG device. In one arm of the XFROG set-up, the fundamental pulse was used to generate a white-light continuum (with poor spatial coherence) in a 2-mm thick sapphire plate, which was then spectrally filtered using a combination of BG40 and OG515 filters to yield a slice of the spectrum about 60 nm wide centered on 600 nm. This energy of the filtered pulse was 500 pJ but it was attenuated by a factor of 105 using ND filters to yield a 5 fJ pulse. This "unkonwn" pulse was focused into the 2-mm thick Type-I BBO crystal using a 100-mm focal length lens. The spot-size at the crystal for the pump and the seed pulses was 265 microns and 120 microns respectively. The 8.0 μJ, 400 nm second harmonic pulse in the other arm of the XFROG device passed through a variable length path to provide the variable gate pulse delay. This pump pulse was focused into the nonlinear crystal separately from the white light using a 75-mm focal length spherical mirror. The white light and the pump pulse crossed at an internal angle of 6.5° in the BBO crystal. The thickness of the crystal was short enough that the effects of GVM were small compared to the pulse length permitting use of the simple gate functions described above. This geometry provided ample phase-matching bandwidth to cover the seed pulse bandwidth. The resulting OPA signal at the CCD array was integrated over a few seconds. The OPA signal emerging from the BBO crystal experienced an average gain (G) of about cosh(8)$\sim$ 1490 (See figure

25), which, in view of the weak pulses involved, still easily satisfied the condition of negligible pump depletion. This gain was less than predicted by our simulation, but beam alignment and beam quality issues probably account for this. The observed gain was more than sufficient to record the spectrally dispersed OPA XFROG signal at the camera. The OPA XFROG retrieved pulse had a FROG error of 0.0216. Its duration was approximately 850 fs with a spectral width of 60 nm. The fine structure in the retrieved intensity and spectrum complicated an exact FWHM determination, so we estimated these values from a fitted curve. Although these numbers implied a small amount of distortion due to GVM, in light of our earlier simulations, we chose what we considered a happy medium between high parametric gain and low distortion, where we were still well within the regime where the spectral phase has not been compromised. The fine structure observed in the temporal and spectral intensity plots is characteristic of the continuum pulse, rather than an artifact of our experiment or the retrieval algorithm. We routinely observe such previously highly structured broadband continuum pulses from microstructure fibers[48]. Numerical simulations and single-shot measurements of such a continuum also show that the spectrum of such a pulse is highly structured due to higher order nonlinear processes involved in the generation of white light[47, 35].

So far, we have validated by numerical modeling the new variation of the FROG technique, called OPA XFROG, which, along with its cousin DFG XFROG, is the most sensitive ultrashort-light-pulse-measurement technique now available. Unlike interferometric methods, it does not carry prohibitively restrictive requirements, such as perfect mode-matching, perfect spatial coherence, highly stable absolute phase, and a same-spectrum reference pulse. We have shown that, while care must be taken to avoid GVM effects in such measurements for fs pulses, this problem can be solved by using appropriate broadband crossed-beam geometries which permits the use of relatively thick crystals and high parametric gains. This makes OPA and DFG

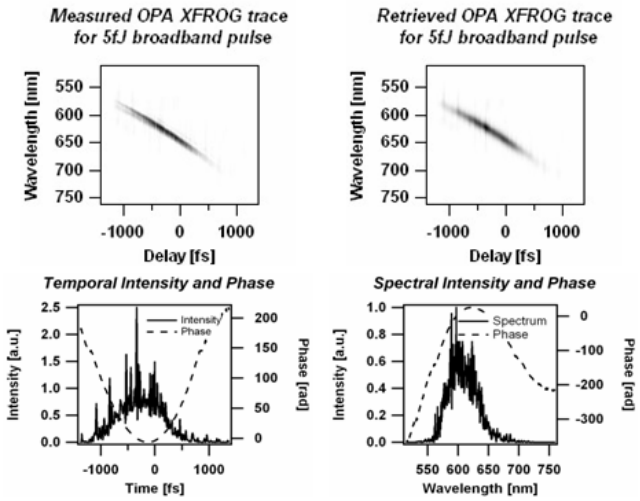

Figure 25: Measured and Retrieved OPA XFROG measurements of broadband white light continuum for a pulse of 5 fJ, showing a gain of ~ 1490.

XFROG powerful tools for measuring non-laser ultrashort light pulses. We previously demonstrated that OPA XFROG can measure the intensity and phase vs. time for pulses with only a few attojoules per pulse and with pulse widths on the order of 250 fs; now we have shown that much broader bandwidth pulses can also be measured accurately. By increasing the pump power (despite the limits imposed by competing OPG processes), it should be possible to measure ultraweak pulses of the order of a few hundred zeptojoules (i.e., just a few photons per pulse). DFG XFROG has the same sensitivity and should be ideal for measuring light pulses in the infrared, although broadband beam geometries remain to be considered for these wavelengths. More importantly, we believe that it should be possible to use OPA XFROG to measure ultraweak, ultrafast fluorescence from biologically important "nonfluorescent" media.

CHAPTER IV

NUMERICAL SIMULATIONS OF GRENOUILLE

This chapter originally appeared in paper:

Xuan Liu, Rick Trebino and Arlee V. Smith, "Numerical simulations of ultrasimple ultrashort laser-pulse measurement", Optics Express 15, 4585-4596(2007)[71].

4.1 Ultrashort-laser-pulse measurement device complexity and its reduction: GRENOUILLE

Measuring ultrashort laser pulses has traditionally been a difficult task. Virtually all available techniques are based on autocorrelation, which requires splitting the pulse into two replicas, combining them in space and time in a nonlinear-optical medium, and measuring the nonlinear-optical signal pulse while varying the delay between the two replicas. Methods that yield more than the mere autocorrelation also require additional optics, such as a spectrometer, and some methods also involve devices as complex as interferometers and pulse shapers or stretchers, as well. Complex devices are inherently difficult to work with and are usually easily misaligned. As a result, complex devices often introduce the very distortions they are designed to measure. While complex computer programs can also be required, this does not add complexity to the device operation, as such programs are available commercially and are now also very fast. And computer programs do not misalign or change with time. Thus, experimental simplicity is the high priority of ultrashort-pulse measurement.

Recently, an extremely simple pulse-measurement device was introduced and is now in wide use. A highly simplified version of the frequency-resolved-optical-gating (FROG)[93] family of devices, this method (called GRENOUILLE[77] ; see figure 26.) operates by using a simple, large-apex-angle prism (a "Fresnel biprism") to split the

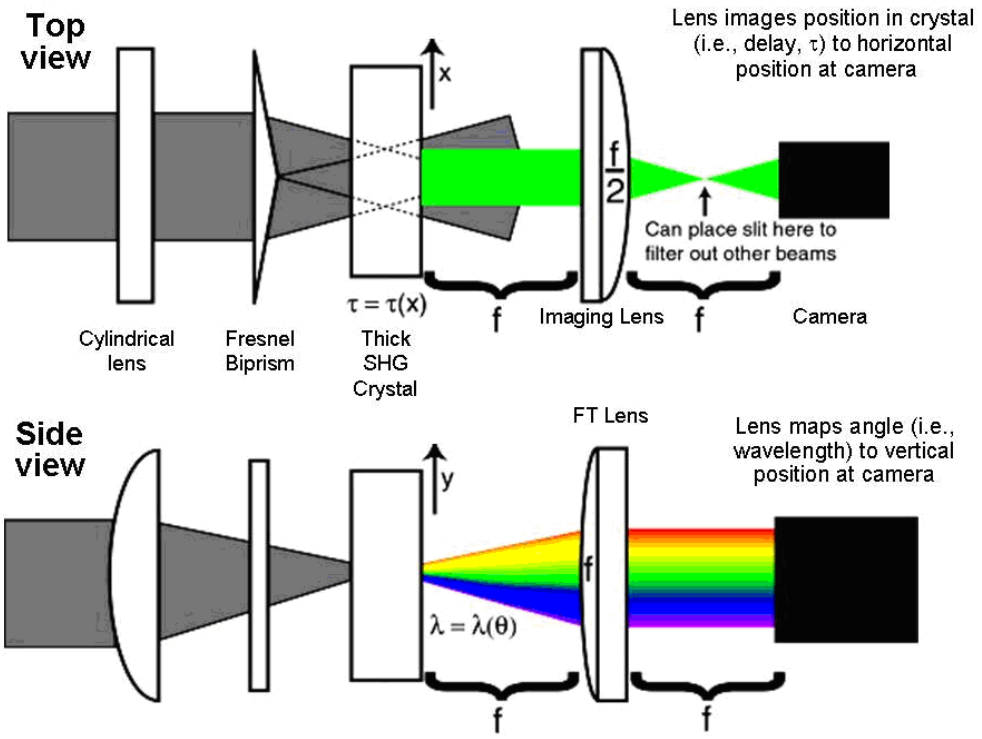

Figure 26: GRENOUILLE from above and the side.

beam into two replicas and to automatically cross and align them in space and time in the crystal. It uses a relatively large crossing angle and a line focus, so the pulse replicas' relative delay is mapped onto the crystal transverse position (see figure 27). GRENOUILLE's second innovation is the use of a thick second-harmonic-generation (SHG) crystal, which, due to its thickness, phase-matches only a small-and different-fraction of the pulse bandwidth for each output angle, allowing the crystal to operate, not only as an autocorrelating element, but also as a spectrometer (see figure 28). The phase-matching bandwidth of the thick crystal is then GRENOUILLE's spectral resolution (and not its spectral range, as in other devices). These two simple innovations yield a very simple, compact FROG device composed of only four easily aligned, linearly arranged optical elements and that requires almost no alignment and never misaligns. In addition, without modification, GRENOUILLE also measures the

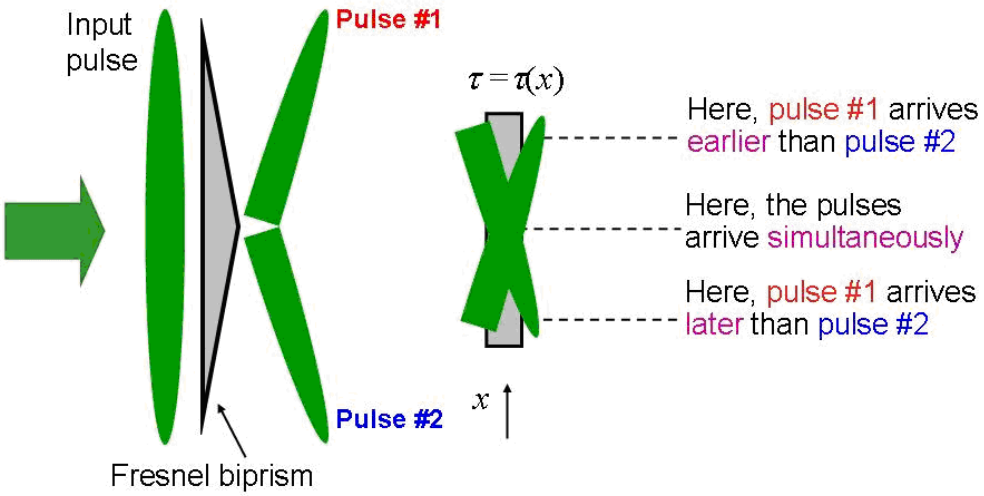

Figure 27: The Fresnel biprism and its use for splitting and crossing two replicas of the pulse to be measured. It maps delay onto transverse position of the crystal.

spatio-temporal distortions, spatial chirp and pulse-front tilt: the otherwise symmetrical trace develops shear in the presence of spatial chirp and displacement along the delay axis in the presence of pulse-front tilt[2, 3, 5].

As with all innovations, the Fresnel biprism and the thick crystal involve some subtlety. For example, the Fresnel biprism should not be used for extremely short or long pulses. For short pulses, it can introduce too much group delay dispersion (GDD) and so must be replaced with a "Fresnel bimirror." For long pulses, a larger crossing angle is required to achieve the large range of delays, and the biprism apex angle becomes too small (i.e., far less than 180), introducing too much angular dispersion in to the beams, and the beam may see very different GDD for different transverse positions. But the Fresnel biprism's physics is relatively simple, and it works well for a wide range of pulse lengths ($\sim$ 20 fs to $\sim$ 1 ps), so we will not consider its effects here. More subtly, the thick crystal must also be used with care. Use of a thicker crystal will yield better spectral resolution due to a smaller phase-matching bandwidth but will also introduce more GDD into the pulse to be measured. Use of a thinner crystal does the converse. Thus the design of a GRENOUILLE is a careful compromise

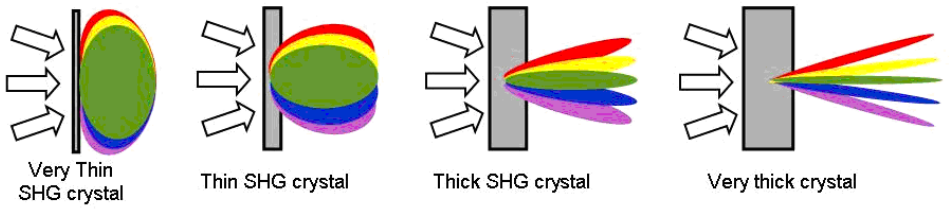

Figure 28: Rough polar plots of the output SHG intensity of a given color vs. angle for a tightly focused broadband input pulse and SHG crystals of various thicknesses. The thick crystal autocorrelates the tightly focused input pulse and simultaneously angularly disperses the resulting second-harmonic pulse.

between opposing complications. Also, the simple picture of figure 28 oversimplifies the potentially complex nonlinear optics somewhat. Not only is SHG occurring in the thick crystal, but a wide range of sum-frequency-generation (SFG) processes-both collinear and noncollinear-are also. It is important to check that the simple picture accurately reflects the device's reality. Next we are going to numerically simulate GRENOUILLE measurements, taking into account these effects involving the thick crystal and the SFG processes.

4.2 Numerical Simulation of GRENOUILLE

When we simulate the second-order nonlinear-optical process in GRENOUILLE, it is convenient for us to work in the space $(\vec{k}, \omega)$ and assume the input beam is aligned along the z-axis, which is perpendicular to the crystal face. Because the input pulse is broadband, these involve a wide range of input frequencies (ω_1 and ω_2) generating the sum frequency $\omega_3 = \omega_1 + \omega_2$ in a given direction. Also, because the beams involved are tightly focused, each of these processes can also occur through off-axis phase-matching processes,$\vec{k}_1 + \vec{k}_2 = \vec{k}_3$, where $\vec{k}_3$ is the phase-matched sum frequency k-vector in a given direction(see figure 29).

Let y be the transverse direction in which the crystal's phase-matching wavelength varies. To simulate the physics of GRENOUILLE, we calculate the spectrum at the

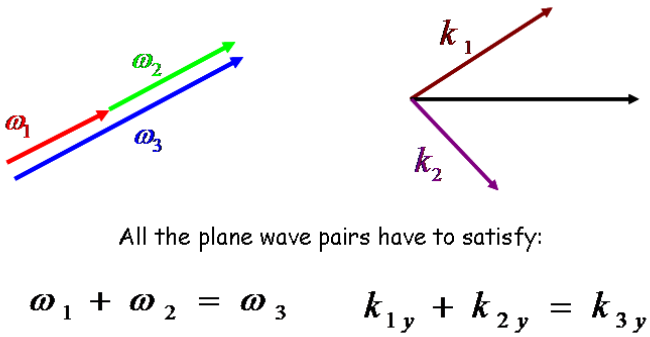

Figure 29: Sum-frequency-generation (SFG) processes in GRENOUILLE: both collinear and noncollinear

crystal exit face for each time delay and output angle in the yz-plane. For the x-dimension (the direction in which the delay between the two beams varies), we simply include a delay between the two pulse replicas. Under the non-depleted-pump assumption, we integrate the wave equation:

$$\frac{\partial E_3(k_{3y},\omega_3,z)}{\partial z} = \int_{-\infty}^{+\infty}\int_{-\infty}^{+\infty} i\frac{d_{eff}\omega_3}{c\tilde{n}_3}\exp(-i\Delta k_z z)\times E_1(k_{1y},\omega_1,z)E_2(k_{3y}-k_{1y},\omega_3-\omega_1,z)dk_{1y}d\omega_1 \tag{65}$$

where E_3 is the sum-frequency field and $E_{1,2}$ correspond to the fundamental input fields.d_{eff} is the effective nonlinearity and $\tilde{n}$ is the effective refractive index. The field envelopes are constructed on a grid of (k_y,ω). The above-mentioned constraints $k_{3y} = k_{1y} + k_{2y}$ and $\omega_3 = \omega_1 + \omega_2$ are strictly enforced. The polarization at the generated sum frequency is calculated for each (k_y,ω) taking into account the contribution from multiple $E_1(k_{1y},\omega)$ and $E_2(k_{2y},\omega)$ pairs that satisfy those conditions. The phase mismatch Δk_z is complicated and becomes a function of both frequency and off-axis angle with respect to z. For a Type I phase-matching process, considering a specific point $q_{(k_{3y},\omega_3)}$ on the grid (see figure 30), if we assume one of the suitable pairs that contributes is $P1_{(k_{1y},\omega_1)}$ and $P2_{(k_{2y},\omega_2)}$ the phase mismatch along z-axis Δk_{qz} for the grid point $q_{(k_{3y},\omega_3)}$ is computed by:

$$\Delta k_{qz} = \frac{\omega_3 n_e(\omega_3,\theta_3)}{c}\cos\theta_3 - \frac{\omega_1 n_o(\omega_1)}{c}\cos\theta_1 - \frac{\omega_2 n_o(\omega_2)}{c}\cos\theta_2 \tag{66}$$

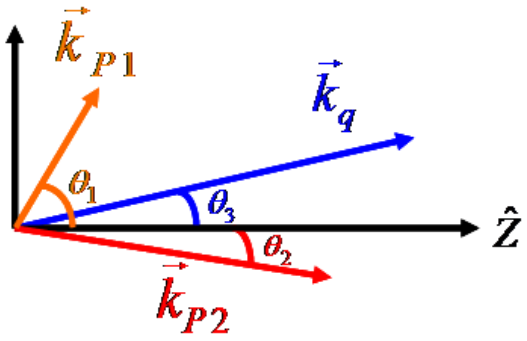

Figure 30: Diagram for the phase-mismatch calculation. The k-vector of grid $q_{(k_{3y},\omega_3)}$ is tilted from the z-axis by θ_3. θ_1 and θ_2 are the tilt angles of the k-vectors of the electric field pair $P1_{(k_{1y},\omega_1)}$ and $P2_{(k_{2y},\omega_2)}$.

The angles θ_1, θ_2 and θ_3 can be easily calculated since they are fixed for each corresponding (k_y, ω) grid point. For the refractive indices, n_e and n_o,we used the full Sellmeier equation, so the crystal dispersion is included to all orders, rather than by an expansion in a power series. Then the radiation field contributed by $P1_{(k_{1y},\omega_1)}$ and $P2_{(k_{2y},\omega_2)}$ is simply $\propto iE_{p1}E_{p2}(\exp(-i\Delta k_{qz}L)-1)/\Delta k_{qz}$, where L is the length of the crystal.

For our simulations, we use various temporal fields to test the device, but, in all cases, we assume a Gaussian-shaped spatial input-field profile. In addition, all the input beams are assumed to have their waists at the center of the crystal. For each delay between the two replicas, we integrate equation (65) to compute the SHG/SFG field.

Figure 31 shows the calculated spectrum for a 800 nm input pulse at the exit face of a 3.5mm BBO crystal *v.s.* the deviation angle(zero degree corresponds to the second harmonic phase matching angle for the center wavelength). As we expected, the thick crystal does work like a spectrometer. Different colors are separated and observed at different angles. Still, the resolution is limited since the length of the crystal is finite. In chapter 5 we will discuss how to improve the spectral resolution

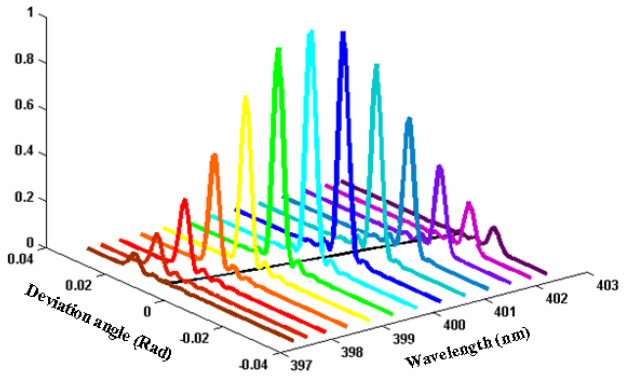

Figure 31: The thick crystal functions as a low resolution spectrometer.

of GRENOUILLE using numerical deconvolution methods.

Because GRENOUILLE involves interpreting a given crystal output angle as the SHG frequency, we must compute the SHG/SFG intensity vs. crystal output angle, integrating over all frequencies. And because the focusing can be tight, we cannot simply interpret the transverse k-vector component, k_y, , as the output angle. In other words, the off-axis k-vector component yields an output angle that also depends on the k-vector magnitude $\sin\theta = k_y/[n_e(\omega,\theta)\omega/c]$.

To calibrate our simulated GRENOUILLE traces, we simulate a double pulse trace GRENOUILLE (FROG) trace, which has both well-known temporal and spectral structure that depends only on the pulse separation, as is done to calibrate GRENOUILLEs in practice[76]. The FROG retrieval algorithm is then applied to the computed GRENOUILLE trace, and the retrieved pulses are compared with the precise known input pulses. We compare our simulated traces with ideal FROG traces, computed using the well-known formula:

$$I_{FROG}(\omega,\tau) = \left| \int_{-\infty}^{\infty} E(t)E(t-\tau)\exp(-i\omega\, t)\, dt \right|^2 . \tag{67}$$

We also run the standard SHG FROG algorithm for our simulated GRENOUILLE

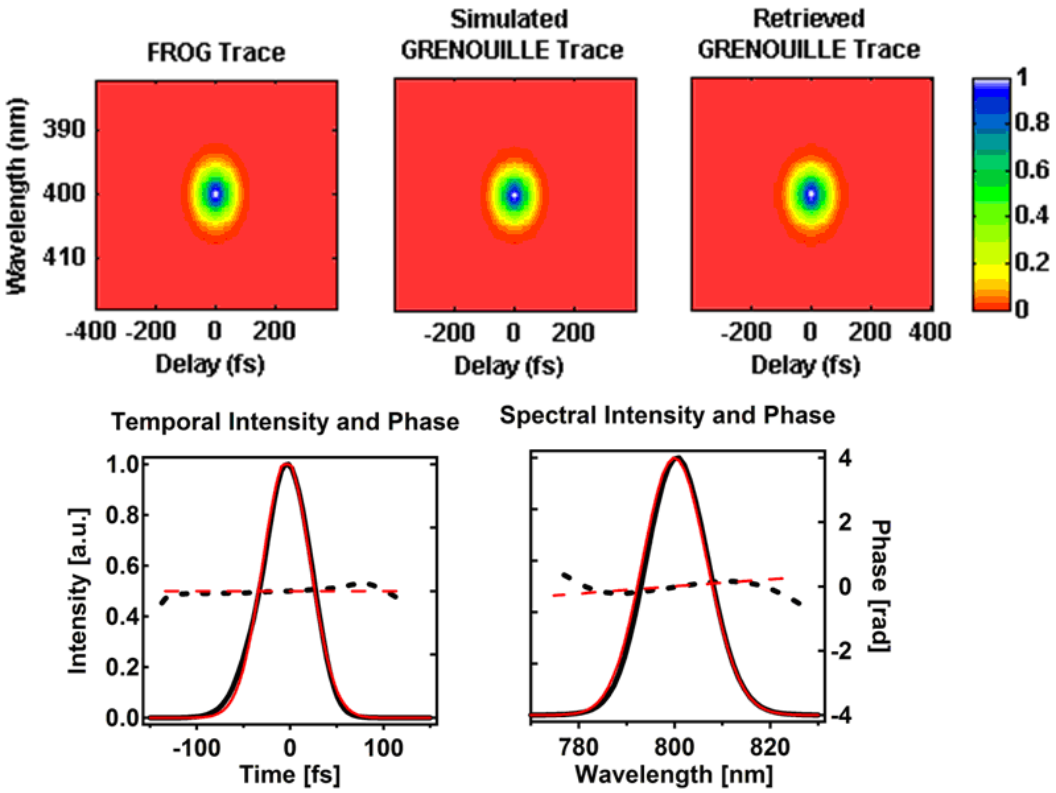

Figure 32: (a) Ideal FROG trace for the 60fs flat phase pulse. (b) Simulated GRENOUILLE trace of a. (c) Retrieved GRENOUILLE trace. (d,e) The black lines show the retrieved temporal and spectral intensities and phases of the pulse. The red lines show the intensities and phases of the actual input pulse.

traces and determine the accuracy with which GRENOUILLE determines both the SHG FROG trace and also, more importantly, the actual pulse. Our grid size for all traces is 128 x 128.

To determine whether GRENOUILLE correctly measures pulses in general, we performed simulations of several test pulses. We present a typical result here in which we simulated the GRENOUILLE trace of a 60-fs, flat-phase Gaussian, 800-nm input pulse (whose ideal FROG trace is shown in figure 32(a)). We use a 3.5 mm BBO SHG crystal, which is commonly used to measure pulses from 50 to about 500 fs in length. The input beam was focused to 10 m in the center of the crystal. The delay increment used was 7.5591 fs, and the wavelength spacing was 0.5138 nm. The resulting GRENOUILLE trace is shown in figure 32(b), and the corresponding

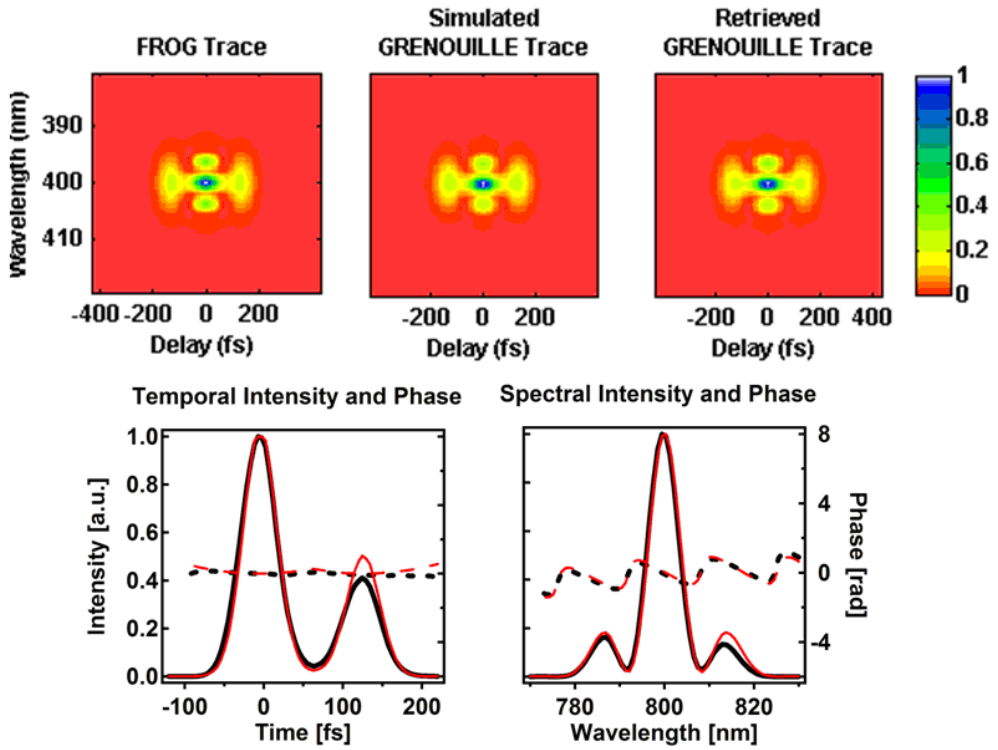

Figure 33: Ideal FROG trace of a double chirped 50 fs pulse. (b) Simulated GRENOUILLE trace. (c) Retrieved GRENOUILLE trace. (d,e) The black curves show the retrieved temporal and spectral intensities and phases of the pulse. The red curves show the intensities and phases of the actual input pulse.

retrieved trace is shown in 32(c). The retrieved temporal and spectral intensities and phases show excellent agreement with the actual pulse temporal and spectral intensities and phases in 32(d) and 32(e).

We find excellent agreement among the ideal, simulated, and retrieved traces. The rms error between the simulated GENOUILLE trace and the FROG trace was 0.007051. The rms error between the retrieved GRENOUILLE trace and the FROG trace was 0.006105. The rms error between the simulated and retrieved GRENOUILLE traces was 0.003534. In other words, the simulated and retrieved traces are quite accurate. Also, note that the rms error between the retrieved trace and the ideal FROG trace is less than that between the simulated trace and the ideal FROG trace. This

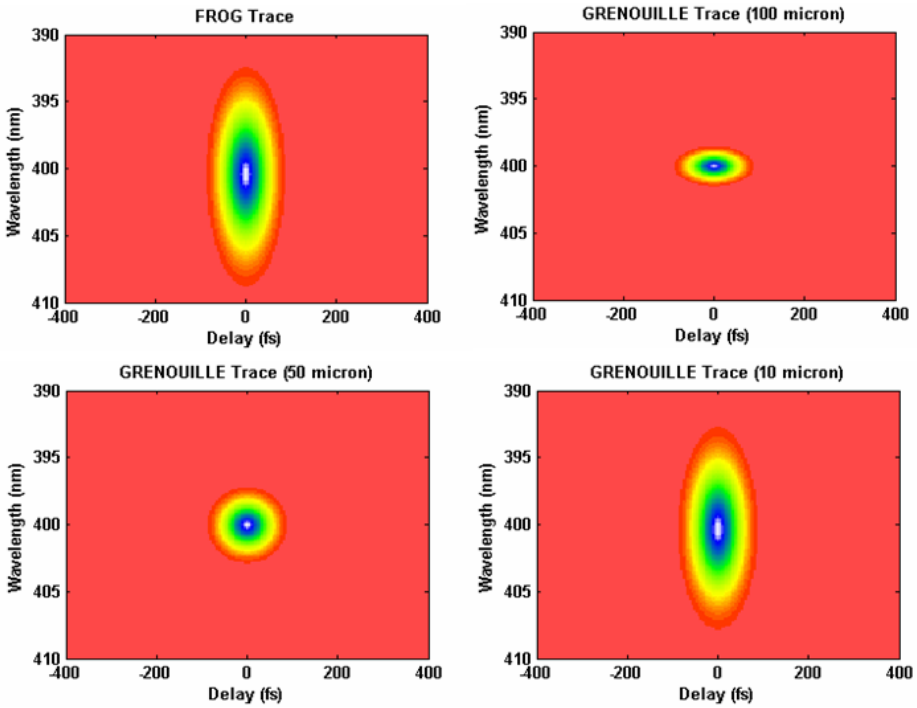

Figure 34: (a) Ideal FROG trace of the 60fs flat phase pulse. (b) Simulated GRENOUILLE trace of the same pulse using 100 μm focus. (c) Simulated GRENOUILLE trace of the same pulse using 50 μm focus. (d) Simulated GRENOUILLE trace of the same pulse using 10 μm focus.

is because the FROG algorithm is able to correct for slight discrepancies in the simulated (measured) trace due to the redundancy in the time-frequency-domain trace. We find that this occurs in all of our simulations and is a convenient feature of FROG (an effect we observe experimentally as well).

We also tested GRENOUILLE's ability to measure complex pulses, and we present one such example here. Figure 33 shows the ideal FROG trace, the simulated GRENOUILLE trace, and the retrieved trace for two overlapping chirped 50-fs pulses with identical parabolic phases (a "double chirped" pulse) using a 3.5 mm BBO crystal and 10 m focal spot. The delay spacing was 9.4488 fs and wavelength spacing was 0.2509 nm. The rms error between the simulated GENOUILLE trace and the FROG trace was 0.006429. The rms error between the retrieved GRENOUILLE trace and

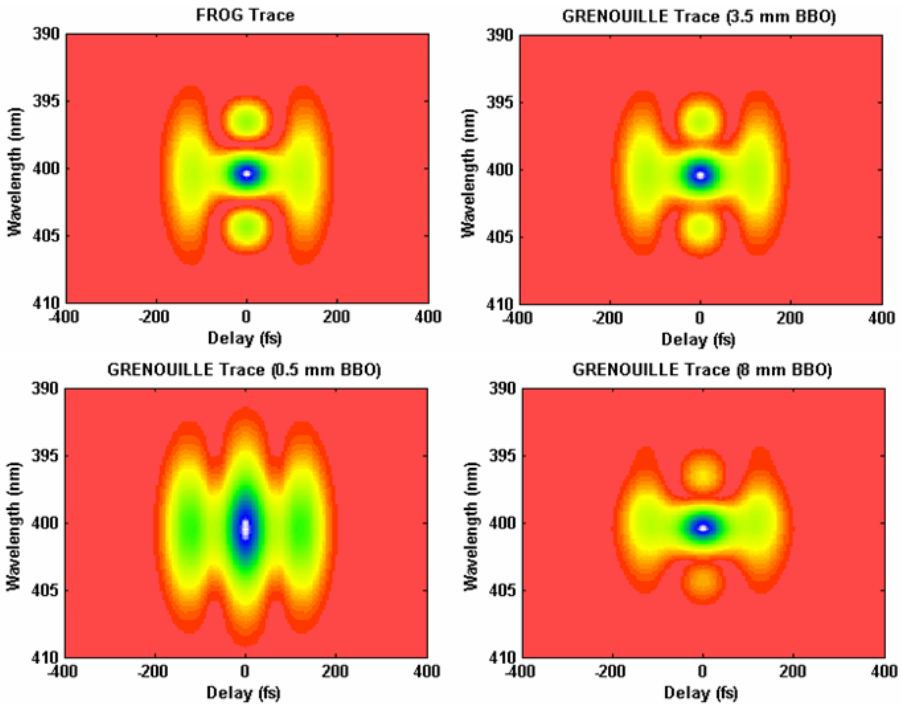

Figure 35: (a) Ideal FROG trace of the 50fs double chirped pulse. (b) Simulated GRENOUILLE trace of the same pulse using 3.5 mm BBO. (c) Simulated GRENOUILLE trace of the same pulse using 0.5 mm BBO. (d) Simulated GRENOUILLE trace of the same pulse using 8 mm BBO focus.

the FROG trace was 0.006191. The rms error between the simulated and retrieved GRENOUILLE trace was 0.003383. We find that the simulated trace yields an intensity and spectrum that do not perfectly match the actual pulse, likely due to the finite beam divergence at the crystal, which yields a slight cropping of the spectrum, but they are not far off.

4.3 Focusing issues and crystal thickness

In GRENOUILLE, the thick crystal functions as the spectrometer dispersive element. Phase-matching maps SHG wavelength to output angle. This means that, in order to measure pulses with large bandwidths, the beam must have a large angular divergence, so a tight focus is required. A beam with too large a spot size and hence too little

divergence will cause frequencies at the edges of the spectrum to be too weak in the resulting GRENOUILLE trace. In the above simulation for the 60-fs pulse, if we were to use a larger focal spot with a correspondingly smaller angular divergence instead, an (erroneous) narrower spectrum would be obtained. And we see precisely this in our simulations, as shown in the figure 34.

Using a thicker crystal decreases the phase-matching bandwidth and so increases the GRENOUILLE spectral resolution. But the crystal should also not be too thick, or the pulse will spread in time due to the crystal GDD, and the pulse temporal structure will be lost. We simulate this effect by varying the crystal thickness and watching the simulated GRENOUILLE trace vary (see figure 35). We use the same pulse as in figure 33. Using a 0.5 mm BBO, the spectral fringes are almost completely lost. The temporal structure of the pulse becomes difficult to recognize for a 8mm thick crystal.

4.4 Measurement of long and short pulses

The GRENOUILLE with the above mentioned configuration usually measures pulses $\sim$ 50 to $\sim$ 500 fs long. However, we find that measurements of pulses longer than 500 fs are also possible with very good accuracy. Figure 36 shows a case of a double chirped long pulse with structure in both delay and frequency and with pulse length of $\sim$550 fs. A 3.5-mm BBO crystal was used with a 10-μm focal spot. The delay increment was 32.126 fs and the wavelength increment was 0.1589 nm. Interestingly, GRENOUILLE measures this pulse quite well. The rms error between the simulated GENOUILLE trace and the FROG trace was 0.021896, quite good for a pulse this complex. The rms error between the retrieved GRENOUILLE trace and the FROG trace was 0.015758. The ms error between the simulated and retrieved GRENOUILLE trace was 0.013183. Again, it appears that the well-known fundamental redundancy in the time-frequency-domain trace and the robust FROG phase-retrieval algorithm

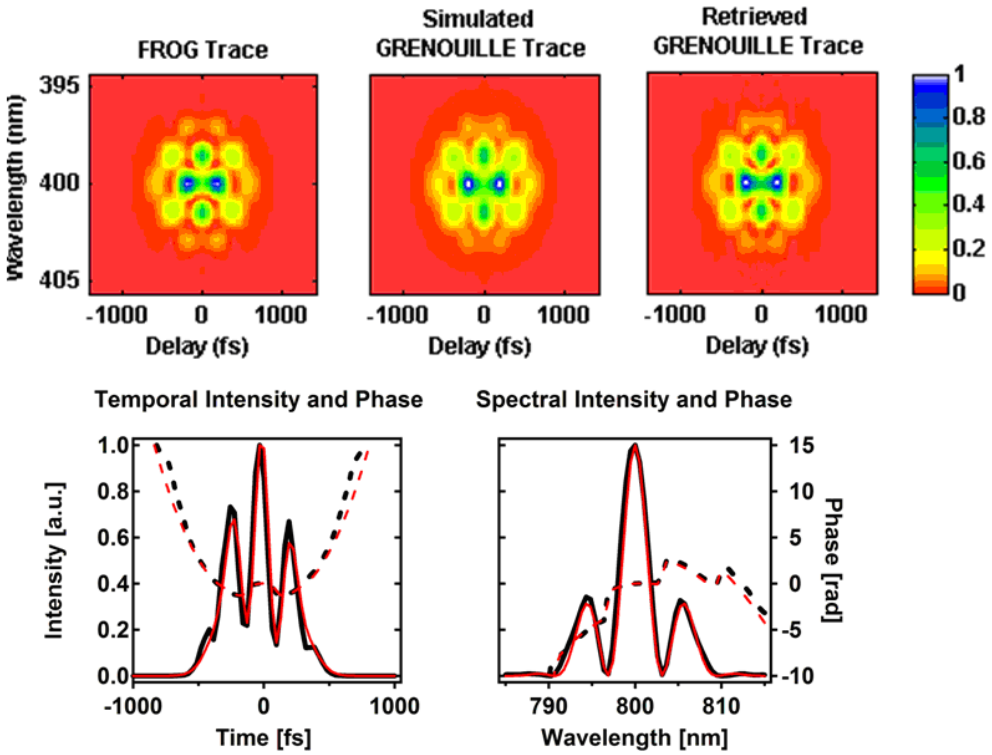

Figure 36: (a) Ideal FROG trace of a double chirped long pulse. (b) Simulated GRENOUILLE trace of the same pulse. (c) Retrieved GRENOUILLE trace. (d,e) The black curves show the retrieved temporal and spectral intensities and phases of the pulse. The red curves show the intensities and phases of the actual input pulse. The FROG (rms) error was 0.013183.

are able to compensate for the insufficient spectral resolution in the GRENOUILLE trace.

The shortest pulses ever measured by GRENOUILLE are ∼20 fs long [6]. The thickness of the BBO crystal in such measurements was 1.5 mm. A tighter focus ensured the larger divergence angle required to cover the larger spectrum. The following simulation demonstrates GRENOUILLE's ability to measure pulses as short as 20 fs, which also have with fine structure (See figure 37). We used a 5-μm focal-spot diameter. The delay increment used was 3.7795 fs and the wavelength spacing used was 1.4509 nm. The rms error between the simulated GENOUILLE trace and the FROG trace was 0.010379. The rms error between the retrieved GRENOUILLE trace and the FROG trace was 0.006799. The ms error between the simulated and retrieved GRENOUILLE trace was 0.008367. The intensities and phases versus time and frequency retrieve quite well. Pulse distortion due to material dispersion is negligible. The minor discrepancy is due to slightly insufficient resolution of the thick crystal 'spectrometer.'

This specific GRENOUILLE design has a resolution of 4 nm at 800 nm, somewhat less than that required to resolve this relatively long pulse. Again, the FROG retrieval algorithm improves the trace, this time significantly (a factor of two improvement in the rms error), retrieving the spectral side lobes reasonably well. For even shorter pulses, temporal broadening due to dispersion will be a problem (For BBO, 800nm type I phase matching, the $GVM = 1.92 \times 10^3$ fs/cm. The $GDD = 195.9 fs^2/mm$ at 400nm). However, a thinner crystal could be used in this case.

In conclusion, we have numerically simulated the performance of GRENOUILLE, which involves considering the complex sum-frequency generation of tightly focused, broadband input beams in a thick SHG crystal. We take into account dispersion using the full Sellmeier equation. We have shown that using an appropriate crystal thickness and beam focus assures the accuracy of a GRENOUILLE measurement.

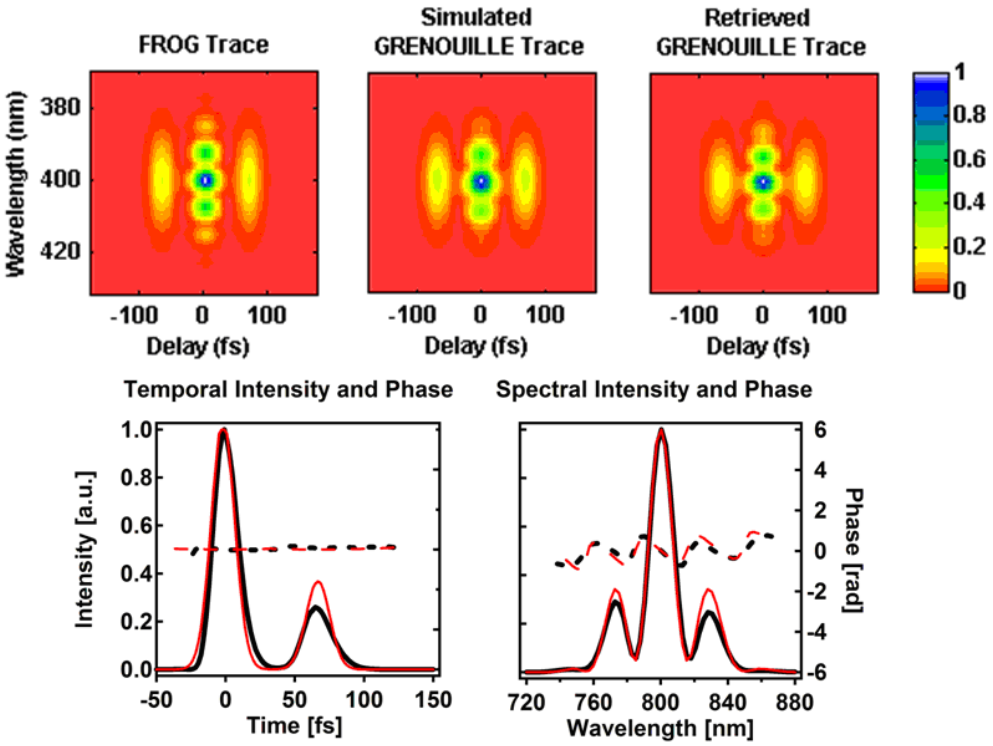

Figure 37: (a) Ideal FROG trace of a slightly chirped 20 fs double pulse. (b) Simulated GRENOUILLE trace of this pulse. (c) Retrieved GRENOUILLE trace. (d,e) The black curves show the retrieved temporal and spectral intensities and phases of the pulse. The red curves show the intensities and phases of the actual input pulse. The FROG (rms) error was 0.008367.

Specifically, our simulations show that GRENOUILLE is able to accurately measure pulses over at least an order of magnitude range of pulse lengths, spectral widths, and temporal and spectral structure. Despite its experimental simplicity, it is even capable of measuring complex pulses with time-bandwidth products approaching 10. Only more complex, complete versions of FROG (and its cousin XFROG) can do better. Such performance, which matches that of GRENOUILLEs observed experimentally, is more than adequate for monitoring the output of today's ultrafast lasers and even measuring some shaped pulses.

CHAPTER V

SPECTRAL DECONVOLUTION OF GRENOUILLE

5.1 GRENOUILLE response function

The GRENOUILLE's spectral resolution is limited by the phase-matching bandwidth of the thick crystal. Better spectral resolution can be achieved by use of a thicker crystal. However, it also introduces more GDD into the pulse to be measured. The spectral resolution is 2nm at 800 nm for a GRENOUILLE which uses a 3.5 mm BBO. In order to improve its spectral resolution without introducing any complexity to the device, we could post-process the GRENOUILLE trace by use of numerical deconvolution method, which is a commonly used procedure in image processing or spectral measurements[12, 55, 54]. We used the simulated GRENOUILLE trace and its correspondent FROG trace to characterize the response function of the device. We then pseudoinverse filtering, or approximate deconvolution the GRENOUILLE trace with this blurring function. In this chapter, we will show that deconvolution procedure greatly enhances the heavily blurred GRENOUILLE traces and improves its spectral resolution.

Using SHG picture to describe the nonlinear optics process inside GRENOUILLE is over simplified. GRENOUILLE involves tight focusing of broadband pulses into a thick crystal, not only SHG is occurring, but also a wide range of sum-frequency-generation (SFG) processes-both collinear and noncollinear. From the previous chapter, we know that the SFG processes in GRENOUILLE can be calculated using the following wave equation,

$$\frac{\partial E_3(k_{3y},\omega_3,z)}{\partial z} = \int_{-\infty}^{+\infty}\int_{-\infty}^{+\infty} i\frac{d_{eff}\omega_3}{c\tilde{n}_3}\exp(-i\Delta k_z z)\times E_1(k_{1y},\omega_1,z)E_2(k_{3y}-k_{1y},\omega_3-\omega_1,z)dk_{1y}d\omega_1 \tag{68}$$

Before we use numerical method to find the response function of GRENOUILLE, we can show that the response function has a shape close to a sin^2. We assume the pump is not depleted and the fundamental beams do not vary with respect to z, so we can integrate over z:

$$E_3(k_{3y},\omega_3,L)=\int_{-\infty}^{+\infty}\int_{-\infty}^{+\infty} i\frac{d_{eff}\omega_3}{c\tilde{n}_3}L\exp(-i\Delta k_z L/2)\sin c(\Delta k_z L/2)\times E_1(k_{1y},\omega_1)E_2(k_{3y}-k_{1y},\omega_3-\omega_1)dk_{1y}d\omega_1 \tag{69}$$

Neglecting uninteresting proportionality constants, and assuming that the beam has a very large divergence, so the k-dependence of the electric fields can be neglected, yields:

$$E_3(k_{3y},\omega_3,L)\propto\int \sin c(\Delta k_z L/2)\ E_1(\omega_1)\ E_2(\omega_3-\omega_1)\ d\omega_1 \tag{70}$$

we can approximate all the SFG processes as the simple second-harmonic process, which is emitted in approximately the usual second-harmonic direction. So to first order, the phase-mismatch will depend only on the second-harmonic frequency, ω_3, and the angle(k_{3y}) and not ω_1 or ω_2. So expand to first order the phase-mismatch, ΔK, in the variable ω_3 about the phase-matched frequency in the direction,(k_{3y}), which we'll denote by: $\omega_{30}(k_{3y})$

$$\Delta k_z\approx\beta[\omega_3-\omega_{30}(k_{3y})] \tag{71}$$

So we now have:

$$E_3(k_{3y},\omega_3,L)\propto\int \sin c[\beta(\omega_3-\omega_{30}(k_{3y}))L/2]\ E_1(\omega_1)\ E_2(\omega_3-\omega_1)\ d\omega_1 \tag{72}$$

Now note that we can factor the *sinc* function out of the integral because it's independent of ω_1,

$$E_3(k_{3y},\omega_3,L)\propto \sin c[\beta(\omega_3-\omega_{30}(k_{3y}))L/2]\ \int E_1(\omega_1)\ E_2(\omega_3-\omega_1)\ d\omega_1 \tag{73}$$

Now the integral is just the ideal second-harmonic spectral field,$E_3(\omega_3)$,

$$E_3(k_{3y},\omega_3,L)\propto \sin c[\beta(\omega_3-\omega_{30}(k_{3y}))L/2]\ \ E_3(\omega_3) \tag{74}$$

This expression tells us that the second-harmonic spectral field in any direction, k_{3y}, is just the actual spectral field times a *sinc* filter function. The spectrum in the k_{3y} direction is then the mag square of this result:

$$S_3(k_{3y}, \omega_3, L) \propto \sin c^2[\beta(\omega_3 - \omega_{30}(k_{3y}))L/2] \;\; S_3(\omega_3) \tag{75}$$

where S_3 is the SH spectrum after the crystal in the direction, k_{3y}. Thus, the spectrum in a given direction is a chunk of the pulse spectrum determined by the phase-matching *sinc*-function. The total pulse energy in the k_{3y} direction, $U_3(k_{3y})$, is what GRENOUILLE measures. It is the integral of the spectrum over all frequencies, ω_3:

$$\begin{aligned} U_3(k_{3y}, L) &\propto \int S_3(k_{3y}, \omega_3, L)\; d\omega_3 \\ &\propto \int \sin c^2[\beta(\omega_3 - \omega_{30}(k_{3y}))L/2]\; S_3(\omega_3)\; d\omega_3 \end{aligned} \tag{76}$$

which is a cross-correlation between the SH spectrum $S_3(\omega_3)$ and the $sinc^2$ function. This result can be written as a convolution because $sinc^2$ is symmetric:

$$U_3(k_{3y}, L) \;\propto \int \sin c^2[\beta(\omega_{30}(k_{3y}) - \omega_3)L/2]\; S_3(\omega_3)\; d\omega_3 \tag{77}$$

It turns out we need to deal with a deconvolution problem in order to improve the spectral resolution of GRENOUILLE. In the next section, we will give a brief introduction to the image restoration theory. We start with a formalization of the problem and explain how linear model works using the well-known Wiener filter as an example. Then we will introduce the idea of deconvolution using statistical modeling and especially emphasis on the Richardson-Lucy method, which we will use for our problems. Other deconvolution technique, such as the wavelet-based methods will not be covered here.

5.2 Deconvolution and Richardson-Lucy algorithm

Image reconstruction has been a very important research field in modern astronomy and electrical engineering. Signal collected by real devices are always distorted to

some extent. In optical imaging, people use point spread function (PSF) to describe the response of an imaging system to a point source.

Assuming the imaging system used is ideal, a perfect image has the intensity of $o(x)$ will be formed. However, if the system is not perfect but has a point spread function of h, we will end up with a blurred image $o_{blur}(x)$ which can be written as,

$$o_{blur}(x) = \int o(x')h(x, x')dx' \tag{78}$$

If the signals are digitized, we have

$$o_{blur}(x) = \sum_{x'} o(x')h(x, x') \tag{79}$$

which means, each point x' will contribute to the intensity of point x with a probability of $h(x, x')$. Most of the time, a deblurring filter $\hat{h}(x, x')$ is estimated such that the error between the deconvolved image $\hat{o}(x)$ and the true image $o(x)$ is minimized. If the point spread function is spacially invariant, we have $o(x, x') = o(x - x')$. Equations 78 and 79 are just continuous and discrete convolution by defination. From Fourier transform convolution theorem, we know the Fourier transform of a convolution is the product of the Fourier transforms of the functions to be convolved: $\mathbf{F}(o_{blur}(x)) = \mathbf{F}(o \otimes h) = \mathbf{F}(o)\mathbf{F}(h) = O \times H$(here we use capitalized letters to represent the Fourier transformed forms of functions). We then have an exact inverse filter estimator $F(\hat{q}(x, x')) = 1/H$. This is also called the 'direct inversion' method. In practise, it rarely works because at certain points, $H(k)$ can be zero or close to zero, which just yields noise amplification. One solution is to set a cutoff frequency, which results in the so called pseudo-inverse filter:

$$\hat{Q}(k) = \begin{cases} \frac{1}{H(k)} & |H(k)| > \delta \\ 0 & |H(k)| \leq \delta \end{cases} \tag{80}$$

The above model does not include noise. A more realistic and useful model is shown in figure 38, which includes an additive noise, $n(s, t)$. The Fourier transformed blurred

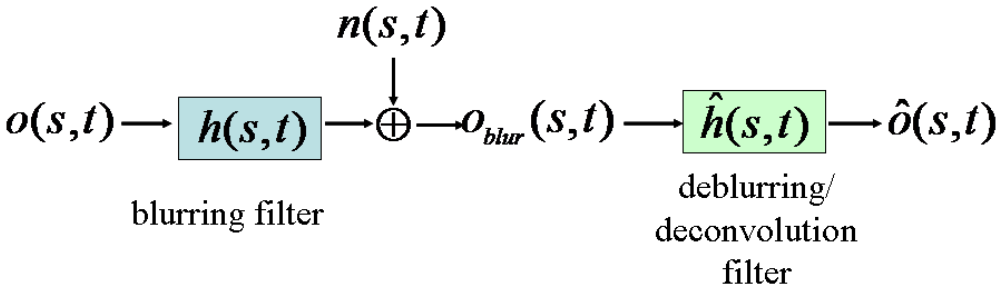

Figure 38: A more realistic model.

image can be written as $O_{blur}(u,v) = \mathbf{F}[o_{blur}(s,t)] = \mathbf{F}[o(s,t)] \times \mathbf{F}[h(s,t)] + \mathbf{F}[n(s,t)] = O(u,v)H(u,v) + N(u,v)$.

Over the years, various filters have been developed to reconstruct the true image. Wiener filter[99] is one of the widely used filters. It is a linear filter and has the form,

$$\hat{O}^{Wiener}(u,v) = O_{blur}(u,v)\hat{Q}^{Wiener}(u,v). \tag{81}$$

with the constraint that the expected value of the quadratic error between the estimated image and the true image is as small as possible. It also assumes that the signal and noise are uncorrelated and the noise is not biased.

$$\varepsilon = E\{\sum [\hat{o}^{Wiener}(s,t) - o(s,t)]^2\} \tag{82}$$

Using Parseval's theorem,

$$\varepsilon = E\{\sum \left|\hat{O}^{Wiener}(u,v) - O(u,v)\right|^2\} = E\{\sum \left|O_{blur}(u,v)\hat{Q}^{Wiener}(u,v) - O(u,v)\right|^2\} \tag{83}$$

The minimum corresponds to a zero partial derivative:

$$\frac{\partial \varepsilon}{\partial \mathrm{Re}\{\hat{Q}^{Wiener}(u,v)\}} = 0, \quad \frac{\partial \varepsilon}{\partial \mathrm{Im}\{\hat{Q}^{Wiener}(u,v)\}} = 0 \tag{84}$$

Which is equivalent to

$$\begin{aligned}
&E\{[O_{blur}(u,v)\hat{Q}^{Wiener}(u,v) - O(u,v)]O_{blur}(u,v)^*\} \\
&= E\{\hat{Q}^{Wiener}(u,v)\,|O_{blur}(u,v)|^2 - O(u,v)O_{blur}(u,v)^*\} \\
&= [\hat{Q}^{Wiener}(u,v)\,|H(u,v)|^2 - H(u,v)^*]E\{|O(u,v)|^2\} \\
&+\hat{Q}^{Wiener}(u,v)E\{|N(u,v)|^2\}
\end{aligned} \tag{85}$$

We have derived the Wiener filter,

$$\hat{Q}^{Wiener}(u,v) = \frac{H(u,v)^*}{|H(u,v)|^2 + \frac{E\{|N(u,v)|\}^2}{E\{|O(u,v)|\}^2}} \tag{86}$$

Usually, the information about the true image and noise is not available. we have to estimate them from the available data. It is possible, Wiener filter yields unphysical solutions with negative values and ripples around sharp features.It also somewhat smoothes out the noise.

Approaches based on statistical estimations-Bayesian method are also developed. According to Bayes' theorem, we have

$$p(o|o_{blur}) = \frac{p(o_{blur}|o)p(o)}{p(o_{blur})} \tag{87}$$

where $p(o_{blur})$ is the *prior*/marginal probability distribution of the blurred image. $p(o)$ represents the *prior* probability of the true image over all possible realizations. A Bayes solution is found by maximizing the right part of equation 87. The maximum likelihood methods maximizes the probability density $p(o_{blur}|o)$ over o:

$$o^{ML} = \arg\max_{o} p(o_{blur}|o) \tag{88}$$

Assuming Gaussian noise, the probability $p(o_{blur}|o)$ is

$$p(o_{blur}|o) = \frac{1}{\sqrt{2\pi}\sigma_N}\exp[-\frac{(o_{blur} - h \otimes o)^2}{2\sigma_N^2}] \tag{89}$$

σ_N is the standard deviation of the noise factor. Assuming $p(o)$ is a constant, maximizing equation 88 is equivalent to minimizing equation 90 (log-likelihood estimator

is used here)

$$\begin{aligned} o^{ML} &= \arg\min_{o}\{-\log[p(o_{blur}|o)]\} \\ &= \arg\min_{o} \tfrac{1}{2} \left\|\tilde{h}\tilde{o} - \tilde{o}_{blur}\right\|^{T} \mathrm{cov}(\tilde{o}_{blur})^{-1} \left\|\tilde{h}\tilde{o} - \tilde{o}_{blur}\right\| \end{aligned} \tag{90}$$

We used the matrix form. $\tilde{h}$ is the PSF matrix. $\tilde{o}_{blur}$ represents the blurred image matrix and $\tilde{o}$ is the true image matrix. *cov* represents the covariance. Define the penalty function:

$$\phi_{Gauss} = \frac{1}{2} \left\|\tilde{h}\tilde{o} - \tilde{o}_{blur}\right\|^{T} \mathrm{cov}(\tilde{o}_{blur})^{-1} \left\|\tilde{h}\tilde{o} - \tilde{o}_{blur}\right\| \tag{91}$$

The gradient of ϕ_{Gauss} is:

$$\nabla\phi_{gauss}(\tilde{o}) = \tilde{h}^{T}\mathrm{cov}(\tilde{o}_{blur})^{-1}(\tilde{h}\tilde{o} - \tilde{o}_{blur}) \tag{92}$$

The solution is

$$\tilde{o}^{ML} = [\tilde{h}^{T}\mathrm{cov}(\tilde{o}_{blur})^{-1}\tilde{h}]^{-1}\tilde{h}^{T}\mathrm{cov}(\tilde{o}_{blur})^{-1}\tilde{o}_{blur} \tag{93}$$

It is the solution of a linear least squares problem. For gaussian white noise, we have $cov(\tilde{o}_{blur}) = diag(\sigma^2)$ and $cov(\tilde{o}_{blur})^{-1} = diag(1/\sigma^2)$. Equation 93 reduces to,

$$\tilde{o}^{ML} = [\tilde{h}^{T}\tilde{h}]^{-1}\tilde{h}^{T}\tilde{o}_{blur} \tag{94}$$

After discrete Fourier transform, it is

$$O^{ML} = \frac{H^{*}O_{blur}}{|H|^{2}} = \frac{O_{blur}}{H} \tag{95}$$

This is exactly the result we have at the beginning. Bad news! Additional constraints has to be considered, such as requirement for positive solutions. Due to the additional constraints, the solution can no longer be written in an explicit form. Iterative algorithm, has to be used to minimize equation 90. The constrained Landweber interation[65] has the form:

$$o^{(n+1)} = \vec{P}_{c}[o^{(n)} + \alpha(o_{blur} - o^{(n)} \otimes h)] \tag{96}$$

where $o^{(n)}$ is the current estimation of the desired 'true image' and $\vec{p}_c$ is the projection operator that enforces the set of constraints on $o^{(n)}$. α is the minimization scalar. Another commonly used method is the Image Space Reconstruction Algorithm(ISRA)[22], which is written as

$$o_k^{(n+1)} = o_k^{(n)} \frac{(\tilde{h}^T \mathrm{cov}(\tilde{o}_{blur})^{-1} \tilde{o}_{blur})_k}{(\tilde{h}^T \mathrm{cov}(\tilde{o}_{blur})^{-1} \tilde{h} o^{(n)})_k} \tag{97}$$

We have discussed maximum likelihood method with Gaussian noise, now we are going to introduce the Richardson-Lucy algorithm (RLA)[72, 83, 30] which is based on the maximum likelihood method with Poisson noise assumption. The penalty function is,

$$\phi_{Poisson}(o) = \sum_k \{(\tilde{h} \cdot o)_k + (o_{blur})_k [\log \frac{(o_{blur})_k}{(\tilde{h} \cdot o)_k} - 1]\} \tag{98}$$

We have the following iteration scheme, the so called Richardson-Lucy algorithm,

$$o_k^{(n+1)} = (\tilde{h}^T \cdot \frac{o_{blur}}{\tilde{h} \cdot o^{(n)}})_k o_k^{(n)} \tag{99}$$

Given the blurred image, the PSF h, the following is a pseudo code of the Richardson-Lucy algorithm((n)represent the n-th interation):

RLA$(o_{blur}, h(s,t), o^{(0)}$,n);	start with an initial guess $o^{(0)}$
$H(u,v) = FFT[h(s,t)]$;	Fast Fourier transform of the PSF
for k=1,...n-1	
$o_{blur}^{(k)}$=IFFT($H\times$ FFT$[o^{(k)}]$;	calculate the quantity $\tilde{h} \cdot o^{(k)}$
$o^{(n+1)}$=$o^{(n)}\times$ IFFT$[H^* \times$FFT$(o_{blur}/o_{blur}^{(k)})]$;	new estimation
return $x^{(n)}$	

The number of iterations plays an important role in the iterative methods. Itself is considered as a regularization parameter. When the number of the iteration increases, the retrieved image first approaches the true image and then potentially goes away from it. And it is difficult to find a clear stopping criterion. The advantages are: they are easy to implement and the early iterations are very efficient.

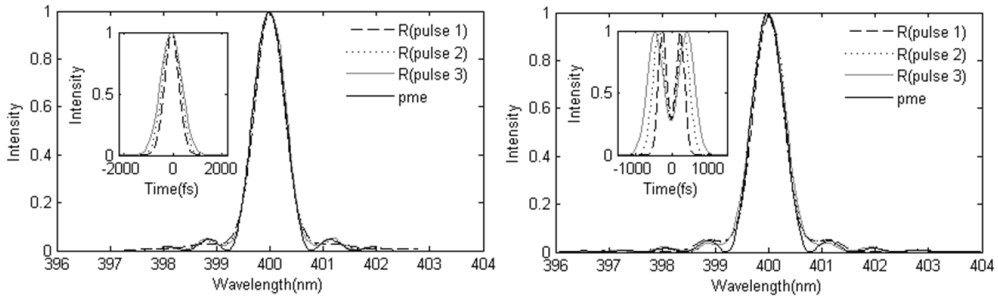

Figure 39: Response functions $R(\omega_3)$ using different single/double pulses. 'pme' refers to the phase matching efficiency $sinc^2$ curve.

5.3 Numerical deconvolution of GRENOUILLE traces

We used the MATLAB built in iterative deconvolution procedure, Richardson-Lucy algorithm to determine the response function from the simulated GRENOUILLE trace and its correspondent ideal FROG trace. Our grid size for all traces was 128 x 128. We assumed Gaussian spatial and temporal profiles. The input beam was focused to 10 μm in the center of the crystal. We use a 3.5 mm BBO SHG crystal, which is commonly used to measure pulses from 50 to about 500 fs in length. We first used the zero delay spectrum $I^{SFG}_{meas}(\omega_3, 0, L)$ and $I^{SHG}_{FROG}(\omega_3, 0)$ to determine the response function $R(\omega_3)$. We tried flat phase single pulses with different pulse length ranging from 500 fs to 700 fs. We also used different flat phase double pulses with different pulse lengths and separations. We found the response functions(see figure 39) are very similar and closely resembles a $sinc^2$ function shape. We also tried spectrum at differently delays, we observe similar results. The FWHM of the response function $R(\omega_3)$ is approximately 0.70 ± 0.03 nm.

Figure 40 shows the simulated GRENOUILLE trace for a complex pulse consisting of a double pulse, each of which is chirped (a "double-chirped pulse") and has a FWHM of 300 fs. The separation between these two pulses is 720 fs. Its FROG trace is shown in figure 40(a) and its GRENOUILLE trace is shown in 40(b). The fine spectral structures with sub 1nm are blurred and unobservable. We only see three

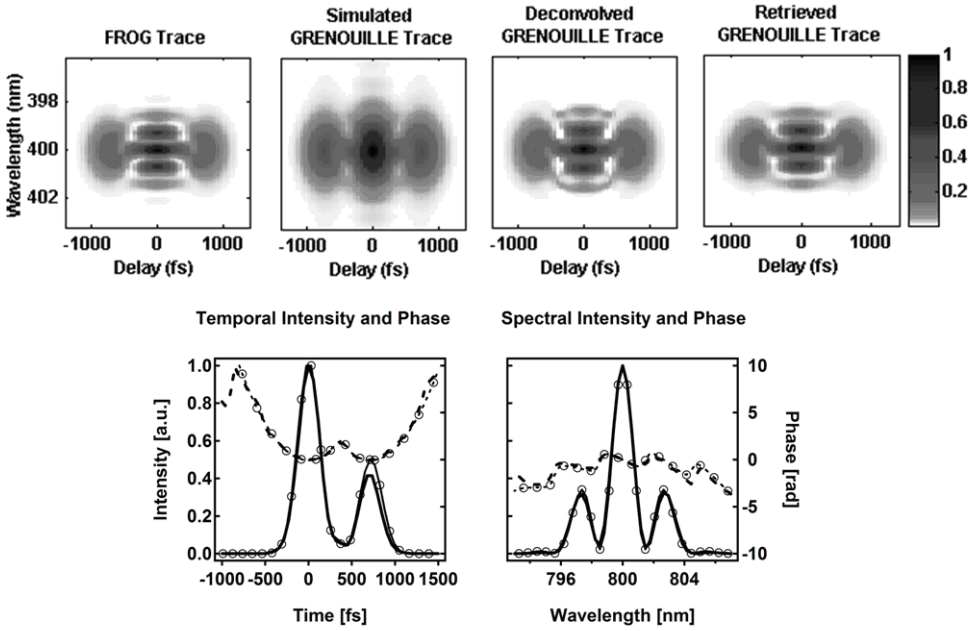

Figure 40: Measuring a pulse with a large temporal separation and spectrally deconvolving the trace to obtain the correct result.

big lobes. Since the temporal structure is still recognizable, it tells us we should have some fringes inside those lobes. The rms error between the FROG trace and the GRENOUILLE trace was 0.047173. If we apply the FROG algorithm to retrieve the blurred GRENOUILLE trace, after two thousand iterations, the algorithm still could not recover any trace that resembles its correspondent FROG trace. The 'missing' spectral fringes and the obvious temporal structure confuses the algorithm. We need to deconvolve the simulated GRENOUILLE trace with its response function. The resulted deconvolved trace is shown in 40(c). Using Lucy-Richardson algorithm, forty iterations were used. Compared with the FROG trace, we notice that all of the major fringes are revealed. The rms error between the FROG trace and the deconvoluted GRENOUILLE trace was 0.012091. Now, we apply our FROG algorithm to it and the retrieval algorithm converges faster, the corresponding retrieved trace is shown in 40(d). The rms error between the FROG trace and the retrieved GRENOUILLE trace was 0.007978. The retrieved temporal and spectral intensities and phases show

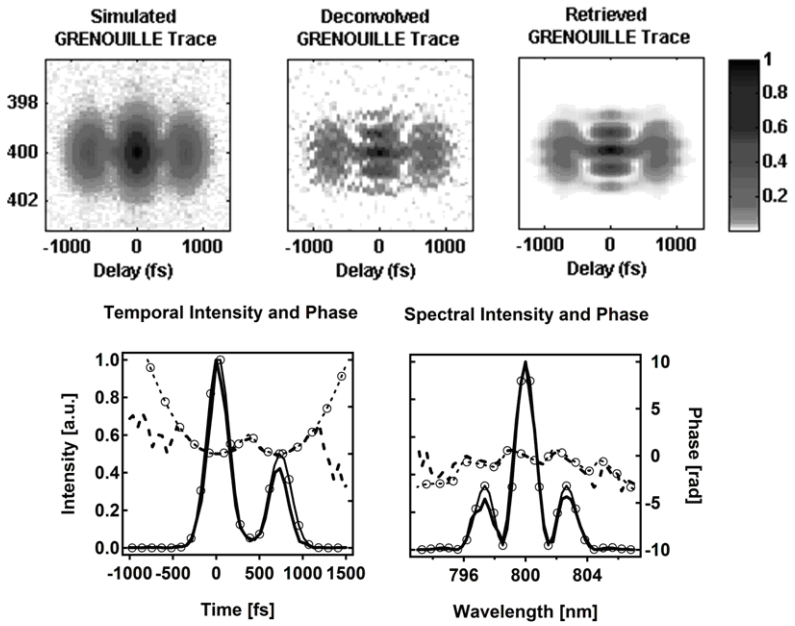

Figure 41: Deconvolution when noise is present.

excellent agreement with the actual pulse temporal and spectral intensities and phases in 40(e) and 40(f). The solid curves with circular markers show the actual temporal and spectral intensities. The dotted curves with circular markers refers to the actual signal temporal and spectral phases. The solid lines without any markers show the intensities of the retrieved pulses. The dotted lines without any marker are the corresponding phases of the retrieved pulse.

We have found that this deconvolution works well even in the presence of noise. In fact, Lucy-Richardson deconvolution is a quite noise-resistant deconvolution algorithm. We could apply the deconvolution procedure without additional numerical techniques such as filtering methods to remove the noise.

Using the same pulse in figure 40, figure 41(a) shows the GRENOUILLE trace including 1% additive Gaussian distribution noise. We deconvolve the trace first and then apply our FROG algorithm to the deconvoluted noisy trace to reconstruct the original real input(See figure 41(b-c)). Due to the naturally built-in redundancy in the FROG trace, our FROG algorithm converges very well. The rms error between

the FROG trace and the deconvolved GRENOUILLE trace was 0.020166. The rms error between the FROG trace and the retrieved GRENOUILLE trace was 0.008643.

In this chapter, we showed that numerical spectral deconvolution method is able to extend the operating range of a given GRENOUILLE to 1 ps or more. It works well even in the presence of noise. After deconvolution, the FROG algorithm converges much faster. Fine spectral structure 1 nm can be revealed. Thus, including spectral deconvolution, an pulse length range of a factor of 30 or more can be achieved from a simple, alignment-free device consisting of only four elements.

CHAPTER VI

TIGHT FOCUS EFFECT IN SECOND HARMONIC GENERATION BY LENS FOCUSING

6.1 Introduction

For the experiments involving the second harmonic generation process, quite often the ultrashort pulses are focused tightly into the nonlinear crystal by use of lenses. Contrary to what we would like to have, the lenses do not strictly conserve the beam temporal and spatial characteristics. In general, the pulse is broadened in time due to lens material dispersion[15]. A radius dependent delay between pulse and pulse fronts appears caused by chromatic aberration[14].Monochromatic aberrations (mainly spherical aberrations for on-axis focusing) will affect the spatial intensity distribution. The usual geometrical optics treatment could not adequately describe those temporal and spatial variations of an ultrashort pulse focused by lens. Wave optical theory studies have been carried out for the transformation of ultrashort pulses around the focal region of lenses[62, 61, 50]. Coupling between the temporal, spectral and spatial profiles have been revealed[62]. The spatial distribution is greatly affected by the spherical aberration when lenses are used[61].

GRENOUILLE uses tight focused beams in order to have a large angular spread[77]. Strange focusing effects have been observed when the beam focus is moving along the longitudinal axis z[76]. When the beam waist is focused at the position that correspond to the maximum SHG intensity, no distortion was observed. When the crystal was moved away from the lens so that the beam waist is moving towards the crystal incident surface, no distortions occurred. However, when moving the crystal closer to the lens so that the beam is focused towards the exit surface of the crystal, fringes

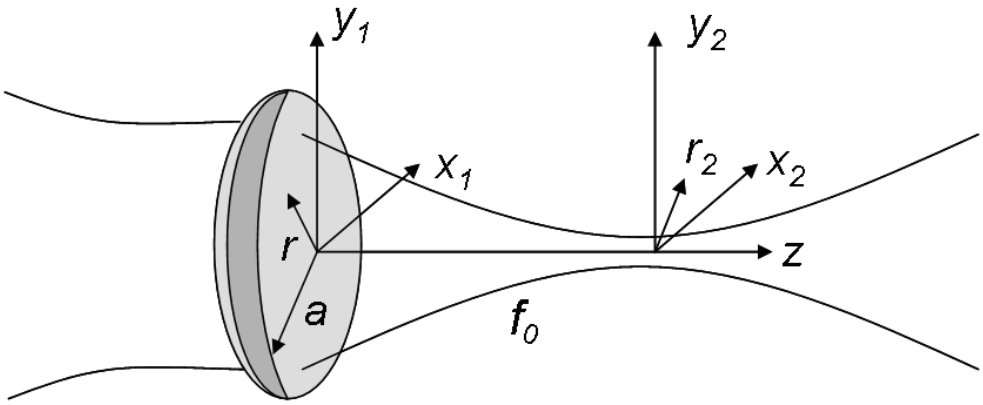

Figure 42: Geometry of Fourier optical analysis.

appeared in the measured traces. Using the model suggested by kempe[61] for focusing of ultrashort pulses by lenses, we found that the spherical aberration modifies the input beam spatial profile and introduces those spatial fringes in the SHG signal. This is not an appropriate practice for the GRENOUILLE device, which maps angle(wavelength) onto different vertical positions at the camera[93].

6.2 Second harmonic generation using beams tightly focused by a singlet lens

Transformation of the fundamental input beam with a thin plano-convex lens was calculated using the model developed by kempe[61](See appendix C). We assume the paraxial approximation is valid, since for our case the numerical aperture is 0.13 maximum. The pupil function $P(x_1, y_1)$ for a circular lens with diameter a(See figure 42) can be written as:

$$P(x_1, y_1) = \begin{cases} 1 & if x_1^2 + y_1^2 = r_1^2 = (ra)^2 r \in [0, 1] \\ 0 & else \end{cases} \tag{100}$$

The focal length of the lens for the center wavelength is f_0. We assume the input beam has Gaussian temporal and spatial profile, $E(t, r) = \exp(-t^2/T^2)\exp(-\frac{r^2}{w^2})$.

The electric field distribution after the lens was analyzed by Fourier optics[61],

$$\begin{aligned} u(v,u,t) \propto & \int_0^1 r dr J_0(rv) \exp(-\tfrac{r^2}{w^2}) \exp(-i\tfrac{1}{2}ur^2) \exp(-iAr^4) \\ & \sqrt{\tfrac{1+i\delta(r,T)}{1+\delta^2(r,T)}} \exp\{-\tfrac{(t+\tau r^2)^2}{T^2[1+\delta^2(r,T)]}[1+i\delta(r,T)]\} \end{aligned} \tag{101}$$

where $v = ak_0 r_2/f_0$ and $u = a^2 k_0(1/f_0 - 1/z)$ are the optical coordinates. The parameter measures the pulse broadening,

$$\tau = \frac{a^2 k_0}{2f_0(n_0-1)} \left.\frac{dn}{d\omega}\right|_{\omega=\omega_0} \tag{102}$$

and

$$\delta(r,T) = 4(\delta' - \delta r^2)/T^2. \tag{103}$$

The parameters δ and δ' are caused by the dispersion of the lens material with thickness of d[85] up to the second order. δ introduces a phase modulation and δ' causes a radius dependent chirp,

$$\begin{aligned} \delta &= \tfrac{a^2 k_0}{2f_0(n_0-1)}(\tfrac{1}{\omega_0} \left.\tfrac{dn}{d\omega}\right|_{\omega=\omega_0} + \tfrac{1}{2} \left.\tfrac{d^2 n}{d\omega^2}\right|_{\omega=\omega_0}), \\ \delta' &= k_0 d(\tfrac{1}{\omega_0} \left.\tfrac{dn}{d\omega}\right|_{\omega=\omega_0} + \tfrac{1}{2} \left.\tfrac{d^2 n}{d\omega^2}\right|_{\omega=\omega_0}). \end{aligned} \tag{104}$$

$A = -k_0\phi^{(4)}$ relates to the spherical aberration[15]. For a thin plano-convex lens with a diameter of a,

$$\phi^{(4)} = -\frac{n_0^2(n_0^2-4)+2n_0+4}{8n_0(n_0-1)^2(n_0+2)} ra(\frac{ra}{f_0})^3 \tag{105}$$

We then propagate the focused fundamental beam inside a second harmonic BBO crystal. Assuming that the fundamental is not depleted, the second harmonic generation process is simulated using the following wave equation[87].

$$\begin{aligned} & [\tfrac{\partial}{\partial z} - \tfrac{i}{2k_2}(\tfrac{\partial^2}{\partial x^2} + \tfrac{\partial^2}{\partial y^2}) + (\tfrac{1}{V_2} - \tfrac{1}{V_1})\tfrac{\partial}{\partial t} + i\tfrac{1}{2}\tfrac{\partial^2 k_2}{\partial \omega^2}\tfrac{\partial^2}{\partial t^2}]E_2(x,y,z,t) \\ & = \tfrac{i\omega_2}{n_2 c} d_{eff} E_1^2(x,y,z,t) e^{-i\Delta k z} \end{aligned} \tag{106}$$

where E_1 and E_2 correspond to the fundamental and second harmonic electric field respectively. We take into account the beam diffraction and crystal dispersion up to the second order. d_{eff} is the effective nonlinearity and n is the effective refractive

index of the nonlinear crystal. $\Delta k = k_2 - 2k_1$ is the phase mismatch. We considered Type I phase-matching conditions in a BBO crystal and align the incident beam at the appropriate phase matching angle so that $\Delta k = 0$. $V_{j=1,2}$ is the group velocity along the direction of the k-vector of the pulse's carrier wave.

In the following studies, The spatially integrated intensity is calculated by

$$I(v) = \int_{-\infty}^{+\infty} dt \, |u(v,t).|^2 \tag{107}$$

6.3 Results

The fundamental beam centered at 800 nm is 100 fs long with a beam width radius of 4.25 mm at the incidence face of the lens. A Newport BK7 lens(KPX061) with a center thickness of 3.392 mm and a diameter of 12.7mm was used. The focal length was 100mm for 589 nm. For 800 nm center wavelength, the focal length is changed to be 101.179 mm and the beam width radius is about $6\mu m$($w = \lambda_0 f_0/\pi w_0$). We move our crystal around the focal plane $z = f_0$. Starting at a position that the crystal is placed 500 μm after the focus($z = f_0 + 500\mu m$), we move our crystal towards the focus until the focal plane is $800\mu m$ behind($z = f_0 - 800\mu m$).

When the focal plane is in front of the crystal, the spatial profile of the fundamental is quite well behaved, which means it is still Gaussian shaped, or close to 'Gaussian' shaped. Also no structures appears in the spatial profile of the SHG signal. Here we shown two typical cases: $z = f_0 + 200\mu m$ and $z = f_0 + 400\mu m$(see figure 43(e), (f) and (g), (h)).

When the focal plane is after the crystal, the spatial profile of the fundamental starts to develope structures, but no obvious disturbance happens to the spatial profile of the SHG signal until positions around $z = f_0 - 700\mu m$. We show the situations when $z = f_0 - 800\mu m$(see figure 43(a))and $z = f_0 - 700\mu m$(see figure 43(c)). Fringes appear in the spatial profiles of their correspondent SHG signal(see 43(b) and 43(d)).

When turning off the spherical abberation($A = 0$), interestingly those effects went away(see figure 43(a'), (b') and 43(c'), (d')).

Our simulation yields an 'asymmetrical' pattern of the SH signal around the focus, which follows what has been described in the experiment. For GRENOUILLE the wavelength axis corresponds to the vertical direction along the camera. So the spatial disturbance caused by the spherical abberation has to be avoided. Working in a safe operation region means we should never focus the beam at the back of the crystal for a GRENOUILLE apparatus.

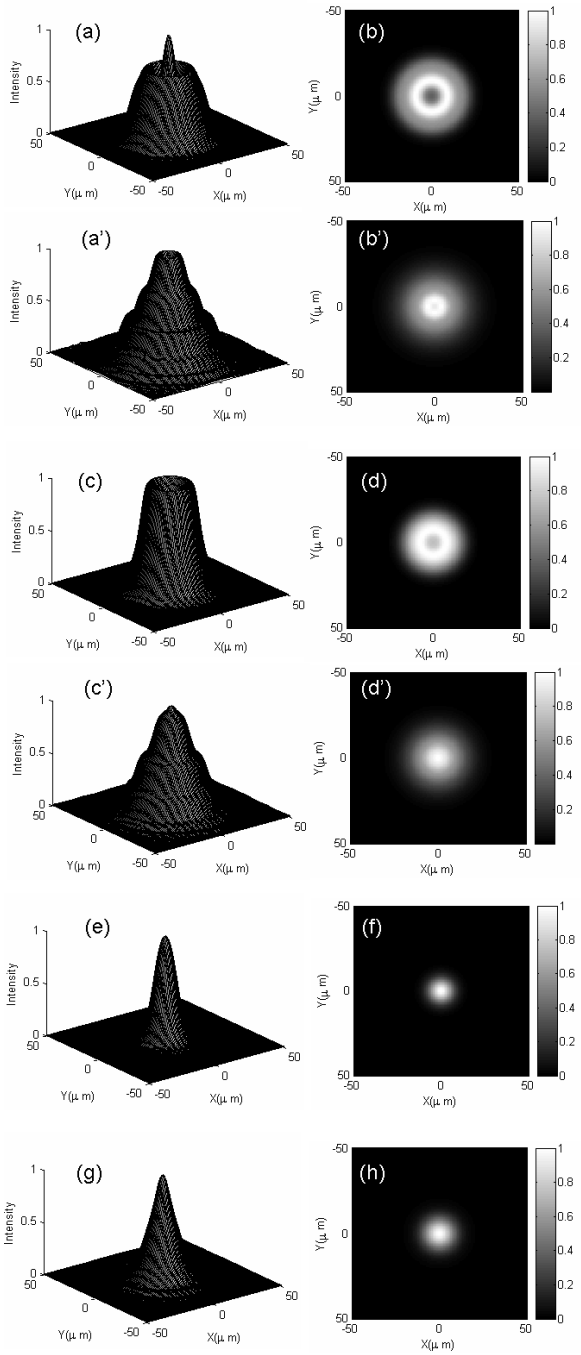

Figure 43: Left:Spatial profiles of the fundamental. Right:Correspondent SHG spatial profiles. (a)at $z = f_0 - 800\mu m$. (a') at $z = f_0 - 800\mu m$, but without spherical abberation.(c)at $z = f_0 - 700\mu m$.(c')at $z = f_0 - 700\mu m$, but without spherical abberation.(e)at $z = f_0 + 200\mu m$. (g)at $z = f_0 + 400\mu m$.

APPENDIX A

RUNGE-KUTTA METHODS

We used Runde-Kutta methods[9, 45, 81] to solve the first order coupled differential equations in chapter 3. For better understanding of the Runge-Kutta methods, we begin with solving the first order ODE of the form

$$\frac{dy}{dx} = f(x, y), \quad y(0) = y_0 \tag{108}$$

by using Runge-Kutta 2^{nd} order approach. For a small step h, $y(x + h)$ can be expanded in Taylor series:

$$\begin{aligned} y(x+h) &= y(x) + hy'(x) + \tfrac{h^2}{2}y''(x) + o(h^3) \\ &= y(x) + hf(x, y) + \tfrac{h^2}{2}y''(x) + o(h^3) \end{aligned} \tag{109}$$

The second order derivative of $y(x)$ can be written as

$$\begin{aligned} y''(x) &= f'(x, y) = \tfrac{\partial f(x,y)}{\partial x} + \tfrac{\partial f(x,y)}{\partial y}\tfrac{dy}{dx} \\ &= \tfrac{\partial f(x,y)}{\partial x} + \tfrac{\partial f(x,y)}{\partial y} f(x, y) \end{aligned} \tag{110}$$

Insert equation 110 back to equation 109, we have

$$y(x + h) = y(x) + hf(x, y) + \frac{h^2}{2}[f_x + f_y f(x, y)] + o(h^3) \tag{111}$$

The Runge-Kutta method estimate the slope over the step using a linear combination of the function f(x,y) evaluated at certain points in the step:

$$y(x + h) = y(x) + Ahf_0 + Bhf_1 \tag{112}$$

where $f_0 = f(x, y)$ and $f_1 = f(x + Ph, y + Qhf_0)$. Expanding f_1 in Taylor series:

$$f_1 = f(x, y) + f_x Ph + f_y Qhf_0 + o(h^2) \tag{113}$$

Equation 112 can be rewritten as:

$$y(x+h) = y(x) + (A+B)hf + BPh^2 f_x + BQh^2 f_y f \tag{114}$$

Comparing 114 with 111, we have

$$A + B = 1 \quad BP = 1/2 \quad BQ = 1/2 \tag{115}$$

Since we have 3 equations and 4 unknowns, we can assume the value of $A = 0$, this leads to the 2^{nd} Runge-Kutta formula

$$y(x+h) = y(x) + hf(x + \frac{h}{2}, y + \frac{h}{2} f(x,y)). \tag{116}$$

For better accuracy, we need to consider higher order Runge-Kutta methods. For the fourth order Runge-Kutta scheme, we can write it in the form:

$$y(x+h) = y(x) + w_1 k_1 + w_2 k_2 + w_3 k_3 + w_4 k_4, \tag{117}$$

where $w_1, ...$ are the weights, and the $k_1, ...$ are given by,

$$\begin{aligned} k_1 &= hf(x,y) \\ k_2 &= hf(x + a_1 h, y + b_1 k_1) \\ k_3 &= hf(x + a_2 h, y + b_2 k_1 + b_3 k_2) \\ k_4 &= hf(x + a_3 h, y + b_4 k_1 + b_5 k_2 + b_6 k_3) \end{aligned} \tag{118}$$

Using method similar to the one used in the above second order Runge-Kutta method, but writing the Taylor series to fourth order in h, it can be shown that there are eleven equations and thirteen unknown coefficients to decide. The most frequently used choice of the constants are as following:

$$y(x+h) = y(x) + \frac{h}{6}(f_1 + 2f_2 + 2f_3 + f_4) \tag{119}$$

where

$$\begin{aligned} f_1 &= f(x,y), \\ f_2 &= f(x + \tfrac{h}{2}, y + \tfrac{h}{2} f_1), \\ f_3 &= f(x + \tfrac{h}{2}, y + \tfrac{h}{2} f_2), \\ f_4 &= f(x + h, y + f_3). \end{aligned} \tag{120}$$

For solving three coupled 1^{st} ODEs:

$$\frac{dE_1}{dz} = f(E_1, E_2, E_3, z), \quad \frac{dE_2}{dz} = g(E_1, E_2, E_3, z), \quad \frac{dE_3}{dz} = q(E_1, E_2, E_3, z) \tag{121}$$

Es' are calculated as following for small increments:

$$\begin{aligned} E_1^{(n+1)} &= E_1^{(n)} + \tfrac{k_1+2k_2+2k_3+k_4}{6} \\ E_2^{(n+1)} &= E_2^{(n)} + \tfrac{l_1+2l_2+2l_3+l_4}{6} \\ E_3^{(n+1)} &= E_3^{(n)} + \tfrac{s_1+2s_2+2s_3+s_4}{6} \end{aligned} \tag{122}$$

where,

$$\begin{aligned} k_1 &= f(E_1^{(n+1)}, E_2^{(n+1)}, E_3^{(n+1)}, z)\Delta z \\ l_1 &= g(E_1^{(n+1)}, E_2^{(n+1)}, E_3^{(n+1)}, z)\Delta z \\ s_1 &= q(E_1^{(n+1)}, E_2^{(n+1)}, E_3^{(n+1)}, z)\Delta z \\ k_2 &= f(E_1^{(n+1)} + \tfrac{k_1}{2}, E_2^{(n+1)} + \tfrac{l_1}{2}, E_3^{(n+1)} + \tfrac{s_1}{2}, z + \tfrac{\Delta z}{2})\Delta z \\ l_2 &= g(E_1^{(n+1)} + \tfrac{k_1}{2}, E_2^{(n+1)} + \tfrac{l_1}{2}, E_3^{(n+1)} + \tfrac{s_1}{2}, z + \tfrac{\Delta z}{2})\Delta z \\ s_2 &= q(E_1^{(n+1)} + \tfrac{k_1}{2}, E_2^{(n+1)} + \tfrac{l_1}{2}, E_3^{(n+1)} + \tfrac{s_1}{2}, z + \tfrac{\Delta z}{2})\Delta z \\ k_3 &= f(E_1^{(n+1)} + \tfrac{k_2}{2}, E_2^{(n+1)} + \tfrac{l_2}{2}, E_3^{(n+1)} + \tfrac{s_2}{2}, z + \tfrac{\Delta z}{2})\Delta z \\ l_3 &= g(E_1^{(n+1)} + \tfrac{k_2}{2}, E_2^{(n+1)} + \tfrac{l_2}{2}, E_3^{(n+1)} + \tfrac{s_2}{2}, z + \tfrac{\Delta z}{2})\Delta z \\ s_3 &= q(E_1^{(n+1)} + \tfrac{k_2}{2}, E_2^{(n+1)} + \tfrac{l_2}{2}, E_3^{(n+1)} + \tfrac{s_2}{2}, z + \tfrac{\Delta z}{2})\Delta z \\ k_4 &= f(E_1^{(n+1)} + k_3, E_2^{(n+1)} + l_3, E_3^{(n+1)} + s_3, z + \Delta z)\Delta z \\ l_4 &= g(E_1^{(n+1)} + k_3, E_2^{(n+1)} + l_3, E_3^{(n+1)} + s_3, z + \Delta z)\Delta z \\ s_4 &= q(E_1^{(n+1)} + k_3, E_2^{(n+1)} + l_3, E_3^{(n+1)} + s_3, z + \Delta z)\Delta z \end{aligned} \tag{123}$$

APPENDIX B

CALCULATION OF THE APPARENT GROUP VELOCITY AND GROUP VELOCITY DISPERSION

The following discussion follows the derivation by Dr. Arlee V. Smith 's Optics Letter paper[89]. Assuming the propagation vector k is tilted at an angle δ with respect to the z axis. v is the group velocity of an unslanted pulse. For a extraordinary wave, the group velocity is tilted by a small angle ρ and becomes v'. Imagine the incident pulse is diffracted by an grating and makes an angle ψ relative to its k vector. Its pulse front is then slanted at an angle ϕ relative to the normal to z. From diffraction theory,

$$k(\omega, \psi) \sin\psi = grating \quad vector \tag{124}$$

Differentiating eq. 124 with respect to ω, we have

$$\frac{\partial k}{\partial \psi}\frac{d\psi}{d\omega}\sin\psi + \frac{\partial k}{\partial \omega}\sin\psi + k\cos\psi\frac{d\psi}{d\omega} = 0 \tag{125}$$

Using the definition of group velocity and birefringent walk off: $v = \partial\omega/\partial k$ and $tan(\rho) = -(1/k)\partial k/\partial\delta$ together with relation $\psi = \phi + \delta$, we have

$$\frac{d\delta}{d\omega} = -\frac{1}{vk}\frac{\sin(\delta+\phi)\cos\rho}{\cos(\delta+\phi+\rho)} \tag{126}$$

.

The apparent group velocity is defined as the velocity v_z at which point a sweeps along z.

$$\begin{aligned} \hat{v} = v_z &= v'\cos(\delta+\rho) - h\tan\phi \\ &= \tfrac{v}{\cos\rho}\cos(\delta+\rho) - \tfrac{v}{\cos\rho}\sin(\delta+\rho)\tan\phi \\ &= v\tfrac{\cos(\delta+\rho+\phi)}{\cos\rho\cos\phi} \end{aligned} \tag{127}$$

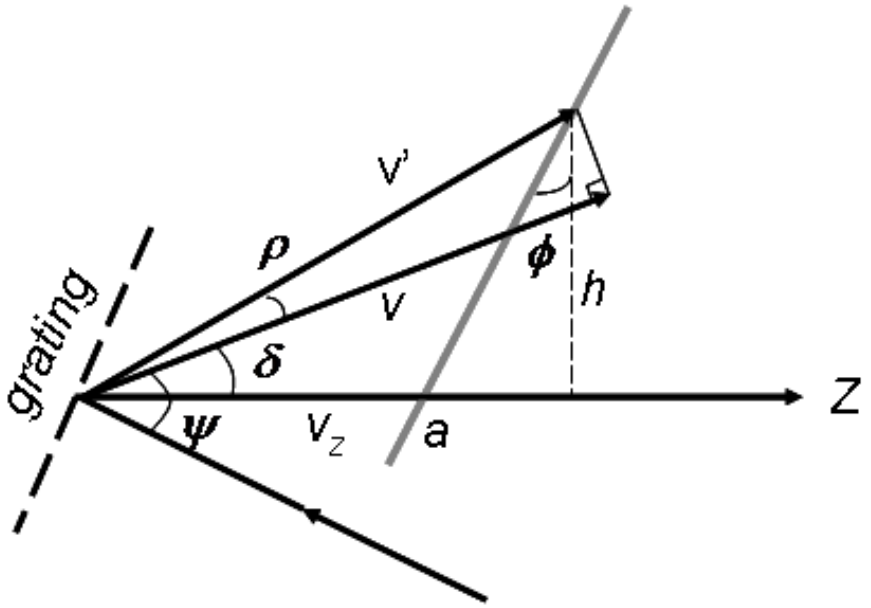

Figure 44: Diagram for calculation of the apparent group velocity of a slanted pulse.

The apparent group velocity dispersion is defined as:

$$\begin{aligned}
&\hat{D} = -\tfrac{1}{2}\tfrac{dk_z^2}{d\omega^2} = -\tfrac{1}{2}\tfrac{d}{d\omega}(\tfrac{1}{\hat{v}}) = \tfrac{1}{2\hat{v}^2}\tfrac{d\hat{v}}{d\omega} \\
&= \tfrac{1}{2\hat{v}^2}\big[\tfrac{\cos(\delta+\rho+\phi)}{\cos\rho\cos\phi}\tfrac{dv}{d\omega} + \tfrac{v}{\cos\rho\cos\phi}\tfrac{d\cos(\delta+\rho+\phi)}{d\omega} - v\tfrac{\cos(\delta+\rho+\phi)}{\cos^2\rho\cos\phi}\tfrac{d\cos\rho}{d\omega}\big] \\
&= \tfrac{1}{2\hat{v}^2}\big[\tfrac{\cos(\delta+\rho+\phi)}{\cos\rho\cos\phi}(\tfrac{\partial v}{\partial\omega} + \tfrac{\partial v}{\partial\delta}\tfrac{d\delta}{d\omega})\big] + \\
&-\tfrac{1}{2v}\tfrac{\cos\rho\cos\phi}{\cos^2(\delta+\rho+\phi)}\sin(\delta+\rho+\phi)(\tfrac{d\delta}{d\omega} + \tfrac{d\rho}{d\omega}) \\
&+\tfrac{1}{2v}\tfrac{\cos\phi\sin\rho}{\cos(\delta+\rho+\phi)}\tfrac{d\rho}{d\omega} \\
&= -\tfrac{1}{2}\tfrac{\cos\rho\cos\phi}{\cos(\delta+\rho+\phi)}gvd - \tfrac{1}{2v^3k}\tfrac{\cos^2\rho\cos\phi\sin(\delta+\phi)}{\cos^2(\delta+\rho+\phi)}\tfrac{\partial v}{\partial\delta} \\
&+\tfrac{1}{2v^2k}\tfrac{\cos^2\rho\cos\phi\sin(\delta+\rho+\phi)\sin(\delta+\phi)}{\cos^3(\delta+\rho+\phi)} \\
&-\tfrac{1}{2v}\tfrac{\sin(\delta+\phi)\cos\phi}{\cos^2(\delta+\rho+\phi)}\tfrac{d\rho}{d\omega}
\end{aligned} \tag{128}$$

Now, we evaluate $\partial v/\partial\alpha$:

$$\begin{aligned}
&\tfrac{\partial v}{\partial\delta} = -v^2\tfrac{\partial}{\partial\delta}\tfrac{\partial k}{\partial\omega} = -v^2\tfrac{\partial}{\partial\omega}\tfrac{\partial k}{\partial\delta} \\
&= v^2\tfrac{\partial}{\partial\omega}(k\tan\rho) = v\tan\rho + v^2k\tfrac{\partial}{\partial\omega}(\tan\rho)
\end{aligned} \tag{129}$$

We also need to evaluate $d\rho/d\omega$:

$$\begin{aligned}
&\tfrac{d\rho}{d\omega} = \cos^2\rho \tfrac{d\tan\rho}{d\omega} \\
&= \cos^2\rho(\tfrac{\partial\tan\rho}{\omega}) + \tfrac{1}{vk}\tfrac{\sin(\delta+\phi)\cos^3\rho}{\cos(\delta+\phi+\rho)}\tfrac{\partial}{\partial\delta}\tan\rho \\
&= \cos^2\rho(\tfrac{\partial\tan\rho}{\omega}) + \tfrac{1}{vk}\tfrac{\sin(\delta+\phi)\cos^3\rho}{\cos(\delta+\phi+\rho)}\tfrac{\partial}{\partial\delta}(-\tfrac{1}{k}\tfrac{\partial k}{\partial\delta}) \\
&= \cos^2\rho(\tfrac{\partial\tan\rho}{\omega}) - \tfrac{1}{vk}\tfrac{\sin(\delta+\phi)\cos^3\rho}{\cos(\delta+\phi+\rho)}(-\tfrac{1}{k}\tan\rho - \tfrac{1}{k}\tfrac{\partial^2 k}{\partial\delta^2}) \\
&= \cos^2\rho(\tfrac{\partial\tan\rho}{\omega}) + \tfrac{1}{vk^2}\tfrac{\sin(\delta+\phi)\cos^3\rho}{\cos(\delta+\phi+\rho)}(\tan\rho + k - 2k^2A) \\
&= \cos^2\rho(\tfrac{\partial\tan\rho}{\omega}) + \tfrac{1}{vk^2}\tfrac{\sin(\delta+\phi)\cos^2\rho\sin\rho}{\cos(\delta+\phi+\rho)} + \tfrac{1}{vk}\tfrac{\sin(\delta+\phi)\cos^3\rho}{\cos(\delta+\phi+\rho)} \\
&-\tfrac{2}{v}\tfrac{\sin(\delta+\phi)\cos^3\rho}{\cos(\delta+\phi+\rho)}A
\end{aligned} \tag{130}$$

where

$$A = \frac{1}{2k} - \frac{1}{2k^2}\frac{\partial^2 k}{\partial\delta^2} \tag{131}$$

Insert eq.129 and 130 back into eq. 128 and neglect $\partial(tan\rho)/\partial\omega$:

$$\begin{aligned}
&\hat{D} = -\tfrac{1}{2}\tfrac{\cos\rho\cos\phi}{\cos(\delta+\rho+\phi)}gvd + \tfrac{1}{v^2}\tfrac{\sin^2(\delta+\phi)\cos^3\rho\cos\phi}{\cos^3(\delta+\rho+\phi)}A \\
&+\tfrac{1}{2v^2k}\tfrac{\cos\phi\sin^2(\delta+\phi)\cos\rho\sin^2\rho}{\cos^3(\delta+\rho+\phi)} \\
&-\tfrac{1}{2v^2k^2}\tfrac{\sin^2(\delta+\phi)\cos^2\rho\sin\rho\cos\phi}{\cos^3(\delta+\rho+\phi)}
\end{aligned} \tag{132}$$

Since $A \approx 1/2k$, the third and last terms are smaller by the order of ρ^2 and ρ/k than the second term respectively, they can be neglected. So we have

$$\begin{aligned}
&\hat{D} = -\tfrac{1}{2}\tfrac{d^2k_z}{d\omega^2} = \tfrac{1}{2V_g^2}\tfrac{\cos\phi\cos\rho}{\cos(\alpha+\phi+\rho)}GVD \\
&+\tfrac{1}{V_g^2}\tfrac{\cos\phi\cos^3\rho\sin^2(\alpha+\phi)}{\cos^3(\alpha+\phi+\rho)}A
\end{aligned} \tag{133}$$

where $GVD = \partial v/\partial\omega$.

APPENDIX C

ULTRASHORT LIGHT PULSES FOCUSED BY LENSES

The scalar electric field amplitude $U(r,\omega)$ has to satisfy the well known Helmholtz equation[15],

$$[\nabla^2 + k(\omega)^2]U(r,\omega) = 0 \tag{134}$$

After propagating through the lens, the field amplitude at z is transformed to be

$$\begin{aligned} U(x_2,y_2,z,\omega) &\propto \int_{-\infty}^{+\infty}\int_{-\infty}^{+\infty} dx_1 dy_1 P(x_1,y_1)A(\Delta\omega)\Theta(x_1,y_1) \\ &\times \exp\{\tfrac{ik_a}{2z}[(x_2-x_1)^2+(y_2-y_1)^2]\} \end{aligned} \tag{135}$$

where

$$\Theta(x_1,y_1) = \exp(ik_l d)\exp[-i(k_l-k_a)\frac{x_1^2+y_1^2}{2}(\frac{1}{R_1}-\frac{1}{R_2})] \tag{136}$$

$$P(x_1,y_1) = \begin{cases} 1 if x_1^2+y_1^2 = r_1^2 = (ra)^2 r \in [0,1] \\ 0 else \end{cases} \tag{137}$$

Let $x_1 = r_1\cos\phi$, $y_1 = r_1\sin\phi$, $x_2 = r_2\cos\varphi$ and $y_2 = r_2\sin\varphi$, using thin lens relation $\frac{1}{f_0} = (n_o-1)(\frac{1}{R_1}-\frac{1}{R_2})$, we have

$$\begin{aligned} U(r_2,\varphi,z,\omega) &\propto \int_0^1\int_0^{2\pi} r_1 dr_1 d\phi A(\Delta\omega)\exp(ik_l d) \\ &\times \exp[-i(k_l-k_a)\tfrac{r_1^2}{2}\tfrac{1}{f_0(n_0-1)}] \\ &\times \exp\{\tfrac{ik_a}{2z}[r_1^2+r_2^2-2r_1r_2\cos(\phi-\varphi)]\} \end{aligned} \tag{138}$$

It is symmetric with respect of ϕ

$$\begin{aligned} U(r_2,z,\omega) &\propto \int_0^1\int_0^{2\pi} r_1 dr_1 d\phi A(\Delta\omega)\exp(ik_l d) \\ &\times \exp[-i(k_l-k_a)\tfrac{r_1^2}{2}\tfrac{1}{f_0(n_0-1)}] \\ &\times \exp\{\tfrac{ik_a}{2z}[r_1^2+r_2^2-2r_1r_2\cos\varphi]\} \end{aligned} \tag{139}$$

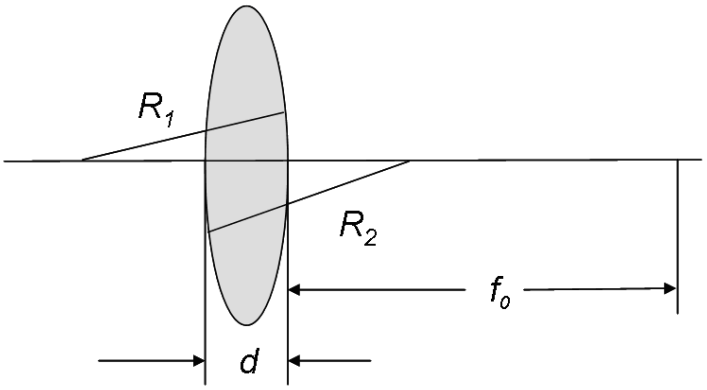

Figure 45: The lens parameters.

where,

$$\begin{aligned}
&k_l = \tfrac{\omega}{c} n(\omega) \simeq k_0 n_0 [1 + a_1 \Delta\omega + a_2 \Delta\omega^2] \\
&a_1 = \tfrac{1}{\omega_0} + \tfrac{1}{n_0} \left.\tfrac{dn}{d\omega}\right|_{\omega=\omega_0}, \\
&a_2 = \tfrac{1}{\omega_0 n_0} \left.\tfrac{dn}{d\omega}\right|_{\omega=\omega_0} + \tfrac{1}{2n_0} \left.\tfrac{d^2 n}{d\omega^2}\right|_{\omega=\omega_0}, \\
&k_a = \tfrac{\omega}{c} = k_0 (1 + \tfrac{\Delta\omega}{\omega_0}), \\
&k_l - k_a = \tfrac{\omega}{c} [n(\omega) - 1] \simeq k_0 (n_0 - 1)[1 + b_1 \Delta\omega + b_2 \Delta\omega^2]
\end{aligned} \tag{140}$$

Let

$$\begin{aligned}
b_1 &= \tfrac{n_0 a_1 \omega_0 - 1}{\omega_0 (n_0 - 1)} = \tfrac{1}{\omega_0} [1 + \tfrac{\omega_0 n(\omega_0)'}{(n_0 - 1)}] \\
b_2 &= \tfrac{n_0 a_2}{n_0 - 1} = \tfrac{n(\omega_0)'}{(n_0 - 1)\omega_0} + \tfrac{n(\omega_0)''}{2(n_0 - 1)}
\end{aligned} \tag{141}$$

We have

$$\begin{aligned}
&U(r_2, z, \omega) \propto \int_0^1 \int_0^{2\pi} r_1 dr_1 d\phi A(\Delta\omega) \exp(i k_0 n_0 [1 + a_1 \Delta\omega + a_2 \Delta\omega^2] d) \\
&\times \exp[-i \tfrac{k_0}{2 f_0} [1 + b_1 \Delta\omega + b_2 \Delta\omega^2] r_1^2] \\
&\times \exp\{\tfrac{i}{2z} k_0 (1 + \tfrac{\Delta\omega}{\omega_0}) [r_1^2 + r_2^2 - 2 r_1 r_2 \cos\varphi]\} \\
&\propto A(\Delta\omega) \exp(i k_0 n_0 d \Delta\omega [a_1 + a_2 \Delta\omega]) \exp[\tfrac{i}{2z} k_0 (1 + \tfrac{\Delta\omega}{\omega_0}) r_2^2] \int_0^1 \int_0^{2\pi} r_1 dr_1 d\phi \\
&\times \exp[-i \tfrac{k_0}{2} (\tfrac{1}{f_0} - \tfrac{1}{z}) r_1^2] \exp[\tfrac{-i}{z} k_0 (r_1 r_2 \cos\varphi)(1 + \tfrac{\Delta\omega}{\omega_0})] \\
&\times \exp[-i \tfrac{k_0}{2 f_0} [b_1 - \tfrac{f_0}{z\omega_0} + b_2 \Delta\omega] r_1^2 \Delta\omega]
\end{aligned} \tag{142}$$

Use optical coordinates, $v = ak_0 r_2/f_0$ and $u = a^2 k_0(1/f_0 - 1/z)$,

$$\begin{aligned} &U(r_2, z, \omega) \propto A(\Delta\omega)\exp(ik_0 n_0 d\Delta\omega[a_1 + a_2\Delta\omega])\exp[\tfrac{i}{4Nz}(1+\tfrac{\Delta\omega}{\omega_0})v^2 f_0] \\ &\int_0^1 r dr \exp[-i\tfrac{a^2 k_0}{2f_0}\Delta\omega(b_1 - \tfrac{f_0}{z\omega_0} + b_2\Delta\omega)r^2]\exp[-i\tfrac{1}{2}r^2 u] \\ &\times \int_0^{2\pi} d\phi \exp[\tfrac{-i}{z} f_0 r v\cos\varphi(1+\tfrac{\Delta\omega}{\omega_0})] \end{aligned} \tag{143}$$

The Fresnel number is defined as $N = a^2 k_0/(2f_0)$[101] and we know

$$\begin{aligned} &\int_0^{2\pi} d\phi \exp[\tfrac{-i}{z} f_0 r v\cos\varphi(1+\tfrac{\Delta\omega}{\omega_0})] \simeq \int_0^{2\pi} d\phi \exp[-irv\cos\varphi(1+\tfrac{\Delta\omega}{\omega_0})] \\ &= 2J_0[rv(1+\tfrac{\Delta\omega}{\omega_0})] \end{aligned} \tag{144}$$

Here we replaced z with f_0 in the phase term. The time domain expression will be

$$\begin{aligned} &u(v,u,t) \propto \int d\Delta\omega \exp(-i\Delta\omega t)A(\Delta\omega)\exp(ik_0 n_0 d\Delta\omega[a_1 + a_2\Delta\omega])\exp[\tfrac{i}{4Nz}(1+\tfrac{\Delta\omega}{\omega_0})v^2 f_0] \\ &\times \int_0^1 r dr \exp[-i\tfrac{a^2 k_0}{2f_0}\Delta\omega(b_1 - \tfrac{f_0}{z\omega_0} + b_2\Delta\omega)r^2]\exp[-i\tfrac{1}{2}r^2 u]J_0[rv(1+\tfrac{\Delta\omega}{\omega_0})] \\ &= \int d\Delta\omega A(\Delta\omega)\exp(ik_0 n_0 d a_2\Delta\omega^2])\exp[\tfrac{i}{4Nz}(1+\tfrac{\Delta\omega}{\omega_0})v^2 f_0] \\ &\times \int_0^1 r dr J_0[rv(1+\tfrac{\Delta\omega}{\omega_0})]\exp[-i\tfrac{1}{2}r^2 u]\exp\{-i\Delta\omega[t - k_0 n_0 d a_1 + \tfrac{a^2 k_0}{2f_0}(b_1 - \tfrac{f_0}{z\omega_0} + b_2\Delta\omega)r^2]\} \end{aligned} \tag{145}$$

Let,

$$\begin{aligned} \delta &= \tfrac{a^2 k_0}{2f_0} b_2, \\ \delta' &= k_0 n_0 d a_2 \\ \tau(u) &= \tfrac{a^2 k_0}{2f_0}(b_1 - \tfrac{f_0}{z\omega_0}) \\ \tau' &= k_0 n_0 d a_1 \end{aligned} \tag{146}$$

We can rewrite the electric field as,

$$\begin{aligned} &u(v,u,t) \propto \int d\Delta\omega A(\Delta\omega)\exp[\tfrac{i}{4Nz}(1+\tfrac{\Delta\omega}{\omega_0})v^2 f_0] \\ &\times \int_0^1 r dr J_0[rv(1+\tfrac{\Delta\omega}{\omega_0})]\exp(-i\tfrac{1}{2}ur^2)\exp[i\Delta\omega^2(\delta' - \delta r^2)]\exp[-i\Delta\omega(t - \tau' + \tau(u)r^2)] \end{aligned} \tag{147}$$

Usually, $N >> v^2/4$[101] and we can ignore the correspondent phase term. In the above derivation, we have assumed the lens is homogeneous illuminated and there is no higher order aberrations. However, the spherical aberration is an unavoidable

effect for singlet lens imaging. The electric field amplitude is calculated by (τ' is independent of the radius and not of interest)

$$\begin{aligned} u(v,u,t) \propto & \int_{-\infty}^{+\infty} d\Delta\omega A(\Delta\omega) \int_0^1 r dr J_0[rv(1+\tfrac{\Delta\omega}{\omega_0})] \exp(-\tfrac{r^2}{w^2}) \exp(-iAr^4) \\ & \times \exp(-i\tfrac{1}{2}ur^2) \exp[i\Delta\omega^2(\delta' - \delta r^2)] \exp[-i\Delta\omega(t + \tau r^2 + ur^2/(2\omega_0))] \end{aligned} \tag{148}$$

Where $A = -k_0\phi^{(4)}$ and

$$\begin{aligned} \phi^{(4)} &= -\tfrac{n_0^2(n_0^2-4)+2n_0+4}{8n_0(n_0-1)^2(n_0+2)} ra(\tfrac{ra}{f_0})^3 \\ \tau &= \tfrac{a^2k_0}{2f_0(n_0-1)} \left.\tfrac{dn}{d\omega}\right|_{\omega=\omega_0} \end{aligned} \tag{149}$$

Let us assume the input pulse has a Gaussian temporal profile $A(t) = \exp(-t^2/T^2)$. Fourier transform it into the frequency domain $A(\omega) = \sqrt{\pi}T \exp(-T^2\omega^2/4)$. For most cases it is found[3] we can make the following approximation without introducing significant errors,

$$J_0[rv(1+\frac{\Delta\omega}{\omega_0})] \approx J_0(rv) \tag{150}$$

Now we can integrate the above expression over $\Delta\omega$,

$$\begin{aligned} u(v,u,t) \propto & \int_0^1 r dr J_0(rv) \exp(-\tfrac{r^2}{w^2}) \exp(-iAr^4) \exp(-i\tfrac{1}{2}ur^2) \\ & \sqrt{\tfrac{1+i\delta(r,T)}{1+\delta^2(r,T)}} \exp\{-\tfrac{(t+\tau r^2)^2}{T^2[1+\delta^2(r,T)]}[1+\delta(r,T)]\} \end{aligned} \tag{151}$$

where $\delta(r,T) = 4(\delta' - \delta r^2)/T^2$.

REFERENCES

[1] Agrawal, G., *Nonlinear Fiber Optics*. Boston: Academic Press, 1995.

[2] Akturk, S., Gu, X., Zeek, E., and Trebino, R., "Pulse-front tilt caused by spatial and temporal chirp," *Optics Express*, vol. 12, no. 19, pp. 4399–4410, 2004.

[3] Akturk, S., Gu, X., Zeek, E., and Trebino, R., "Spatial chirp and pulse-front tilt in ultrashort laser pulses and their measurement," in *Ultrafast Phenomena*, (Niigata, Japan), 2004.

[4] Akturk, S., Kimmel, M., O'Shea, P., Tebino, R., Naumov, S., Sorokin, E., and Sorokina, I., "Measuring several-cycle 1.5-m pulses using frequency-resolved optical gating," *Optics Express*, vol. 11, no. 25, pp. 3461–3466, 2003.

[5] Akturk, S., Kimmel, M., O'Shea, P., and Trebino, R., "Measuring pulse-front tilt in ultrashort pulses using grenouille," *Optics Express*, vol. 11, pp. 491–501, 2003.

[6] Akturk, S., Kimmel, M., O'Shea, P., and Trebino, R., "Extremely simple device for measuring 20 fs pulses," *Optics Letters*, vol. 29, no. 9, pp. 1025–1027, 2004.

[7] Akturk, S., Kimmel, M., and Trebino, R., "Extremely simple device for measuring 1.5-m ultrashort laser pulses," *Optics Express*, vol. 12, no. 19, pp. 4483–4489, 2004.

[8] Akturk, S., Kimmel, M., Trebino, R., Naumov, S., Sorokin, E., and Sorokina, I., "Pulse-measurement challenges at 1.5 microns: several-cycle pulses and several-element devices," in *Ultrafast Phenomena*, (Niigata, Japan), 2004.

[9] Atkinson, K. E., *An Introduction to Numerical Analysis*. New York: John Wiley and Sons, 1989.

[10] Birge, J., Ell, R., and Krtner, F., "Two-dimensional spectral shearing inter- ferometry (2dsi) for ultrashort pulse character- ization," in *CLEO*, (Long Beach, California), 2006.

[11] Birge, J., Ell, R., and Krtner, F., "Two-dimensional spectral shearing interferometry for few-cycle pulse characterization," *Optics Letters*, vol. 31, pp. 2063–2065, 2006.

[12] Blass, W. and Halsey, G., *Deconvolution of Absorption Spectra*. New York: Academic Press, 1982.

[13] Bloembergen, N., *Nonlinear Optics, 4th ed.* NJ: World Scientific, 1996.

[14] Bor, Z., "Distorsion of femtosecond laser pulses in lenses and lens systems," *J. Mod. Opt.*, vol. 35, pp. 1907–1918, 1988.

[15] Born, M. and E., W., *Principles of Optics*. Pergamon, 1989.

[16] Boyd, R., *Nonlinear Optics*. Academic Press, 2003.

[17] Cameron, S. M., Bliss, D. E., Kimmel, M. W., and Neal, D. R., "3-dimensional reflective image-reconstruction through a scattering medium based on time-gated raman amplification," *US patent 5939739*, Aug 1999.

[18] Cerullo, G. and De Silvestri, S., "Ultrafast optical parametric amplifiers," *Review of Scientific Instruments*, vol. 74, pp. 1–18, 2003.

[19] Chenevix-Trench, G., "What makes a good phd student?," *Nature*, vol. 441, no. 7090, p. 252, 2006.

[20] Chung, J.-H. and Weiner, A. M., "Ambiguity of ultrashort pulse shapes retrieved from the intensity autocorrelation and the power spectrum," *IEEE J. Quantum Electron.*, vol. 7, pp. 656–666, 2001.

[21] Danielius, R., Piskarskas, A., DiTrapani, P., Andreoni, A., Solcia, C., and Foggi, P., "Matching of group velocities by spatial walk-off in collinear three-wave interaction with tilted pulses," *Optics Letters*, vol. 21, pp. 973–975, 1996.

[22] Daube-Witherspoon, M. E. and Muehllehner, G., "An iterative image reconstruction algorithm suitable for volume ect," *IEEE Trans Med Imag,*, vol. 5, pp. 16–22, 1986.

[23] DeLong, K., Fittinghoff, D. N., Trebino, R., Kohler, B., , and Wilson, k., "Pulse retrieval in frequency-resolved optical gating based on the method of generalized projections," *Optics Letters*, vol. 19, no. 24, pp. 2152–2154, 1994.

[24] DeLong, K., Fittinghoff, D., and Trebino, R., "Practical issues in ultrashort-laser-pulse measurement using frequency-resolved optical gating," *IEEE J. Quant. Electron.*, vol. 32, no. 7, pp. 1253–1264, 1996.

[25] DeLong, K., Fittinghoff, D., Trebino, R., Sullivan, A., Hunter, J., White, W., and Kane, D., "Frequency-resolved optical gating: Measuring the intensity and phase of an ultrashort laser pulse," in *Ultrafast Phenomena IX* (Barbara, P., Knox, W., Mourou, G., and Zewail, A., eds.), Springer Series in Chemical Physics, pp. 127–131, Berlin: Springer-Verlag, 1994.

[26] DeLong, K. and Trebino, R., "Improved ultrashort pulse-retrieval algorithm for frequency-resolved optical gating," *J. Opt. Soc. Am. A*, vol. 11, no. 9, pp. 2429–2437, 1994.

[27] DeLong, K. and Trebino, R., "Measuring the intensity and phase of two ultrashort pulses on a single shot," in *Generation, Amplification, and Measurement of Ultrashort Laser Pulses* (Trebino, R. and Walmsley, I., eds.), vol. 2116, pp. 268–274, Bellingham, WA: Society of Photo-Optical Instrumentation Engineers, 1994.

[28] DeLong, K., Trebino, R., Hunter, J., and White, W. E., "Frequency-resolved optical gating with the use of second-harmonic generation," *Journal of the Optical Society of America B-Optical Physics*, vol. 11, no. 11, pp. 2206–2215, 1994.

[29] DeLong, K., Trebino, R., and White, W. E., "Simultaneous recovery of two ultrashort laser pulses from a single spectrogram," *Journal of the Optical Society of America B-Optical Physics*, vol. 12, no. 12, pp. 2463–2466, 1995.

[30] Dempster, A., Laird, N., and Rubin, D., "Maximum likelihood from incomplete data via the em algorithm," *J. Roy. Statist. Soc. B.*, vol. 39, no. 1, pp. 1–38, 1977.

[31] Diels, J.-C., Fontaine, J. J., McMichael, I. C., and Simon, F., "Control and measurement of ultrashort pulse shapes (in amplitude and phase) with femtosecond accuracy," *Applied Optics*, vol. 24, pp. 1270–1282, 1985.

[32] Diels, J.-C. and Rudolph, W., *Ultrashort Laser Pulse Phenomena*. San Diego: Academic Press, 1996.

[33] Dreger, M. A., "Optical beam propagation in biaxial crystals," *Journal of Optics A: Pure and Applied Optics*, vol. 1, pp. 601–616, 1999.

[34] Dreger, M. A. and Mciver, J. K., "Second-harmonic generation in a nonlinear, anisotropic medium with diffraction and depletion," *Journal of the Optical Society of America B-Optical Physics*, vol. 7, pp. 776–784, 1990.

[35] Dudley, J. M., Gu, X., Xu, L., Kimmel, M., Zeek, E., O'Shea, P., Trebino, R., Coen, S., and Windeler, R. S., "Cross-correlation frequency resolved optical gating analysis of broadband continuum generation in photonic crystal fiber: simulations and experiments," *Optics Express*, vol. 10, pp. 1215–1221, 2002.

[36] Eimerl, D., Auerbach, J. M., and Milonni, P. W., "Paraxial wave theory of second and third harmonic generation in uniaxial crystals: I. narrowband pump fields," *Journal of Modern Optics*, vol. 42, pp. 1037–1067, 1995.

[37] Etchepare, J., Grillon, G., and Orszag, A., "Third order autocorrelation study of amplified subpicosecond laser pulses," *IEEE J. Quantum Electron*, vol. 19, pp. 775–778, 1983.

[38] Fienup, J. R., "Reconstruction of an object from modulus of its fourier-transform," *OPTICS LETTERS*, vol. 3, pp. 27–29, 1978.

[39] Fienup, J. R., "Phase retrieval algorithms: a comparison," *Appl. Opt.*, vol. 21, pp. 2758–2769, 1982.

[40] Fienup, J. R., "Reconstruction of a complex-valued object from the modulus of its fourier-transform using a support constraint," *JOURNAL OF THE OPTICAL SOCIETY OF AMERICA A-OPTICS IMAGE SCIENCE AND VISION*, vol. 4, pp. 118–123, 1987.

[41] Fienup, J. R. and C.C., W., "Improved phase-retrieval algorithm," *JOURNAL OF THE OPTICAL SOCIETY OF AMERICA A-OPTICS IMAGE SCIENCE AND VISION*, vol. 1, pp. 1320–1320, 1984.

[42] Fittinghoff, D. N., Bowie, J. L., Sweetser, J. N., Jennings, R. T., Krumbgel, M. A., DeLong, K. W., and Trebino, R., "Measurement of the intensity and phase of ultraweak, ultrashort laser pulse," *Optics Letters*, vol. 21, no. 12, pp. 884–886, 1996.

[43] Fittinghoff, D. N., DeLong, K. W.and Trebino, R., and Ladera, C. L., "Noise sensitivity in frequency-resolved optical-gating measurements of ultrashort pulses," *Journal of the Optical Society of America B-Optical Physics*, vol. 12, no. 10, pp. 1955–1967, 1995.

[44] Fleck, J. A. and Feit, M. D., "Beam propagation in uniaxial anisotropic media," *Journal of the Optical Society of America B-Optical Physics A-Optics, Image Science and Vision*, vol. 73, pp. 920–926, 1983.

[45] Forsythe, G. E., Malcolm, M. A., and Moler, C. B., *Computer Methods for Mathematical Computations*. NJ: Prentice-Hall: Englewood Cliffs, 1977.

[46] Froehly, C., Lacourt, A., and Vinot, J. C., "Time impulse response and time frequency response of optical pupils.:experimental confirmations and applications," *Nouvelle Revue d'Optique*, vol. 4, pp. 183–196, 1973.

[47] Gaeta, A. L., "Nonlinear propagation and continuum generation in microstructured optical fibers," *Optics Letters*, vol. 27, pp. 924–926, 2002.

[48] Gu, X., Xu, L., Zeek, E., O'Shea, P., Shreenath, A. P., Trebino, R., and Windeler, R. S., "Frequency-resolved optical gating and single-shot spectral measurements reveal fine structure in microstructure-fiber continuum," *Optics Letters*, vol. 27, pp. 1174–1176, 2002.

[49] Haacke, S., Berrehar, J., Lapersonne-Meyer, C., and Schott, M., "Dynamics of singlet excitons in 1d conjugated polydiacetylene chains: a femtosecond fluorescence study," *Chemical Physics Letters*, vol. 308, no. 5-6, pp. 363–368, 1999.

[50] Horvath, Z. and Bor, Z., "Focusing of femtosecond pulses having gaussian spatial distribution," *Opt. Comm.*, vol. 100, pp. 6–12, 1993.

[51] Iaconis, C. and Walmsley, I. A., "Spectral phase interferometry for direct electric-field reconstruction of ultrashort optical pulses," *Opt. Lett.*, vol. 23, pp. 792–795, 1998.

[52] Iaconis, C. and Walmsley, I. A., "Self-referencing spectral interferometry for measuring ultrashort optical pulses," *IEEE J. Quantum Electron*, vol. 35, pp. 501–509, 1999.

[53] Jain, A., *Fundamentals of digital image processing*. Upper Saddle River, NJ: Prentice-Hall, Inc., 1989.

[54] Jansson, P., *Deconvolution With Applications in Spectroscopy*. New York: Academic Press, 1984.

[55] Jansson, P., *Deconvolution of Images and Spectra*. New York: Academic Press, 1997.

[56] Kane, D., Taylor, A., Trebino, R., and DeLong, K., "Single-shot measurement of the intensity and phase of femtosecond uv laser pulse using frequency-resolved optical gating," *Optics Letters*, vol. 19, no. 14, pp. 1061–1063, 1994.

[57] Kane, D. and Trebino, R., "Characterization of arbitrary femtosecond pulses using frequency resolved optical gating," *IEEE J. Quant. Electron.*, vol. 29, no. 2, pp. 571–579, 1993.

[58] Kane, D. and Trebino, R., "Single-shot measurement of the intensity and phase of a femtosecond pulse," in *Ultrafast Pulse Generation and Spectroscopy* (Gosnell, T., Taylor, A., Nelson, K., and Downer, M., eds.), vol. 1861, pp. 150–160, Bellingham: SPIE Press, 1993. SPIE Jan 18-22, Los Angeles, CA.

[59] Kane, D. and Trebino, R., "Single-shot measurement of the intensity and phase of an arbitrary ultrashort pulse by using frequency-resolved optical gating," *Optics Letters*, vol. 18, no. 10, pp. 823–825, 1993.

[60] Kawano, K. and Kitoh, T., *ntroduction to Optical Waveguide Analysis*. New York: John Wiley and Sons, Inc, 2002.

[61] Kempe, M. and Rudolph, W., "Impact of chromatic and spherical aberration on the focusing of ultrashort light pulses by lenses," *Optics Letter*, vol. 18, pp. 137–139, 1993.

[62] Kempe, M., Stamm, U., Wilhelmi, B., and Rudolph, W., "Spatial and temporal transformation of femtosecond laser pulses by lenses and lens system," *Journal of the Optical Society of America B-Optical Physics*, vol. 14, pp. 1158–1165, 1992.

[63] Kintzer, E. S. and Rempel, C., "Near-surface second-harmonic generation for autocorrelation measurements in the uv," *Applied Physics B*, vol. 42, no. 2, pp. 91–95, 1987.

[64] Krylov, V., Gallus, J., Wild, U. P., Kalintsev, A., and Rebane, A., "Femtosecond noncollinear and collinear parametric generation and amplification in bbo crystal," *Applied Physics B-Lasers and Optics*, vol. 70, pp. 163–168, 2000.

[65] Landweber, L., "An iteration formula for fredholm integral equations of the first kind," *Am. J. Math.*, vol. 73, pp. 615–624, 1951.

[66] Lee, D. J., Akturk, S., Gabolde, P., and Trebino, R., "Experimentally simple, extremely broadband transient-grating frequency-resolved-optical-gating arrangement," *Optics Express*, vol. 15, pp. 760–766, 2007.

[67] Linden, S., Giessen, H., and Kuhl, J., "Xfrog-a new method for amplitude and phase characterization of weak ultrashort pulses," in *Physica Status Solidi B Conference Title: Phys. Status Solidi B*, vol. 206, (Germany), pp. 119–124, 1998.

[68] Linden, S., Kuhl, J., and Giessen, H., "Amplitude and phase characterization of weak blue ultrashort pulses by downconversion," *Optics Letters*, vol. 24, pp. 569–571, 1999.

[69] Liu, X., Shreenath, A., Kimmel, M., Trebino, R., Simith, A. V., and Link, S., "Numerical simulations of optical parametric amplification cross-correlation frequency-resolved optical gating," *Journal of the Optical Society of America B-Optical Physics*, vol. 23, pp. 318–325, 2006.

[70] Liu, X., Shreenath, A., Kimmel, M., Trebino, R., and Smith, A.V.and Link, S., "Numerical simulations of optical-parametric-amplification cross-correlation frequency-resolved optical gating," *Journal of the Optical Society of America B-Optical Physics*, vol. 23, no. 2, pp. 318–325, 2006.

[71] Liu, X., Trebino, R., and Smith, A., "Numerical simulations of ultrasimple ultrashort laser-pulse measurement," *Optics Express*, vol. 15, no. 8, pp. 4585–4596, 2007.

[72] Lucy, L. B., "An iteration technique for the rectification of observed distributions," *Astron. J.*, vol. 79, pp. 745–754, 1974.

[73] Miller, P., ed., *Ultrafast Phenomena XIII.* 2003.

[74] Moon, J., Mahon, R., Duncan, M., and Reintjes, J., "3-dimensional reflective image-reconstruction through a scattering medium based on time-gated raman amplification," *Optics Letters*, vol. 19, no. 16, pp. 1234–1236, 1994.

[75] Morton, K. and Mayers, D., *Numerical Solution of Partial Differential Equations, An Introduction.* Cambridge, UK: Cambridge University Press, 2005.

[76] O'Shea, P., Akturk, S., Kimmel, M., and Trebino, R., "Practical issues in ultra-short-pulse measurements with 'grenouille',," *Appl. Phys. B*, vol. 79, pp. 683–691, 2004.

[77] O'Shea, P., Kimmel, M., Gu, X., and Trebino, R., "Highly simplified device for ultrashort-pulse measurement," *Optics Letters*, vol. 26, no. 12, pp. 932–934, 2001. English Article OPTICS LETTERS.

[78] Peatross, J. and Rundquist, A., "Temporal decorrelation of short laser pulses," *Journal of the Optical Society of America B-Optical Physics*, vol. 15, pp. 216–222, 1998.

[79] Peri, D., "Optical implementation of a phase retrieval algorithm," *Applied Optics*, vol. 26, pp. 1782–1785, 1987.

[80] Piasecki, J., Colombeau, B., Vampouille, M., Froehly, C., and Arnaud, J. A., "Nouvelle methode de mesure de la reponse impulsionnelle des fibres optiques," *Applied Optics*, vol. 19, pp. 3749–3755, 1980.

[81] Press, W. H., Flannery, B. P., Teukolsky, S. A., and Vetterling, W. T., *Numerical Recipes in C.* Cambridge, UK: Cambridge University Press, 1988.

[82] Reid, D., Loza-Alvarez, P., Brown, C., Beddard, T., and Sibbett, W., "Amplitude and phase measurement of mid-infrared femtosecond pulses by using cross-correlation frequency-resolved optical gating," *Optics Letters*, vol. 25, no. 19, pp. 1478–1480, 2000.

[83] Richardson, W., "Bayesian-based iterative method of image restoration," *Journal of the Optical Society of America B-Optical Physics A-Optics, Image Science and Vision*, vol. 62, pp. 55–59, 1972.

[84] Riedle, E., Beutter, M., Lochbrunner, S., Piel, J., Schenkl, S., Sporlein, S., and Zinth, W., "Generation of 10 to 50 fs pulses tunable through all of the visible and the nir," *Applied Physics B-Lasers and Optics*, vol. 71, pp. 457–465, 2000.

[85] Rudolph, W. and Wilhelmi, B., *Light Pulse Compression.* Zurich: Harwood, 1989.

[86] Sala, K., Kenney-Wallace, G., and Hall, G., "Cw autocorrelation measurements of picosecond laser pulses," *IEEE Journal of Quantum Electronics*, vol. 16, pp. 990–996, 1980.

[87] Shen, Y. R., *The Principles of Nonlinear Optics*. New York: John Wiley & Sons, 1984.

[88] Smith, A., *SNLO Nonlinear Optics Code*. Sandia National Laboratories, Albuquerque, NM 87185-1423.

[89] Smith, A., "Group-velocity-matched three-wave mixing in birefringent crystals," *Optics Letters*, vol. 26, pp. 719–721, 2001.

[90] Stark, H., *Image Recovery: Theory and Application*. Orlando: Academic Press, 1987.

[91] Taft, G., Rundquist, A., Murnane, M. M., Christov, I. P., Kapteyn, H. C., DeLong, K. W., Fittinghoff, D. N., Krumbugel, M. A., Sweetser, J. N., and Trebino, R., "Measurement of 10-fs laser pulses," *IEEE Journal of Selected Topics in Quantum Electronics*, vol. 2, pp. 575–585, 1996.

[92] Trebino, R. and Kane, D. J., "Using phase retrieval to measure the intensity and phase of ultrashort pulses: frequency-resolved optical gating," *Journal of the Optical Society of America B-Optical Physics A-Optics, Image Science and Vision*, vol. 10, pp. 1101–1111, 1993.

[93] Trebino, R., *Frequency-Resolved Optical Gating*. Boston: Kluwer Academic Publishers, 2002.

[94] Uesugi, Y., Mizutani, Y., and Kitagawa, T., "Developments of widely tunable light sources for picosecond time-resolved resonance raman spectroscopy," *Review of Scientific Instruments*, vol. 68, no. 11, pp. 4001–4008, 1997.

[95] V., K. V., G., S. P., and A., S. V., "Regularized iterative algorithm for the phase retrieval," *Optik*, vol. 94, pp. 96–99, 1993.

[96] Wang, Z. Y., Zeek, E., Trebino, R., and Kvam, P., "Beyond error bars: Understanding uncertainty in ultrashort-pulse frequency-resolved-optical-gating measurements in the presence of ambiguity," *Optics Express*, vol. 11, no. 26, pp. 3518–3527, 2003.

[97] Wang, Z. Y., Zeek, E., Trebino, R., and Kvam, P., "Determining error bars in measurements of ultrashort laser pulses," *Journal of the Optical Society of America B-Optical Physics*, vol. 20, no. 11, pp. 2400–2405, 2003.

[98] Weiner, A. M., Heritage, J. P., and Thurston, R. N., "Synthesis of phase-coherent, picosecond optical square pulses," *Optics Letters*, vol. 11, no. 3, pp. 153–155, 1986.

[99] Wiener, N., *Extrapolation, Interpolation, and Smoothing of Stationary Time Series*. New York: Wiley, 1949.

[100] Wilson, K. R. and Yakovlev, V. V., "Ultrafast rainbow: tunable ultrashort pulses from a solid-state kilohertz system," *Journal of the Optical Society of America B-Optical Physics*, vol. 14, no. 2, pp. 444–448, 1997.

[101] Wilson, T. and Sheppard, C., *Theory and Practice of Scanning Optical Microscopy*. London: Pergamon 1984, 1984.

[102] Wyatt, R., , and Marinero, E. E., "Versatile single-shot background-free pulse duration measurement technique, for pulses of subnanosecond to picosecond duration," *Appl. Phys.*, vol. 25, pp. 297–301, 1981.

[103] Yang, Y., Galatsanos, N., and Stark, H., "A projection-based approach to the blind deconvolution problem," *Journal of the Optical Society of America B-Optical Physics A-Optics, Image Science and Vision*, vol. 11, no. 9, pp. 2401–2409, 1994.

[104] Yudilevich, E., Levi, A., Habetler, G. J., and Stark, H., "Restoration of signals from their signed fourier-transform magnitude by the method of generalized projections," *Journal of the Optical Society of America B-Optical Physics A-Optics, Image Science and Vision*, vol. 4, no. 1, pp. 236–246, 1987.

[105] Zhang, J. Y., Huang, J. Y., and Shen, Y. R., "Optical parametric generation and amplification," in *An International Handbook on Laser Science and Technology* (Lectokhov, V. S., Shank, C. V., S. Y. R., and Walther, H., eds.), Hardwood Academic Publishers, 1995.

[106] Zhang, J. Y., Lee, C. K., Huang, J. Y., and Pan, C. L., "Sub femtojoule sensitive single-shot opa-xfrog and its application in study of white-light supercontinuum generation," *Optics Express*, vol. 12, pp. 574–581, 2004.

[107] Zhang, J. Y., Shreenath, A., Kimmel, M., Zeek, E., Trebino, R., and Link, S., "Measurement of the intensity and phase of attojoule femtosecond light pulses using optical-parametric-amplification cross-correlation frequency-resolved optical gating," *Optics Express*, vol. 11, pp. 601–609, 2003.

VITA

Xuan Liu was born in Yinchuan, the capital of NingXia province, P. R. China. She recieved the degree of Bachelor of Science in Physics from the University of Science and Technology of China(USTC), Hefei, China, 1999. She received her Master of Philosophy in Chemistry from the University of Nottingham, Nottingham, UK, 2001. Since then, she came to the school of Physics, Georgia Institute of Technology, Atlanta, USA to pursue her PhD degree. She joined Dr. Rick Trebino's group in 2002.